Development of Muon Chamber in CBM experiment and Study of Particle Production in Low Energy Heavy-Ion Collisions

Ph.D. Thesis

By

SUMIT KUMAR KUNDU

DEPARTMENT OF PHYSICS

INDIAN INSTITUTE OF TECHNOLOGY INDORE

DECEMBER 2022

Development of Muon Chamber in CBM experiment and Study of Particle Production in Low Energy Heavy-Ion Collisions

A THESIS

Submitted in partial fulfillment of the
requirements for the award of the degree
of
DOCTOR OF PHILOSOPHY

by
SUMIT KUMAR KUNDU

DEPARTMENT OF PHYSICS
INDIAN INSTITUTE OF TECHNOLOGY INDORE
DECEMBER 2022

INDIAN INSTITUTE OF TECHNOLOGY INDORE

I hereby certify that the work which is being presented in the thesis entitled **Development of Muon Chamber in CBM experiment and Study of Particle Production in Low Energy Heavy-Ion Collisions** in the partial fulfillment of the requirements for the award of the degree of **DOCTOR OF PHILOSOPHY** and submitted in the **DEPARTMENT OF PHYSICS, Indian Institute of Technology Indore**, is an authentic record of my own work carried out during the time period from **July 2017** to **December 2022** under the supervision of **Dr. Ankhi Roy**, Associate Professor, Indian Institute of Technology Indore.

The matter presented in this thesis has not been submitted by me for the award of any other degree of this or any other institute.

Sumit 17/04/2023

Signature of the student with date
(SUMIT KUMAR KUNDU)

This is to certify that the above statement made by the candidate is correct to the best of my knowledge.

Ankhi Roy 17/04/2023

Signature of Thesis Supervisor with date
(Dr. ANKHI ROY)

Mr. SUMIT KUMAR KUNDU has successfully given his Ph.D. Oral Examination held on 17/04/2023

Ankhi Roy 17/04/2023

Signature of Thesis Supervisor with date
(Dr. ANKHI ROY)

Dedicated

to

my school friends

and family

ACKNOWLEDGEMENTS

It has been an incredible journey during this Ph.D. program. First, I would like to thank Dr. Maneesha Garg, my mentor during my M.Sc., who motivated and guided me to join Ph.D. during my M.Sc. I may not even join the Ph.D. program if she was not there to help.

I want to thank my thesis supervisor, Dr. Ankhi Roy, who was always there for me, thought more highly of my abilities than of myself and supported me in every possible way. Thanks a lot to Dr. Manavendra Mahato and Prof. Subhendu Rakshit, who are responsible for evaluating my progress every year; they kept me on track with their valuable suggestions and constructive criticism. I highly appreciate the support of all the faculties in the Department of Physics, Indian Institute of Technology Indore, including staff Prashant Gupta, Ved Prakash, Nitin Upadhyay, and Sunny Namdev, for providing such a pleasant environment for research. A time-to-time outing and discussion with Dr. Biplab Ghosh gave me a lot of confidence during my Ph.D.

A huge thanks to Dr. Partha Pratim Bhaduri for allowing me to work with him and providing the required guidance occasionally. I want to thank Dr. Subhasis Chattopadhyay, Dr. Anand Kumar Dubay, Dr. Jogender Saini, Dr. Zubayer Ahmed, Dr. Vikas Singhal, Ekata Nandy, Chandrasekhar Ghosh, Vinod Negi for their suggestions, and guidance during my visits to VECC, Kolkata. Thank you, Omveer Choudhary, Dr. Ajit Kumar, Vivek, Apar, and Dr. Mitali Mondal, for your company at VECC.

It was a wonderful experience while working at the Bose Institute, Kolkata. All credit goes to Dr. Sidharth Kumar Prasad for making it so easy to work there. A sincere thanks to Dr. Saikat Biswas, Dr. Supriya Das, Dr. Susnata Seth, Arindam Sen, and Sayak Chatterjee for their help during the Bose Institute visit.

This journey will be nothing without the support of friends at IIT Indore. My flatmates Rajarshi Roy, and Mrinal Kashyap, thank them for their beautiful memories

and delicious cooking. Thanks to Diksha Tiwari, Md. Fulbabu Sk., Satyam, Omkar Indari, Sandeep Choudhary, Suman Deb, Rutuparna Rath, Devesh Pathak, Caption Rituraj Singh, Sarvesh Mangla, Dhruv Ringe, Sajjan Rajput, Rahul Kumar Verma, Charu Di, Vikas Bhai, Nisha Di, Amarnath Sir, Palash Sir, Mahesh Patel, Geeta Di, Priya, and other J. C. Bose residents for making the stay at IIT Indore so enjoyable.

The support and love I get from my labmates are beyond words. Starting with the most supporting person Dr. Sudhir Rode, there are Dr. Ajay Kumar, Dr. Sudeep Ghosh, Dr. Ankita Goshwami, Ravindra Singh, Yoshini Bailung, Swapnesh Khade, Jaswant, Hriday, Prasoon, Ravi, Yatharth, Praveen, Tarun, Rashi, Niyathikrishna M R, who make the research life so comforting and provide support in every up and down of this journey.

There is no achievement without the support of our family members. The continuous effort and support of my father, Mr. Ved Singh Kundu, and my mother, Mrs. Pramila Devi, bring out the best in me. Thanks a lot to my dear brother Rakesh Kundu, sister-in-law Ritika Dalal for their support when I need it the most, and my niece Paavani Kundu for fulfilling our life with joy and happiness. I could never thank enough my wife, Chanchal Rana, and my beloved daughter Avni Kundu for being there with me constantly during this journey. They are the reason that I never had downtime during this time period.

Finally, I want to express my gratitude to everyone who helped with this thesis in whatever form.

(Sumit Kumar Kundu)

SYNOPSIS

Our fundamental quest about the creation and evolution of the present universe ignites the research in relativistic heavy ion collisions. It is believed that a hot de-confined state of quarks and gluons, known as Quark-Gluon Plasma (QGP), was created at the beginning of the universe. Experiments at the Relativistic Heavy Ion Collider (RHIC) at Brookhaven National Laboratory (BNL), USA, and the Large Hadron Collider (LHC) at CERN are unique facilities to create such exotic states in the laboratory by relativistic heavy ion collisions. They already revealed a lot about the hot Quantum Chromodynamic (QCD) state. According to Lattice QCD prediction [1], a baryon-rich cold QGP state that may exist in neutron stars can also be produced in the laboratory at high baryon density and moderate temperature. However, experimentally the baryon-rich QGP state is not much explored compared to the hot one. The experiments at the Nuclotron-based Ion Collider fAcility (NICA) at Dubna, Russia, and the Compressed Baryonic Matter (CBM) experiment at the Facility for Antiproton and Ion Research (FAIR) accelerator at GSI, Darmstadt, are the upcoming efforts that aim to explore the high baryon density and moderate temperature region of the QCD phase diagram.

Motivation

FAIR will provide different nuclear beams in the energy range of 2A to 35A GeV to strike a fixed target in the CBM experiment. Due to the expected high heavy-ion beam intensities ($\approx 10^9/sec$), the CBM experiment will have the opportunity of getting a high interaction rate (10 MHz), which enables the detection of low-mass vector mesons (ρ, ω, ϕ) and rare probes like charmonium (J/ψ) via their di-leptonic decay channel. This will enable CBM to address some fundamental questions of Quantum Chromodynamics, like the phase transition from a confined hadronic to a partonic de-confined state, the chiral symmetry restoration, and in-medium mass modification of different vector mesons.

In CBM experimental setup, the Micro Vertex Detector (MVD) for precise vertexing and the Silicon Tracking System (STS) detector for the track reconstruction for a wide range of momentum (100 MeV/c to 10 GeV/c) are placed near the target inside the dipole magnet. Ring Imaging Cherenkov (RICH) detector to detect electrons or Muon Chamber (MuCh) system to detect muons will be placed just outside the dipole magnet. It is a unique feature of CBM experiment, which enables us to compare the physics results from both the leptonic (electron or muon) channels from the same setup by only exchanging RICH or MuCh detector. Transition Radiation Detector (TRD) is placed after RICH detector to detect electrons of momentum greater than 1.5 GeV/c. The next detector in the line is the time-of-flight (TOF) detector which will detect the charged hadrons. Finally, a Projectile Spectator Detector (PSD) is placed to detect the centrality of the collision and orientation of the reaction plane.

This thesis includes our contribution to the development of a cooling system for the Muon Chamber (MuCh) detector and simulation study of the CBM [2] experiment at FAIR, situated at GSI, Darmstadt, Germany. In addition, we see the effect of different nuclear equations of state and beam energy on anisotropic flow and particle production in simulated low-energy heavy-ion collisions. This study covers the energy range from the existing GSI-SIS energy of the High Acceptance Di-Electron Spectrometer (HADES) experiment to top Super Proton Synchrotron (SPS) energy. The effect of various particlization scenarios of the Ultra-relativistic Quantum Molecular Dynamics (UrQMD) model on variables like anisotropic flow, proton rapidity spectra, and particle production has also been analyzed to predict the available experimental results more accurately. The results and conclusions from these studies will be useful for a better understanding of the underlying physics of the model and to compare the outcome with the results from future experiments at FAIR and NICA.

CBM MuCh Cooling System

A muon detection system MuCh is under construction in India, mainly at VECC, Kolkata, with the collaboration of other Indian institutes. The MuCh detector [3] consists of triplets of tracking detectors placed between the hadron absorber layers. The final design of MuCh detector consists of six hadron absorbers of different thicknesses and eighteen gaseous detector layers in the set of triplets, making six tracking stations. There is a requirement for a cooling system that could extract the heat from the confined area of the MuCh detector, generated due to Front End electronic Boards (FEBs) placed at the detector plates. We investigate a solution to the above requirement by developing a cooling system using de-mineralized water as a coolant [4]. To check the concept of the cooling system, two plates of real-size prototypes are tested in a test beam experiment at the CERN SPS beam line facility. Two different arrangements of the water distribution have been studied using three sample prototypes to check the suitable configuration of the cooling system for a single detector layer. Based on this study, a realistic model for water distribution has been proposed for the first layer of the MuCh detector station.

Estimation of MuCh Data Rate Handling Capacity

We have contributed to simulation studies as well to increase the performance and for better tuning of the detectors. Different changes have been studied in the simulated geometry of the CBM detector using the GEANT3 transport engine to check the effect of newly added devices and material layers. It is helpful for reducing the R&D cost and saving time. In one such simulation study, the MuCh detector data rate has been estimated using a coherent source which is mainly from ion-ion collision events, using GEANT3 and GEANT4 transport engines. A comparison has been made for point density per event for each detector station. More contribution of secondary particles has been observed using the GEANT4 transport engine. The occupancy, i.e., the fraction of fired pads per event for each detector station, has been studied, and the maximum pad hit rate has been estimated for each station of the MuCh detector. It helps to estimate the minimum requirement of data rate handling capacity of a detector that will be used in the CBM experimental setup.

Hadron Identification using PID framework

The CBM experiment offers flexibility in the detection of both leptons as well as hadrons. While tracking the reconstruction of hadrons, it is hard to distinguish pions, kaons, and protons beyond some particular transverse momentum range. A Particle Identification Framework (PID) has been used for detecting hadrons more efficiently beyond that transverse momentum range. This PID framework uses graphical cuts on charge×momentum ($\mathrm{q} \times \mathrm{p}$) versus invariant mass (m^2) distribution to identify particles initially. Then the invariant mass distribution of identified particles is fitted with Gaussian for signal and second order polynomial for background in different momentum ranges. The stabilized fitting parameters for individual particles in different momentum ranges are used to calculate the Bayesian probability (purity) by using the formula:

$$Purity_i = \frac{P_i}{\Sigma P_i + P_{bg}} \tag{0.1}$$

P_i and P_{bg} represent the probability of a track being a hadron or a background particle respectively. This purity is used to identify proton, pion and kaon. It has been observed that, by using this framework, we are able to increase the efficiency and decrease false particle detection to a large extent.

Phenomenological Study on Anisotropic Flow

The main aim of CBM experiment at FAIR is to explore the baryon-rich region of the QCD phase diagram. Before the availability of data from CBM experiment, it is necessary to do model-based studies of different observables sensitive to the production of QCD medium in the same energy region and validate it with available experimental results. The anisotropic flow of particles is one such observable that could be studied as it is directly affected due to pressure gradient from multiple scatterings between constituents of the medium, which depends directly on the underlying nuclear equation of state.

Dependence on Nuclear Equations of State

We investigate the dependence of anisotropic flow coefficients and particle production on nuclear equations-of-state (EoS) in non-central (10–40% centrality) Au–Au collisions for a wide range of beam energy from 1A GeV to 158A GeV [5]. A publicly available version (v3.4) of the UrQMD [6] model is employed for this study. UrQMD provides three different configurations of a hybrid model for an intermediate hydrodynamical stage which are hadron gas (HG), chiral, and bag model EoS along with a pure transport approach. In the hybrid mode, the transport approach to explain the non-equilibrium dynamics is joined with a hydrodynamical description to describe the expansion of locally thermalized fireball. To extract QCD medium properties, such kind of combined approach could be very helpful. We qualitatively aim to understand the effect of various nuclear equations of state on the flow harmonics and hence gain some insights about dynamics leading to their development at various beam energies ranging from 1A to 158A GeV. Apart from anisotropic flow, we check the effect of EoS on particle production in noncentral collisions. To do so, particle ratios are examined for different species. Net-proton rapidity distributions have been examined, as it is expected to be sensitive to the underlying EoS of the nuclear fireball. Although, some studies have been done in this region for central collision. We extend this study to the noncentral collision events.

Initially, directed flow (v_1) is estimated for charged hadrons for pure transport and hybrid versions of UrQMD model. Elliptic flow (v_2) for pions and protons for transverse momentum $(\mathrm{p}_\mathrm{T}) < 2\ \mathrm{GeV/c}$ at 40A and 158A GeV as a function of rapidity are measured and compared with the available experimental results. For protons pure transport approach works better in explaining the NA49 data. While looking at the slope of the directed flow of pion and net protons, for pions, the slope remains negative for cascade mode during all investigated energies and shows a change from negative to positive for hydrodynamics modes between 30A to 80A GeV. In the case of net protons, a slight hint of sensitivity is seen for chiral and hadron gas EoS beyond 25A GeV. A strong increase in slope for the bag model could be due to inbuilt first-order phase transition and hence a possible hint towards the onset of deconfinement. A more detailed investigation is done on net protons by looking at their p_T-integrated directed flow and elliptic flow at midrapidity ($-0.5 < \mathrm{y}_{\mathrm{c.m.}} < 0.5$). The same kind of splitting is observed for bag model while observing directed flow. In the case of v_2, a similar splitting could be seen between the bag model and the other two EoS. To observe the effect of EoS on particle production, various particle ratios, namely, strange to non-strange and antiparticle to particle, are compared with the available data. In the case of K^-/π^- and K^+/π^+ ratio, chiral and hadron gas EoS can reproduce the trend set by data in both cases, but the magnitude is overestimated. For bag model EoS, K^-/π^- ratio gets saturated after 20A GeV, which creates splitting for bag model and other two EoS. For $\mathrm{K}^+/\mathrm{K}^-$ and π^+/π^- ratios, data seems to favor hybrid mode, with slight underestimation by hybrid in the case of $\mathrm{K}^+/\mathrm{K}^-$ ratio. In this study, it is observed that none of the available EoS can reproduce the experimental measurements quantitatively.

Dependence on Particlization Scenarios

In a further study [7], various particlization scenarios available in the hybrid UrQMD model are involved with the available EoS. Here, particlization represents the switching from fluid dynamic description to the transport description using various hypersurface criteria. We study which particlization scenario among gradual freeze-out (GF, default), isochronous freeze-out (ICF), and iso-energy density freeze-out (IEF) hypersurface is better in predicting the available experimental results. There is no such kind of physical particlization that takes place in the actual evolution of QCD matter. Hence, it is essential to optimize it to describe experimental results. This study aims to find the best possible combination of the particlization model and EoS, which can explain the experimental data. In different particlization scenarios, the choice of hypersurface and switching criteria allows the fluid dynamic evolution to cease at different times. So it must affect the flow of the species as it will spend more or less time in evolution. Initially, we look at the directed flow of pions and protons as a function of rapidity for various particlization scenarios and equation of states and found out that directed flow is quite sensitive to particlization scenarios. The slope of directed flow at mid-rapidity is an interesting observable and contains insights into medium properties. From the slope of the directed flow of protons with $\mathrm{p_T} < 2\ \mathrm{GeV/c}$, it is observed that the IEF scenario shows better agreement with the experimental results for all three EoS at beam energies greater than $20 - 25\mathrm{A}\ \mathrm{GeV}$. The same kind of agreement was observed when we studied the elliptic flow for net protons. Particle ratios should also be sensitive to the underlying particlization modes as this fluid-to-particle transition can alter the chemical composition of the system. Starting with strange to non-strange ratio such as K^-/π^- and K^+/π^+, we look at particle to anti-particle ratio of $\mathrm{K}^-/\mathrm{K}^+$, π^-/π^+, and $\bar{\mathrm{p}}/\mathrm{p}$ as well as baryon to meson ratio of p/π^+ and $\bar{\mathrm{p}}/\pi^-$ as a function of beam energy and are compared with the available experimental results. In all the cases, the ratios have shown excellent agreement with the experimental measurements in the IEF scenario for all three cases of EoS. These ratios seem more sensitive to the particlization scenarios than the equation of state because of the possible change in the particle chemistry. From all these investigations, it seems clear that IEF scenario brings more clarity in understanding and interpreting the experimental results.

Conclusions and outlook

In this thesis, an attempt has been made to study the detector and the physics performance of the CBM MuCh setup, along with a feasibility study of particle production in heavy-ion collisions at low beam energies using the UrQMD model. In the former case, detailed research has been done for the concept, design, fabrication, and test performance of a water-based cooling system of CBM MuCh detector. A prototype for the cooling system of the CBM MuCh detector system has been developed for the first two stations at Bose Institute, Kolkata. Two different configurations using three prototypes have been studied. The same principle and technique could be used for any other system by customizing various parameters like shape, size, material type, and thickness of the cooling plate. This type of cooling system could be used for any system where large heat is generated in a very confined space. In a simulation study, the pad hit rate has been estimated for each station of the CBM MuCh detector using GEANT3 and GEANT4 transport engines. It predicts how much data rate each station has to handle while in operation. Besides that, a PID framework has been used to identify the hadrons with greater efficiency than the traditional cut-based method.

In the latter part of the thesis, we performed a feasibility study of particle production in heavy-ion collisions. As the CBM experiment will take some time to gather actual data, there is not so much exploration in the CBM experiment energy range. We do a simulation study using the UrQMD event generator in this energy region and look at the possible modes of that model to predict the experimental results. Such a study has been done to check the effect of the equation of state and energy dependence and to check the impact of various particlization scenarios by looking at the anisotropic flow, particle production, and other variables for low-energy heavy ion collisions. Initially, none of the EoS was able to predict the experimental results thoroughly. Although different variables show sensitivity to different EoS in a hybrid model. By looking at different particlization scenarios for all EoS, we are able to predict that the choice of IEF particlization scenario is more beneficial and provides good agreement with the experimental results.

Publications from the thesis:

Journal Publications:

1. **“Dependence on beam energy and nuclear equation of state of anisotropic flow and particle production in low-energy heavy-ion collisions”, S. K. Kundu**, Y. Bailung, S. P. Rode, P. P. Bhaduri, and A. Roy, Phy. Rev. C **104**, 024907 (2021), https://doi.org/10.1103/PhysRevC.104.024907
2. **“Effect of various particlization models on anisotropic flow and particle production using UrQMD hybrid model”, S. K. Kundu**, Y. Bailung, S. P. Rode, P. P. Bhaduri, and A. Roy, Nucl. Phys. A **1030**, 122574 (2023), https://doi.org/10.1016/j.nuclphysa.2022.122574
3. **“Development of a water-based cooling system for the Muon Chamber detector system of the CBM experiment”, S. K. Kundu**, S. Biswas, S. Chattopadhyay, S. Das, A. K. Dubey, C. Ghosh, A. Kumar, A. Roy, J. Saini, S. Seth, and S. K. Prasad, Nuclear Inst. and Methods in Physics Research, A **1050**, 168143 (2023), https://doi.org/10.1016/j.nima.2023.168143

Conference Proceedings:

1. **“Dependence of anisotropic flow of net-protons on particlization model for various nuclear equation of state”, S. K. Kundu**, Y. Bailung, S. P. Rode, P. P. Bhaduri, and A. Roy, Proceeding of DAE-BRNS Symp. Nucl. Phys. **321**, 650-651 (2021), https://inspirehep.net/literature/2028498
2. **“Feasibility study of water distribution for the CBM MuCh cooling system”, S. K. Kundu**, S. Seth, S. Biswas, S. K. Ghosh, S. Das, and S. K. Prasad, Proceeding of DAE-BRNS Symp. Nucl. Phys. **323**, 790-791 (2021), https://inspirehep.net/literature/2028285

3. **“Dependence of anisotropic flow and particle production on particlization models and nuclear equation of state”, S. K. Kundu**, Y. Bailung, S. P. Rode, P. P. Bhaduri, and A. Roy, Proceeding of Hot QCD Matter 2022, https://doi.org/10.1142/S0218301322500975

Progress Reports:

1. **“Estimation of MuCh data rate: event coherent background from GEANT3 and GEANT4”, S. K. Kundu**, P. P. Bhaduri, S. Chattopadhyay, and A. Roy, CBM Progress Report 2018, **165**, https://repository.gsi.de/record/220128
2. **“Performance study of the first two stations of CBM MuCh cooling system”, S. K. Kundu**, S. Seth, S. K. Prasad, S. Das, S. Kumar, S. R. Ghosh, and A. Roy, CBM Progress Report 2019, **102**, https://repository.gsi.de/record/228172
3. **“Identification of Hadrons using PID framework”, S. K. Kundu**, A. Sen, S. Biswas, A. Roy, and S. Das, CBM Progress Report 2021, **198**, https://repository.gsi.de/record/246663

Publications beside the thesis:

1. **“Study of jet fragmentation via azimuthal angular correlations of heavy flavor decay electrons in pp, p–Pb, and Pb–Pb collisions using PYTHIA8+Angantyr”,**
   R. Singh, Y. Bailung, **S. K. Kundu**, and A. Roy, Phy. Rev. C **107** 024911 (2023), https://doi.org/10.1103/PhysRevC.107.024911

Contents

Figures

Tables

Chapter 1

Introduction

In this chapter, some details about the standard model, QCD phase diagram, and Quark-Gluon Plasma have been discussed. The motivation for this thesis is mentioned in the overall structure of the thesis.

1.1 Standard Model

In this universe, every object around us, known as ”Matter,” is made up of a few fundamental particles. The standard model of particle physics very well explains these fundamental particles and their interactions. The standard model is a quantum field theory that describes three out of the four known fundamental forces of our Universe, which are the strong force, electromagnetic force, and weak nuclear force. This theory is developed after many discoveries in experimental and theoretical studies. According to the Standard Model, elementary particles shown in Figure 1.1 can be classified into quarks, leptons, and bosons. There are six flavors of quarks: up (u), down (d), strange (s), charm (c), top (t), and bottom (b), and six leptons: electron (e), electron neutrino (ν_e), muon (μ), muon neutrino (ν_μ), tau (τ), and tau neutrino (ν_τ). Each quark and lepton have its own corresponding anti-particle. These quarks and leptons are further categorized into three generations depending on their mass and decay time. All stable matter in the world is made up of first-generation particles. Another category of elementary particles in the Standard Model are bosons, which are classified as gauge and scalar bosons. Gauge bosons ($g,\ \gamma,\ Z,\ W^{\pm}$) act as force carriers for three fundamental forces other than the gravitational force. Gluons act as force carriers of the strong force, $W^{\pm}$, and Z bosons are responsible for weak interaction, whereas photons are force carriers for the electromagnetic force. Recently, one scalar boson called Higgs boson was

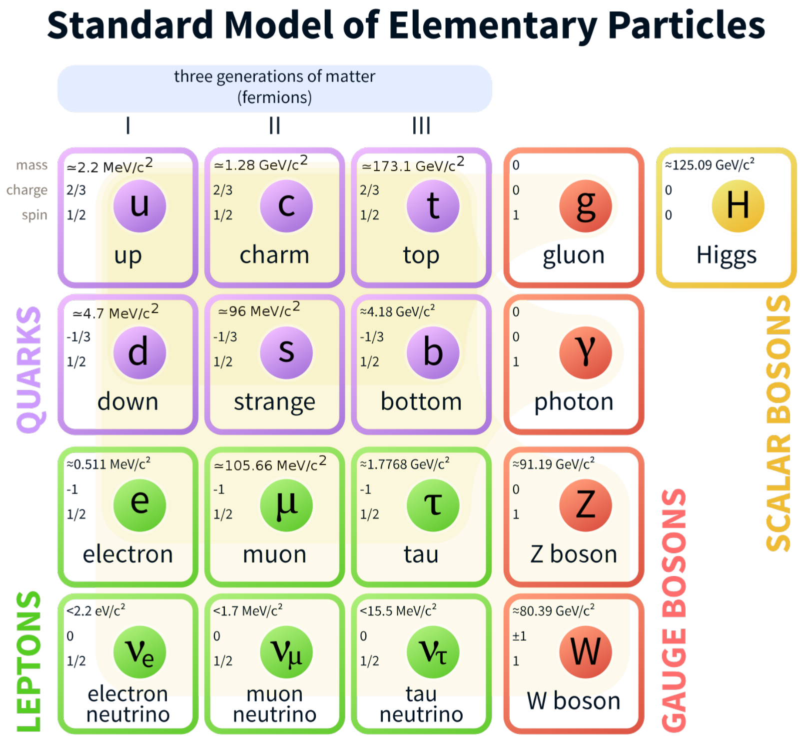

Figure 1.1: The classification of elementary particles included in the Standard Model. Ref. [8]

discovered by CERN [9, 10], which is responsible for giving masses to the quarks and leptons because of interaction with them. At the very early stage of the evolution of the universe, the strong force dominates among quarks and gluons.

1.2 Quantum Chromodynamics (QCD)

The QCD is the theory [11] that explains the strong interaction of the standard model among quarks and gluons. The formulation of QCD calls for local gauge invariance under SU(3) gauge transformations in the quark color space [12, 13]. In QCD, color charge serves as the equivalent of electric charge in Quantum Electrodynamics (QED). According to QCD, all combinations of quarks in hadrons, either baryon (made up of three quarks) or meson (made up of a quark and an anti-quark), will contain a mixture of three color charges to produce colorless hadrons. In any hadron, strong force binds the quarks by the exchange of gluons. In QCD, the potential among two quarks separated by a distance 'r' is approximated by using the formula:

$$V_s(r) = -\frac{4}{3}\frac{\alpha_s}{r} + kr \tag{1.1}$$

where α_s represents the strong coupling constant, and k is the QCD string constant of magnitude $\sim$ 1 GeV/fm. For r greater than 1 fm, the second linear term dominates in equation 1.1, for r tends to infinity, potential becomes infinite. If a huge amount of energy is provided to separate two quarks from each other, that energy will be sufficient to produce a $q\bar{q}$ pair from the QCD vacuum, which combines with the initial quarks to produce either baryon or meson. That is why an isolated quark can never be found in nature. This phenomenon is known as *quark confinement*. For r smaller than 1 fm, the first term in equation 1.1 dominates. In that case, deconfinement may occur if α_s tends to zero faster compared to r. α_s strongly depends on the square of the momentum transfer (Q^2) between two interacting quarks at small distance. This dependence of

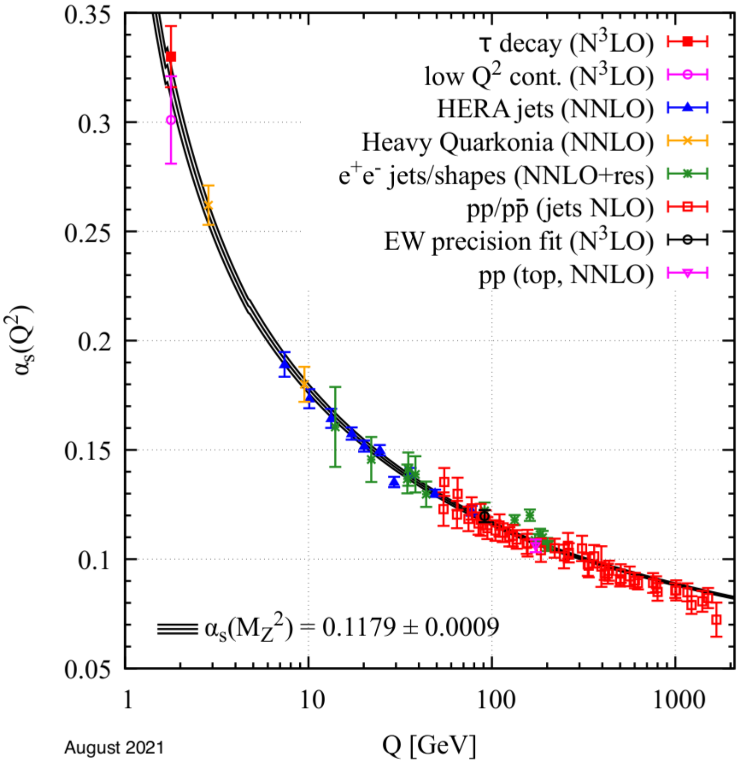

Figure 1.2: The strong coupling constant α_s as a function of Q measured from different experimental and theoretical calculations. Ref. [14]

α_s on Q^2 [15] is represented by the equation 1.2 as follows:

$$\alpha_s(Q^2) = \frac{12\pi}{(33 - 2n_f) \cdot ln(Q^2/\Lambda^2_{QCD})} \tag{1.2}$$

where Λ_{QCD} represents QCD scale parameter and n_f represents the number of quark flavors. Figure 1.2 shows how α_s depends on Q. α_s tends to zero for asymptotically large Q, and hence quarks become free within a certain range of r; this is known as *asymptotic freedom* [16, 17].

1.3 QCD Phase Diagram

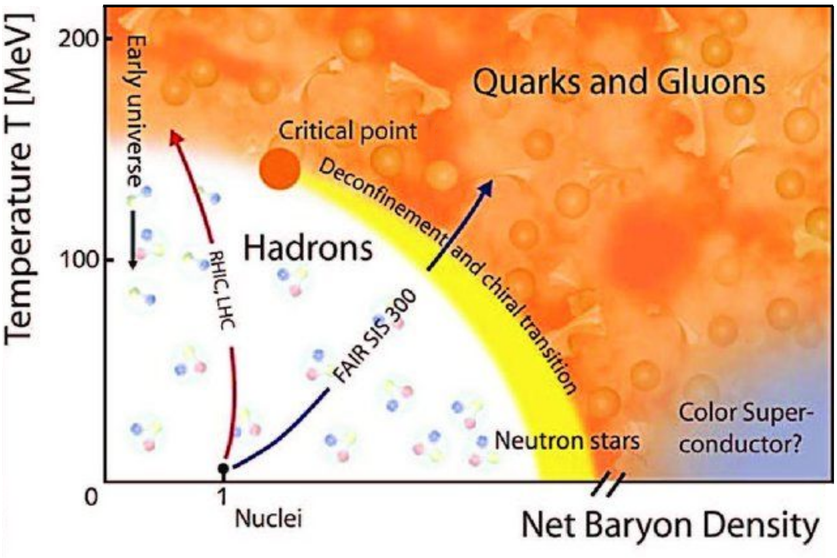

Figure 1.3: Schematic view of QCD phase diagram. Ref. [18]

The QCD predicts the behavior of the particles at different temperatures and net-baryon densities by using the QCD phase diagram. Different models like lattice QCD or effective field theories predict QCD phase diagram. The QCD phase diagram, as shown in figure 1.3, represents the three different possible states of matter for different temperatures and net-baryon density regions: the hadronic state at low temperature and baryon density region, the QGP state at high temperature, and the color superconductor at low temperature and high baryon density region.

When the number of particles and antiparticles is almost equal for very low net baryon densities, QCD predicts that hadrons will break down into quarks and gluons above a temperature of about 160 MeV [19, 20]. During the first few microseconds following the big bang, the opposite process occurred in the universe: quarks and gluons were constrained into hadrons. It is anticipated that the transition from partonic to the hadronic matter will occur smoothly in this area of the phase diagram [1]. At relatively high levels of the baryon density, calculations indicate a critical endpoint [21]. Beyond this critical endpoint, one anticipates a first-order phase transition from hadronic to partonic matter with a phase coexistence area in between for higher values of net baryon densities (and for lower temperatures). Another form of transition could happen if the baryonic matter is compressed at a low temperature. This would occur if colored bosonic diquark pairs, the analog to Cooper pairs in QCD, formed as a result of an attractive interaction among quarks in the deconfined baryon-rich phase. These diquarks can then accumulate to form a color superconductor at a quite low temperature. Currently, it appears to be impossible to obtain a great degree of compression without heating needed for the production of color superconductor in a laboratory setting. A few seconds after the neutron star is born in the supernova explosion, it is anticipated that such high-density, highly interacting cold matter will exist in the neutron star's core. The diquark couples will be broken up by heating, converting the color superconductor into a regular color conductor. Modern heavy ion experiments at intermediate energies like CBM at FAIR and NICA at JINR are primarily focused on gaining additional insight into the extremely intriguing area of high net baryon densities.

1.4 Relativistic Heavy Ion Collisions and Quark-Gluon Plasma

To study the behavior of strongly interacting nuclear matter for various temperature and baryon density ranges, it is required to create hot and dense nuclear matter in the laboratory, which could be done either by increasing temperature or by compressing the nuclear matter. This can be done by colliding two heavy nuclei with each other at a speed comparable to the speed of light so that a large amount of kinetic energy will convert into thermal energy and hence creating a high-temperature or a dense baryonic region. When two ions collide at relativistic high energy, the dense hadronic matter is expected to be produced. The energy density goes above 1 GeV/fm^3 in a such collision, and the corresponding relativistic matter pressure attained in a such collision is approximately 0.52 $\times$ 10^{35} $Pascal$ [22]. According to available experimental results, these collisions result in the creation of a dense hadronic fireball with a well-localized space with an energy density of ϵ = 1 GeV/fm^3. Due to the quite high internal pressure of the fireball and lifetime depending on the size of the system, $\tau \simeq 2R/c$, where R is the radius of the system and c is the speed of light, it explodes rapidly, creating a large number of new hadrons which share the collision energy, and hence expected to create a high baryon density region for certain beam energy. The overall formation of different stages during the relativistic collision of two nuclei could be understood from the time evolution diagram in the next section.

1.4.1 Space-Time evolution

Figure 1.4 shows the space-time evolution plot of the high-energy heavy-ion collision. It can be studied in terms of the Bjorken model [23]. Here, two Lorentz contracted nuclei traveling at relativistic speed are colliding with each other. Based on the collision energy, two possibilities are conceivable following the initial collision phase. The left-hand side corresponds to the case where the energy density is not high enough for the formation of QGP, hence a purely hadronic scenario is formed, whereas the right-hand side displays the anticipated collision evolution above the threshold energy density for the generation of QGP [23, 24]. The following stages represent the time evolution of the fireball in a scenario involving QGP formation: At $t = 0$, two highly energetic length contracted nuclei strike with each other with impact parameter b at the origin $(z = 0)$. Most part of their kinetic energy is dumped into a small volume in the central part of the collision area. Due to this energy, in the pre-equilibrium stage, a large number of quark-antiquark pairs and gluons are produced just after the collision. These produced partons interact with each other for 0.5–1 fm/c to reach an equilibrium state called QGP. The QGP expands and cools due to pressure gradient for 3–5 fm/c. These partons hadronize when energy density falls below the critical value (ϵ_c = 1 GeV/fm^3). Further expansion occurs until chemical freeze-out, where inelastic interaction stops, and then

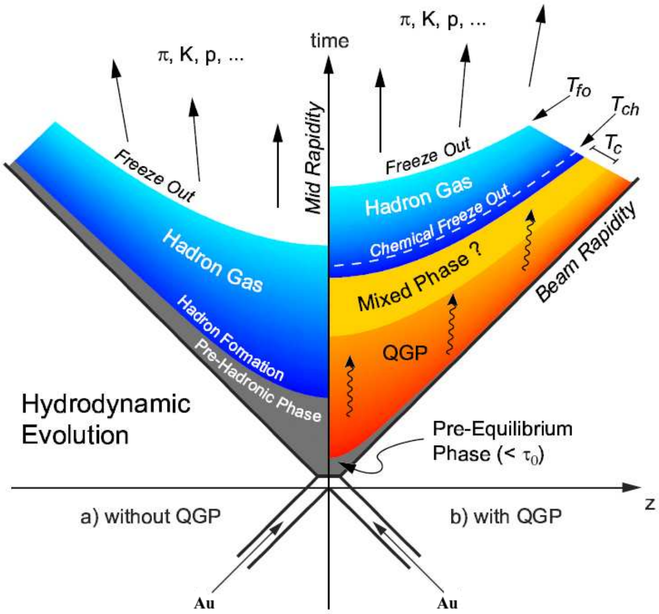

Figure 1.4: Plot to show the evolution of a fireball produced in relativistic heavy ion collisions in the light cone picture. Ref. [25]

up to kinetic freeze-out, where momentum transfer stops between the hadrons. Particles at this stage reach the detector. It takes around 10–15 fm/c time from the initial collision to reach this point, depending on the beam energy.

1.4.2 Relativistic heavy-ion experiments in different energy regions

If we talk about the experiments that are trying to explore the QCD phase diagram in the different energy ranges, the experiments at facilities like Relativistic Heavy-Ion Collider (RHIC), at Brookhaven National Laboratory (BNL), and Large Hadron Collider (LHC) has been extensively studied the region of high temperature and approx zero net baryon density region of the QCD phase diagram. Such dense nuclear matter is believed to exist in the early universe within a few microseconds after the big bang. The experiments provide conclusive results related to the formation of QGP. Although not so many studies have been done in the high baryon density region compared to the low net baryon density region, some facilities like the STAR collaboration at RHIC [26] and NA49 detector at the CERN-SPS [27] are trying to search the QCD critical endpoint in the high baryon density and intermediate temperature region.

The upcoming experiments like the Nuclotron-based Ion Collider fAcility (NICA) [28] at the Joint Institute for Nuclear Research (Dubna) and the Compressed Baryonic Matter (CBM) experiment [29, 30] at the Facility for Antiproton and Ion Research (FAIR, Germany) and ongoing Beam Energy Scan (BES) program at RHIC [31] aim to probe the high baryon density and moderate temperature region of the QCD phase diagram. These experiments will provide insights into the highly compressed baryonic matter which exist in the core of neutron stars.

1.4.3 Signatures of QGP

In high-energy heavy-ion collision experiments, QGP exist for a very short time period ($\sim 10^{23}\ s$), which is why it is not possible to detect QGP formation directly. We have to detect those particles which are produced in a fireball so that we can get indirect information about the formation of QGP. Different signatures like strangeness enhancement, photons and dileptons, jet quenching, quarkonium suppression, heavy-flavor production, and collective flow could help us in this regard. A few of them which are relevant to our study are discussed as follows:

Photons and dileptons

Nearly all stages of relativistic heavy-ion collisions are predicted to produce photons (real or virtual), which thereafter decay into dileptons (i.e., $e^+e^-, \mu^+\mu^-$). These electromagnetic radiations are the ideal probe to study the produced strongly interacting medium because they don't interact strongly any interact only electromagnetically. Even at the fireball stage, the mean free path of these probes ($\sim$ $10^2 - 10^4$ fm) is quite large compared to the system size ($\sim$ 10 fm). Hence they come out of the fireball and reach the detectors without losing any information about the interior of the fireball. Photons are categorized depending on their production stage. Such as prompt photons are produced during the very initial stage of the collision via initial hard scattering in processes like quark-gluon Compton scattering ($q + g \to q + \gamma$), quark anti-quark annihilation ($q + \bar{q} \to g + \gamma$), etc. Photons that are produced before the thermalization stage are known as pre-equilibrium photons. Thermal photons are produced from the QGP stage and via hadronic interaction in the hadronic phase.

Dileptons are way much heavier than photons and hence could be a more reliable source to gather knowledge about QGP compared to photons. The dileptons could be categorized into three following groups depending on their pair invariant mass:

- **Low mass region ($M \leq M_\phi$):** Dileptons produced from the decay of low mass vector mesons like η, ϕ, and ω, whose mass is less than mass of ϕ meson i.e. M_ϕ, lies in the low mass region.
- **Intermediate mass region ($M_\phi < M < M_{J/\psi}$):** This region covers the dileptons produced due to the thermal radiation of the fireball. Hence, it is very crucial to study about the QGP.
- **High mass region ($M \geq M_{J/\psi}$):** The dileptons produced from the decay of heavy quarkonia like J/ψ and Υ, and from the radiation coming from the primordial stage lies in this region.

Other than the temperature of the fireball, photons and dileptons help us to investigate the formation time of QGP [32]. Photons can help in studying the system size evolution using intensity interferometry [33–35]. Detection of dileptons could help to study the medium modifications of the vector mesons [36, 37] and to characterize the QGP phase using dilepton interferometry [38].

Quarkonium Suppression

Heavy quarks (Q) and anti-quarks ($\bar{Q}$) produce Quarkonium which is a stable bound state. Q can be either charm or bottom quark. $c\bar{c}$, $b\bar{b}$ are known as charmonium and bottomonium respectively. The masses of quarkonia are largely derived from the bare masses of their quark content, which are determined via the Higgs mechanism from the electroweak sector of the standard model, as opposed to the masses of light hadrons, whose masses come from the interactions between their nearly massless constituents. In addition, a unique characteristic of these quarkonia is their modest size, which ranges from 0.1 to 0.3 fm, as opposed to light hadrons, which have a radius of around 1 fm. This shows that they have higher binding energy than light hadrons. The production of $D\bar{D}$/$B\bar{B}$ pairs from $c\bar{c}$ and $b\bar{b}$ is not permitted since their masses are less than two times those of the corresponding open heavy-flavor hadrons, i.e., $M_{c\bar{c}} < 2M_D$ $(D = c\bar{u})$ and

$M_{b\bar{b}} < 2M_B$ $(B = b\bar{u})$. J/ψ and Υ productions are responsive to the characteristics of the generated medium, claim by Matsui and Satz [39]. Quarkonia states would melt through color screening in the partonic medium at a specific temperature $T > T_c$, where T_c is the critical deconfinement temperature. They would be suppressed in heavy-ion collisions, which would point to the QGP's creation. J/ψ suppression was initially discovered experimentally at the SPS [40], and then further confirmed by the experiments like PHENIX, STAR and ALICE [26, 41–43].

Anisotropic flow

The anisotropic flow of the particles emitted in noncentral relativistic heavy-ion collisions is considered a promising observable to investigate the collective effects of the produced medium. In proton-proton collisions, particles are created isotropically in the transverse plane. But in noncentral heavy-ion collisions, the interaction volume is anisotropic, which causes multiple scattering of the colliding particles and changes the azimuthal distribution of their transverse momentum. Because of the numerous rescattering that occurred early on, as shown in the figure 1.5, the initial spatial anisotropy turns into momentum anisotropy. Additionally, the medium will enter into thermal equilibrium due to these rescatterings, which will expand collectively further. This collectivity might be reflected in the particle distributions that is created. The azimuthal distribution of the final state particles could be represented by the Fourier expansion [45] as follows:

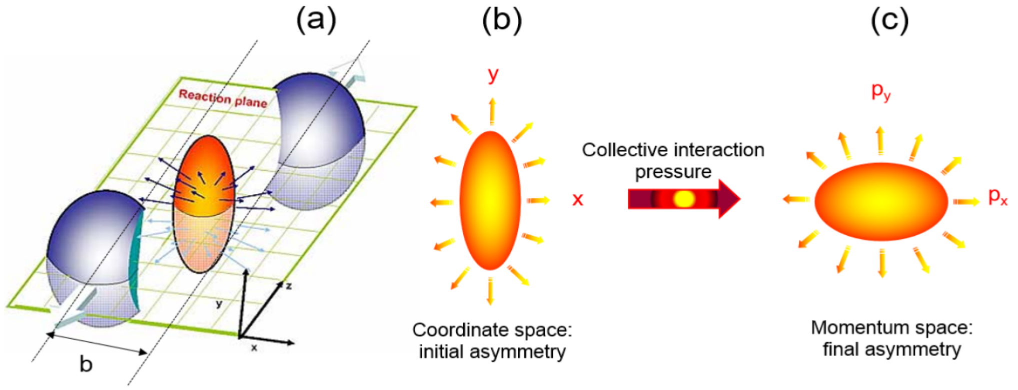

Figure 1.5: Anisotropical behavior in noncentral heavy-ion collision [44].

$$E\frac{d^3N}{d^3p} = \frac{1}{2\pi}\frac{d^2N}{p_T dp_T dy}\left[1 + \sum 2v_n cos(n(\phi - \psi_r))\right] \tag{1.3}$$

where the azimuthal angle of the particle and reaction plane angle are indicated by ϕ and ψ_r, respectively. v_n is the n_{th} Fourier coefficient of the azimuthal distribution, and it could be obtained from:

$$v_n = \left\langle \cos[n(\phi - \psi_r)] \right\rangle \tag{1.4}$$

where v_n is defined as directed flow (v_1), elliptic flow (v_2), triangular flow (v_3), quadrangular flow (v_4) for n = 1, 2, 3, 4 and so on, respectively. Figure 1.6 gives more clarification about the azimuthal angle of the particle, the reaction plane angle, and the directed and elliptic flow in the momentum space. These coefficients are believed to provide insight into the dynamics of the fireball. For instance, the significant magnitude of the v_2 has shed light on the possibility that the bulk of the produced matter achieves close to local thermal equilibrium conditions. The pressure gradient developed due to rescatterings in the early stage of the collisions converts the initial state spatial anisotropy to final state momentum anisotropy and elliptic flow. Several experiments [46, 47] at different energies have examined v_2 for the possible signature of thermalization of the produced medium. Substantial amount of study has been performed to inspect v_2 in low energy collisions at various beam energy ranges [48–50] availing variety of microscopic transport models [6, 51–53]. At low beam energies, change of sign, i.e., transition from

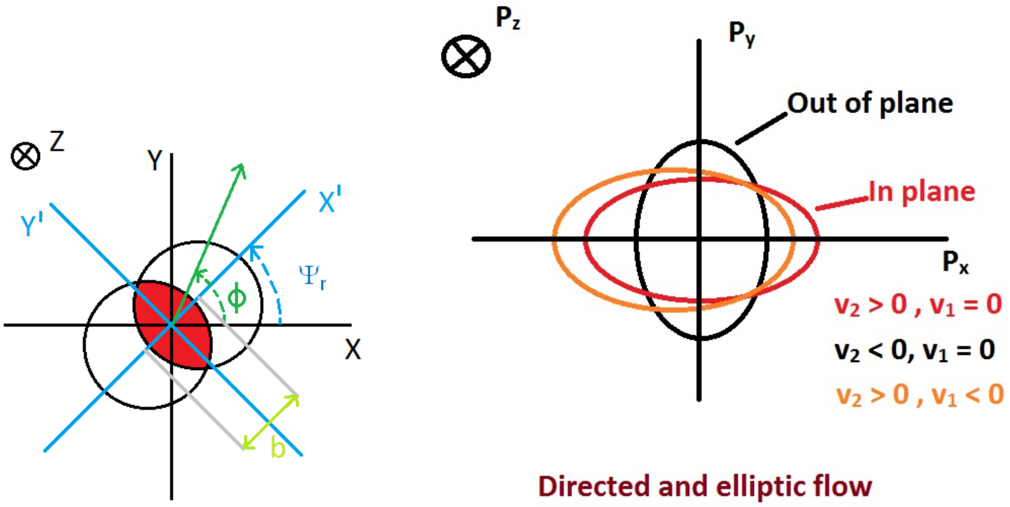

Figure 1.6: Representation of harmonic coefficients of azimuthal distribution of final state particles.

out-of-plane to in-plane flow, has been observed [54, 55].

1.5 Thesis Motivation

The main motive of the relativistic heavy ion collision experiments is to explore different regimes of the QCD phase diagram and identify the production of quark-gluon plasma in the laboratory. With the same motive, the CBM experiment at FAIR likes to explore the QCD phase diagram's high net baryon density region at moderate temperature. The CBM experiment will measure diagnostic probes of the dense stage of the fireball in the beam energy range of 2A GeV to 40A GeV for the first time, including multi-strange baryons, dilepton pairs, and charmed particles. Charm quarks are predicted to be created at the very initial stage of a heavy-ion collision. So the detection of D mesons and J/ψ could be used as probes to obtain information about the dense fireball and its degrees of freedom. Similarly, vector mesons like ρ and ω get produced at the initial stages and then decay either into mesons or dileptons. Their study is helpful in probing the hot and dense nuclear matter. Multi-strange hyperons and ϕ mesons, due to their small hadronic cross sections, can give information about the dense fireball region by looking at their collective flow. As a result, the CBM experiment offers a special potential for discovery at both SIS100 and SIS300 energies. CBM experiment is a fixed target experiment, where the incoming proton or ion beam will fall on a fixed target. Micro Vertex detector (MVD) is the detector placed closest to the target. The primary task of MVD is the reconstruction of D mesons through vertex detection. The Silicon Tracking System (STS), placed after MVD, will provide the track reconstruction facility for a wide range of momentum from 100 MeV to 10 GeV with a momentum resolution of around 1%. MVD and STS detectors will be placed inside the magnetic field region. After that, Ring Imaging Cherenkov (RICH) detector or Muon Chamber (MuCh) system will be placed depending on whether we detect electrons or muons. A Transition Radiation Detector (TRD) is placed after the RICH detector to detect electrons with a momentum of more than 1.5 GeV/c. Further, a time-of-flight (TOF) detector made up of layers of Resistive Plate Chambers (RPCs) will be used to detect charged hadron particles. A Projectile Spectator Detector (PSD) will be placed at the end of the setup to determine the centrality of the collision and orientation of the reaction plane. As a contribution to the CBM experiment, India is developing the MuCh detector for the CBM. The MuCh detector is made up of slices of the hadron absorbers and detector layers. The detector layers in triplets are placed in between these hadron absorbers for track reconstruction. The whole MuCh detector setup could be modified during the data-taking process. The number of detector layers and hadron absorbers could be modified depending on the beam energy. Due to the compact design of the MuCh detector, the heat produced due to the electronics of the detectors could be an issue. This motivates us to investigate this issue and develop a cooling system to extract the excess heat caused by the electronics of the MuCh detector using demineralized water as a coolant. A prototype has been created using three prototype cooling modules to investigate the working and configuration of the cooling system.

While constructing an experimental setup, it is necessary to do the simulation study as well for the better performance of the detectors. We have contributed to the simulation study in terms of data rate study where we predict the maximum pad hit rate for each station of the CBM MuCh detector to get an estimate about the minimum requirement of data rate handling capacity of a detector that is used in the CBM MuCh detector. In another simulation study, we used the Particle Identification (PID) framework to detect hadrons more efficiently at a higher transverse momentum range where traditional methods fail to work.

As we know, relativistic collisions of heavy ions allow inspection of the phase structure of the strongly interacting matter produced in the laboratory over various temperatures and densities. One of the many objectives of these collisions is to locate the QCD critical point and the phase transition to the deconfined matter as per the various QCD predictions. The high temperature and vanishing baryon chemical potential (μ_B) region of the QCD phase diagram are pretty well explored in the experiments operating at the Large Hadron Collider (LHC) [56–58] at CERN, Geneva and Relativistic Heavy Ion Collider (RHIC) [59, 60] at BNL, USA. On the contrary, the realization of the QCD matter produced at high μ_B is somewhat limited. Such investigation will be carried out in the upcoming CBM experiment at the FAIR facility at GSI, Germany, and a few other future facilities like NICA at JINR, Dubna and BES program at RHIC. Due to technical limitations at these energies, previous experiments like HADES [61] at GSI, Kaon Spectrometer (KaoS) [62] at GSI, Alternating Gradient Focusing (AGS) [63, 64] experiments at BNL, NA49 [65] experiment at CERN SPS could not address problems associated with the rare probes. Thus, in addition to this, as well as for the optimal utilization of the new upcoming facilities, it is essential to investigate the data available from previous experiments at similar beam energy regimes via model-based studies and provide predictions for future experimental measurements. This motivates us to pursue phenomenological study on the effect of different equations of state and beam energy and the effect of different particlization scenarios provided by the model on variables like anisotropic flow, and particle production by looking at particle ratios and net-proton rapidity spectra for low-energy heavy ion collisions.

1.6 Thesis layout

The thesis is organized in the following manner:

In chapter 1, we have introduced high-energy physics by discussing the early stage of the Universe, the Standard Model, and QCD. A description of the QCD phase diagram and quark-gluon plasma has also been provided. Finally, we talked about the motivation of the thesis.

In chapter 2, a brief description of the FAIR facility has been provided. CBM experiment and its detectors are explained in detail.

In chapter 3, we present a detailed study of the cooling system of the MuCh detector in the CBM experiment. The working principle and the design of the cooling system have been discussed. Different configurations for the modules of the MuCh cooling system have been compared.

In chapter 4, first, the CBMROOT framework for the MuCh detector has been discussed in detail. The simulation study of the CBM experiment in terms of data rate handling capacity of the MuCh detector and hadron study using a PID framework are explained further.

Chapter 5 explains the phenomenology work related to the study of anisotropic flow and particle production for low-energy heavy-ion collision. We look at the effect of different equations of state, particlization scenarios, and beam energy for better tuning of the UrQMD model.

In chapter 6, finally, the results and outcomes of the thesis have been summarized.

Chapter 2

CBM experimental facility at FAIR

This chapter provides a detailed explanation of the FAIR facility. More information is provided on the CBM experiment and the detectors used in it. The functioning and construction of the GEM detector employed in the MuCh detector system are described in detail.

2.1 FAIR facility

The Facility for Antiproton and Ion Research (FAIR) is an idea proposed by the international science community and the GSI Laboratory. FAIR will provide world-class accelerator and experimental facilities for a wide range of groundbreaking research in nuclear, hadron, atomic, and plasma physics. The main focus of FAIR research is on the formation and dynamics of matter at both the microscopic and cosmic levels, allowing us to gain a better understanding of fundamental topics such as the source of the elements in this world, evaluation of matter and its compositions in the early time period of the universe, the internal structure of the matter at extremely high temperature and baryon densities that we observe in large astrophysical objects, and understanding the complex structure of matter at all scales by looking at the underlying components and interactions.

The FAIR offers four scientific projects that aim to investigate several physical regions: APPA, PANDA, NuSTAR, and CBM. The Atomic, Plasma Physics and Applications (APPA) facility provides shared installation and experimental techniques for studies in quite diverse research fields of atomic physics, plasma physics, and applied science. APPA covers four different collaborations of different fields under one roof, which are the High-Energy Irradiation Facility for Biophysics and Material Research

(BIOMAT), Facility for Low-Energy Antiproton and Heavy Ion Research (FLAIR), High Energy Density Science at FAIR (HED@FAIR), and Stored Particles Atomic Physics Research Collaboration (SPARC).

Proton ANtiproton Detector Array (PANDA) tries to study every aspect of antiproton-proton collision related to various topics around weak and strong forces, exotic states of matter, and the structure of hadrons.

Nuclear Structure, Astrophysics, and Reactions (NuSTAR) collaboration will use the new accelerator facilities at FAIR for basic science with a focus on the structure of atomic nuclei, nuclear astrophysics, and nuclear reactions. The Superconducting Fragment Separator (Super-FRS) is the central device of the NuSTAR collaboration. It will be able to produce rare isotopes of all elements up to uranium at relativistic energies and separate them within a few nanoseconds, enabling the study of very short-lived nuclei.

The CBM experiment aims to explore the QCD phase diagram in high net baryon density and moderate temperature regions. We have discussed the CBM experiment in more detail in the further part of this chapter.

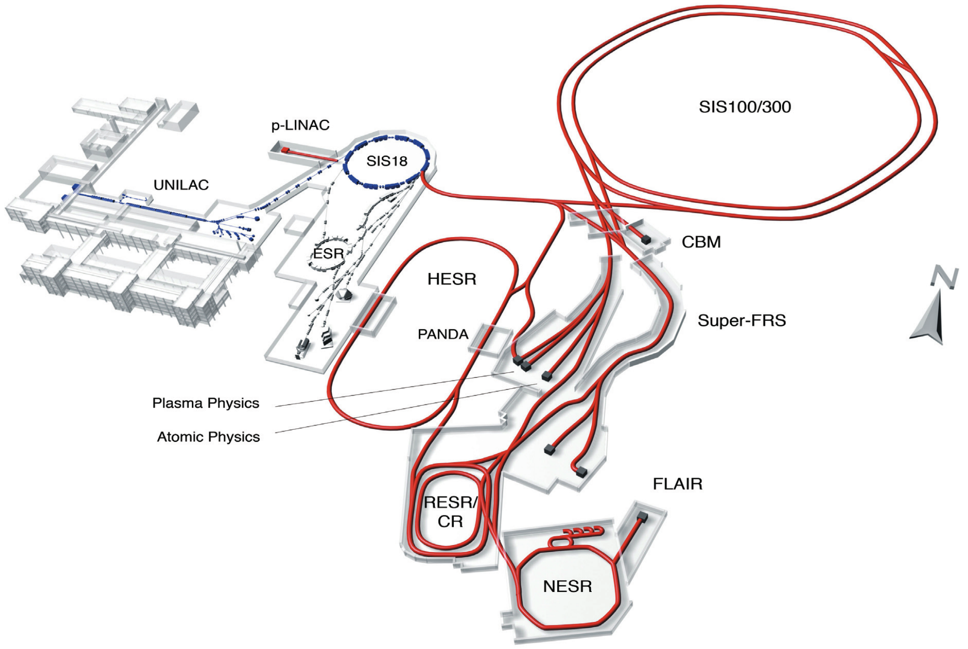

Figure 2.1: Layout of the Facility for Anti-proton and Ion Research (FAIR) [66].

The primary goal of FAIR is to provide stable and unstable nuclei, as well as antiprotons, in a wide range of intensities and energy for the scientific projects mentioned above. Figure 2.1 depicts the proposed FAIR layout as well as the present GSI facilities. SIS100 and SIS300 are two heavy-ion synchrotrons (SIS)[1] which will be used by the FAIR. UNILAC and SIS18 are the existing GSI accelerators that will act as injectors for the new synchrotrons. p-LINAC is the proposed extension to the GSI facility.

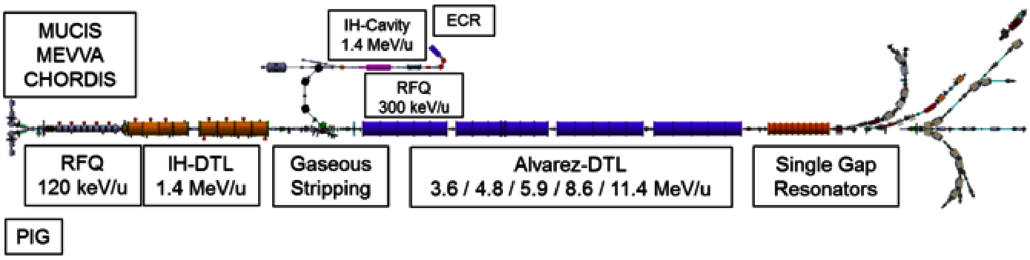

Figure 2.2: Layout of UNILAC, Image Source: [67].

Ion acceleration begins with the UNILAC (UNIversal Linear ACcelerator) shown in Figure 2.2. It is of length 120 meters. Three different ion sources provide charged ions to UNILAC as per requirement: Electron Cyclotron Resonance (ECR) source provides a low-intensity beam of highly charged ions. If a low-intensity beam of low to intermediate-charged ions is required, then Penning Ionization Gauge (PIG) source delivers it. High-intensity beams of low to intermediate-charged ions are delivered by MEtal Vapor Vacuum Arc (MEVVA) source, MUlti-Cusp Ion Source(MUCIS), or Cold or HOt Reflex Discharge Ion Source (CHORDIS). It has the ability to accelerate all ion species, from protons to uranium (2.2A keV to 120A keV), to 16% of the speed of light. UNILAC is capable of running at a 50 Hz repetition rate. Between two continuous beam pulses, the beam parameters such as ion species, energy, intensity, and beam target area can be changed. As a result, numerous different experiments requiring various sorts of beams can be provided in a quasi-simultaneous manner.

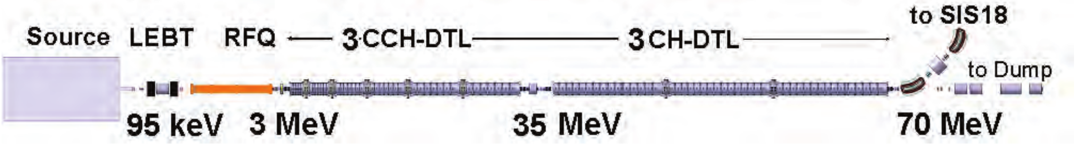

Figure 2.3: Layout of p-LINAC, Image Source: [68].

The antiproton physics program of FAIR is based on a rate of 7×10^{10} cooled antiprotons per hour. Initially, it requires the primary proton intensities which will be provided by a proton LINAC (p-LINAC) shown in Figure 2.3. It will run independently

---

[1] SchwerIonenSynchrotron in German

from the existing UNILAC for heavy ions. p-LINAC is 30 meters in length and has the ability to accelerate protons up to 70 MeV. Its repetition rate is 4 Hz. Protons are supplied to p-LINAC using Radio-Frequency Quadrupole (RFQ) LINAC and Drift-Tube Linac (DTL) at the starting point. Ions from the UNILAC or protons from p-LINAC will be employed in the experiments, or they are injected into the SIS18 ring accelerator for further acceleration.

To create antiprotons, the accelerated protons from LINAC are injected into the existing synchrotron SIS18 and accelerated to 2 GeV. After the subsequent transfers to the SIS100 synchrotron, the protons will be accelerated to 29 GeV. Up to 2×10^{13} protons will be compressed into a single short bunch of fewer than 50 ns in length to minimize the heating in the antiproton production target. The proton bunch will be directed onto a nickel target of about 60 mm in length followed by a magnetic horn. The cycle of proton acceleration will be repeated every 10 s. This scheme is expected to produce a bunch of at least 1×10^{8} antiprotons in the phase space volume which can be accepted by the magnetic separator and the Collector Ring (CR). The CR will be used for pre-cooling of the antiprotons. Thereafter, the antiprotons will be moderately compressed to a single bunch and transferred to the RESR storage ring.

Moving back to SIS18, it has a circumference of 216 meters and its maximum magnetic rigidity (Magnetic field intensity (B) × Radius of curvature (r)) is 18 Tm. The SIS18 ring shown in Figure 2.4 includes 12 double dipole magnets with magnetic quadrupole triplet or doublet focusing in each of the 12 sections. Two rf-cavities with a frequency range of 800kHz up to 5.6 MHz apply 32 kV acceleration voltage each. Ions circulate in SIS18 while passing through these 12 acceleration structures (sections). Magnets keep ions on their circular path. The kinetic beam energy per nucleon for any particular beam depends on the maximum magnetic rigidity of the accelerator as follows:

$$\frac{E}{A} = \sqrt{(0.3 \times B.r \times \frac{Z}{A})^2 + m^2} - m \tag{2.1}$$

where $\frac{E}{A}$ represents the kinetic beam energy per nucleon. $B.r$ is the maximum magnetic rigidity of the accelerator. Z, A, and m represent the atomic number, atomic mass, and mass of the particle respectively.

The ions from UNILAC can be accelerated up to 90% of the speed of light by

SIS18 (proton up to 5 GeV, U up to 1A GeV, Ne up to 2A GeV). It directs ions to the experimental storage ring (ESR) for storage and further analysis or injects them into the FAIR synchrotrons SIS100 and SIS300.

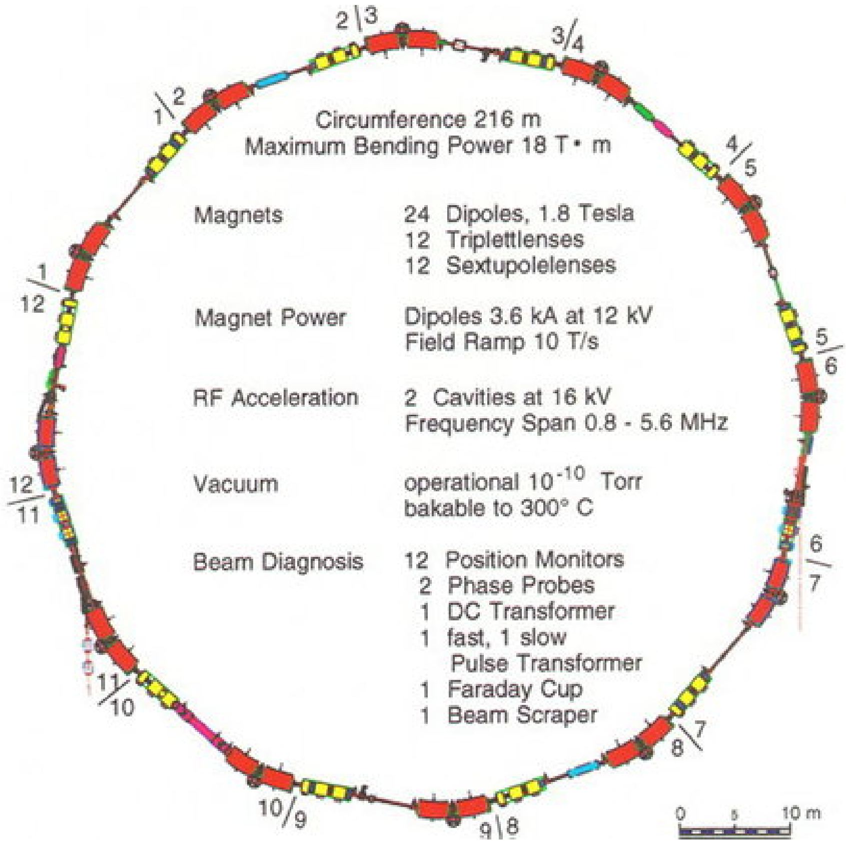

Figure 2.4: Layout of SIS18 synchrotron, Image Source [69].

The SIS100 and SIS300 ring accelerators will work in an underground tunnel at 17 m depth under the earth's surface. SIS100 and SIS300 have a circumference of 1100 meters providing around 7 km of distance in one rotation. SIS100 accelerates the ions up to a speed equal to 99% of the speed of light. It can accelerate all ions from Protons to Uranium (Protons up to 29 GeV, Au up to 11A GeV, nuclei with Z/A=0.5 up to 45A GeV). The magnets used here to keep the ions on tracks are superconducting and cooled by using liquid helium to a temperature of $-269°C$. The accelerated particles are used for the experiment directly or get further accelerated by SIS300. Figure 2.5 shows the layout of SIS100 and SIS300 accelerators.

SIS300 accelerates the ions up to the maximum extent possible by FAIR facility (protons up to 90 GeV, Au up to 35A GeV, nuclei with Z/A=0.5 up to 45A GeV). The two-stage acceleration idea, which will be implemented with the SIS100 and SIS300

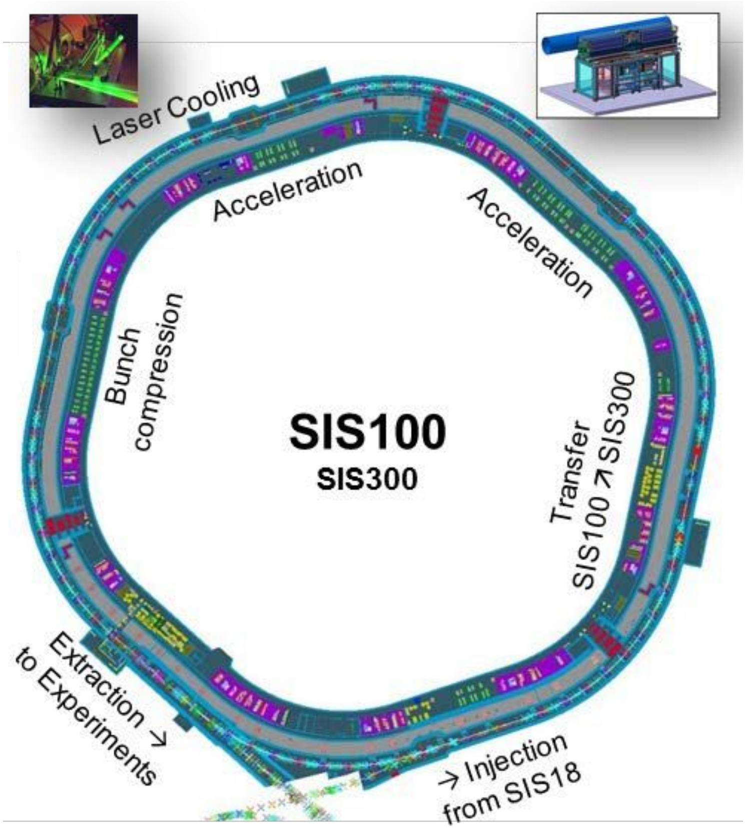

Figure 2.5: Layout of SIS100 and SIS300 accelerators.

synchrotrons, provides a real-time parallel experiment supply with beams of varying qualities. SIS100 and SIS300 synchrotrons feed ions to all four scientific projects which will function under the FAIR facility.

2.2 Compressed Baryonic Matter (CBM) experiment

CBM experiment is one of the major scientific projects at FAIR. CBM experiment is a fixed target experiment that will explore the QCD phase diagram in the region of high net baryon density and moderate temperature in heavy ion collisions. CBM experiment will have a high interaction rate of 10 MHz in the beam energy range of 2–45A GeV. At such a high interaction rate, luminosity will be high, which makes the detection of rare probes like charmonium (J/ψ) and low mass vector mesons (ρ, ω, ϕ) possible via dileptonic decay channel. The CBM experimental program will overall study the physics cases like the study of equations of state of baryonic matter at neutrons star densities, in-medium properties of hadrons, the phase transition from hadronic matter to the partonic matter at high net-baryon density, hypernuclei, strange dibaryons and massive strange objects, charm production mechanisms, charm propagation, and in-medium properties of charmed particles in dense nuclear matter.

For these studies, the final CBM experimental setup should be capable of identifying hadrons as well as leptons. The CBM experimental setup is prepared in such a way that it could be modified for the detection of electrons or muons coming from the decay of rare probes. It will be beneficial to match the output result from both ends to give a reliable conclusion. The layout of the CBM experiment can be seen in Figure 2.6.

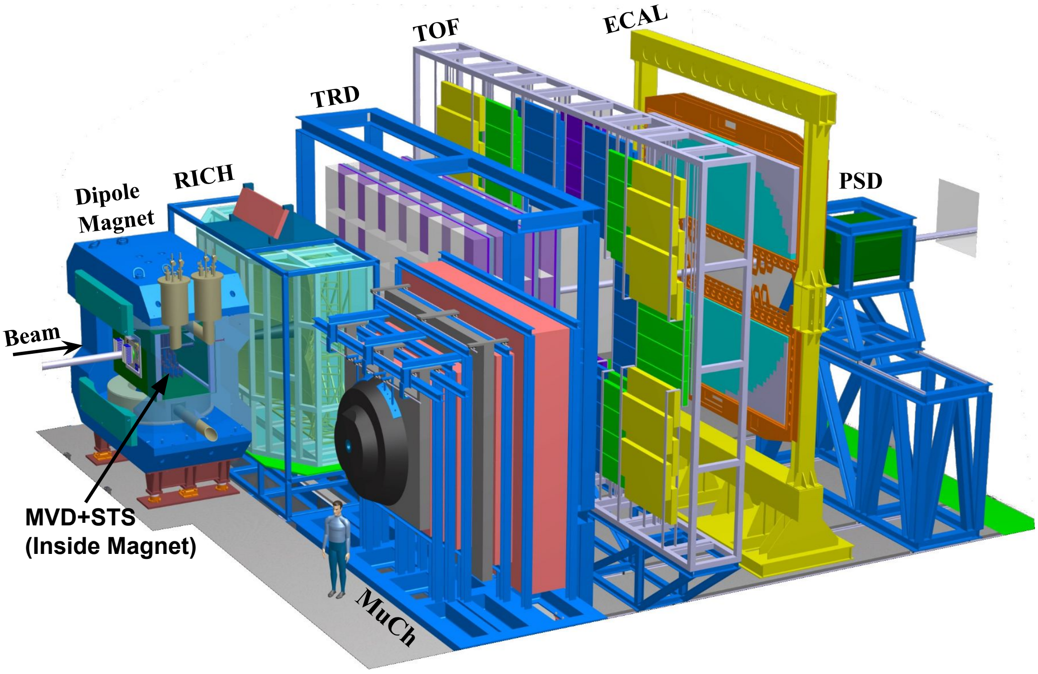

Figure 2.6: Systematic layout of CBM experimental setup.

More detailed explanations of detectors used in CBM experiment are as follows:

2.2.1 Dipole Magnet

In the CBM experiment, target, MVD, and STS detectors are placed within a magnetic field region generated by an H-type superconducting dipole magnet, as shown in Figure 2.7. This dipole magnet has a magnetic gap of 1.4 m where MVD and STS detectors are placed. Its total length is 1.5 m with a magnetic field region of 1 m along the beam axis with an average value of 1 T. Here, the angular acceptance of the dipole magnet is ±25° in the vertical direction and ±30° in the horizontal direction, measured from the target. In this dipole magnet, superconducting coils are used to reduce operational costs. The indirect cooling is provided to the coils using liquid helium at 4.5° K. More details about dipole magnet could be found in its technical design report [70].

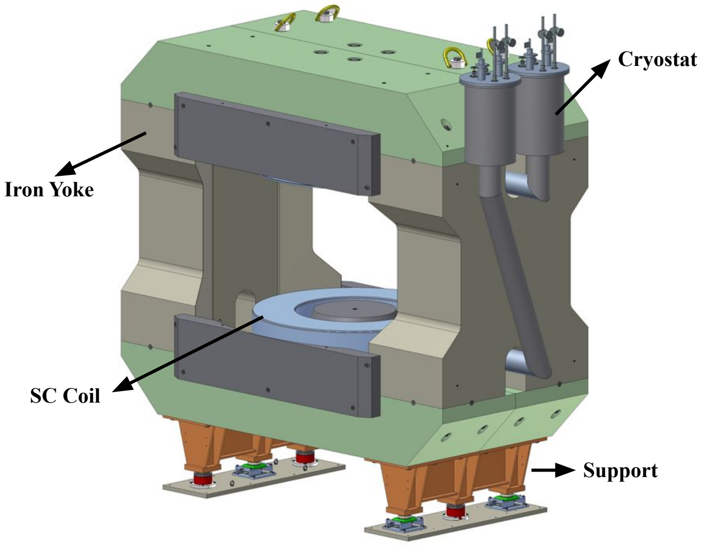

Figure 2.7: The layout of superconducting dipole magnet used in CBM experiment. Ref. [71]

2.2.2 Micro Vertex Detector (MVD)

Micro Vertex Detector measures the secondary vertex of D-mesons with a resolution of 50-100 μm along the beam axis. As MVD will be placed near the interaction point, it will experience a high particle rate, up to 10^{10} particles per second. While determining the decay vertices of charmed mesons (cτ = 122.9 μm for D° mesons and cτ = 311.8 μm for $D^{\pm}$ mesons), the detectors should have high position resolution and low material budget to suppress the multiple scattering. The Monolithic Active Pixel Sensors (MAPS) can fulfill these criteria. MAPS are based on the silicon detector technique, which allows the integration of detector elements and processing electronics on the same substrate. It's pixel size is in between (18 x 18) μm^2 and (20 x 40) μm^2. It provides (3.5 - 6) μm of position resolution depending on the pixel size. The MVD will have four layers of detector stations made up of MAPS as shown in Figure 2.8. More details about MVD could be found in its technical design report [72].

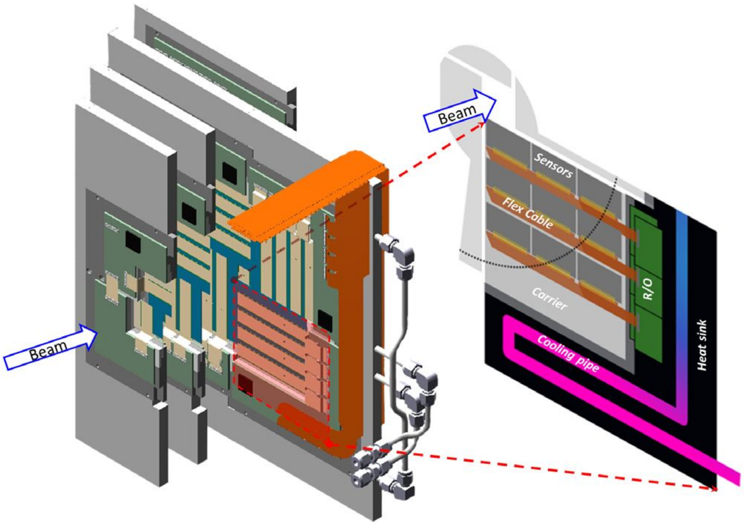

Figure 2.8: Visual layout of Micro Vertex Detector of CBM experiment. The third layer is shown briefly.

2.2.3 Silicon Tracking System (STS)

The STS detector is one of the most important components of the CBM experiment. The STS detector consists of 8 tracking layers of detectors based on silicon micro-strip sensors. As shown in Figure 2.9, these layers cover the aperture between 2.5° to 25° polar angle. These are placed 30 to 100 cm away from the interaction point in the direction of the beam axis. The number of layers of the STS detector is decided based on the precision required in the track fitting as well as material budget, cost, space, etc. It provides us with the momentum of the charged particles produced during the collision based on the bending of all charged particles. In this case, momentum resolution should be of the order of $\Delta p/p = 1\%$, and the efficiency of hit reconstruction should be greater than or equal to 95%. This can be achieved with an ultra-low material budget of range 1% X_0 per tracking station where X_0 is the radiation length of silicon. It will help minimize the multiple Coulomb scattering and achieve the required momentum resolution. In STS, double-sided micro-strip sensors are used of the thickness of 300 μm of silicon (approx 0.3% X_0). These sensors send the signal through multi-line micro-cables made up of sandwiched polyimide-Aluminum layers of a few 10 μm thickness which is approximately 0.17% X_0. More details about the STS detector could be found in its technical design report [73].

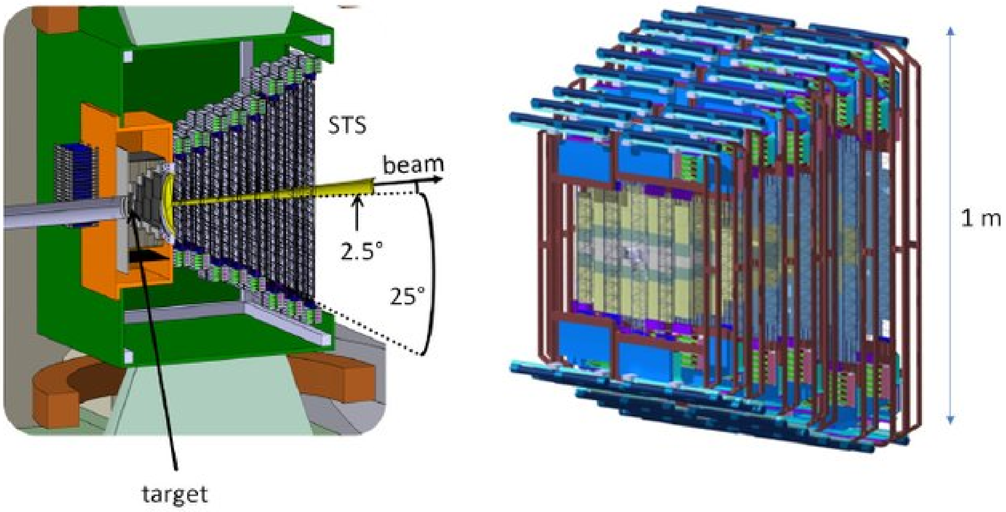

Figure 2.9: Conceptual design of the Silicon Tracking System, (left). The ensemble of eight tracking stations is to be mounted on the detector's main support frame (right).

2.2.4 Ring Imaging Cherenkov Detector (RICH)

The primary objective of the RICH detector is to identify electrons and suppress pions in the momentum range below 10 GeV/c. A gaseous RICH detector with focusing mirror components, a photodetector, and a conventional geometric design will be used to accomplish this. The RICH detector will be placed at 1.6 m distance from the target along the beam axis. The gas radiator will be of size 1.7 m, along with two sets of mirrors and photodetector planes as shown in Figure 2.10; the overall length will be around 2 m. The mirror plane is divided lengthwise into two arrays of spherical reflectors made up of glass mirrors, each measuring (4 x 1.5) m^2. The 80 mirror panels have Al+MgF_2 reflecting coating and of 6 mm thickness with a curvature of 3 m radius. Cherenkov radiation rings will be forecasted onto two photodetector planes (2 x 0.6) m^2, which are placed after the dipole magnet and protected by magnet yokes. CO_2 will be used as the radiator gas, which has a Cherenkov threshold for pions of momentum 4.65 GeV/c. Above the threshold value, pions could be distinguished from electrons up to 10 GeV/c based on Cherenkov opening angle. To deliver high precision, high geometrical acceptability, and high detection efficiency of photons, Hamamatsu H8500 Multi-Anode Photo Multiplier Tubes (MAPMTs) [74] are used. More detail about the working of the RICH detector could be studied in its technical design report [75].

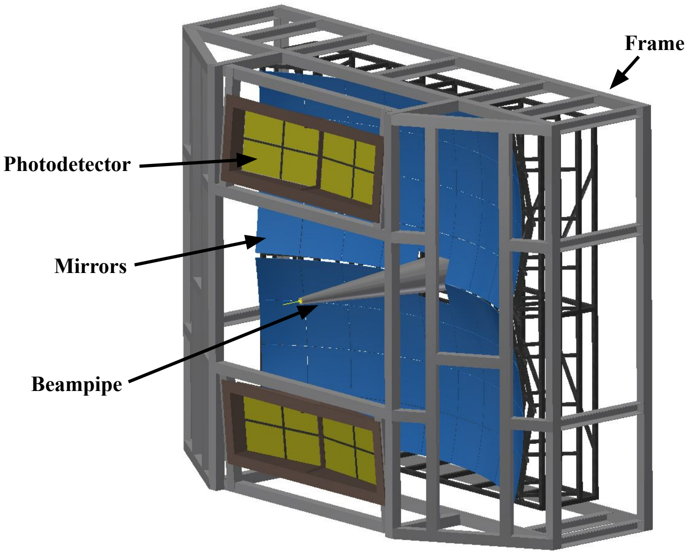

Figure 2.10: Technical design of RICH detector.

2.2.5 Muon Chamber System (MuCh)

The CBM aims to track the particles using a hadron absorber setup and identify muons based on their momentum. The hadron absorber is divided into many layers, and triplets of tracking detector planes are inserted into the spaces between the layers of the absorber as shown in Figure 2.11. The final design consists of 6 hadron absorber layers and 18 gaseous detector layers arranged in triplets after every hadron absorber. This muon detector system is located after the Silicon Tracking System (STS), which calculates the particle momentum. The momentum of the muon, which varies with the mass of vector mesons and beam energy, plays an important role in its identification. At a reaction rate of 10 MHz, the first detector layer after the first absorber will face a maximum hit rate of 3 MHz/cm^2 (0.3 hits/cm^2 per central event). Due to absorber layers, the particle multiplicity will be low at the last tracking station. The trigger concept can be used by measuring small track segments from the last triplet and extrapolating tracks to the target. By selecting good tracks with detected vertices, the event rate is reduced by a factor of about 600 in a simulation study. Further details of the MuCh detector are explained in its technical design report [3].

Finding low-momentum muons in a scenario with high particle density is a problem for experimental muon observations in heavy-ion collisions at FAIR energy. If a single thick absorber is used in the detector, it will absorb hadrons as well as low-

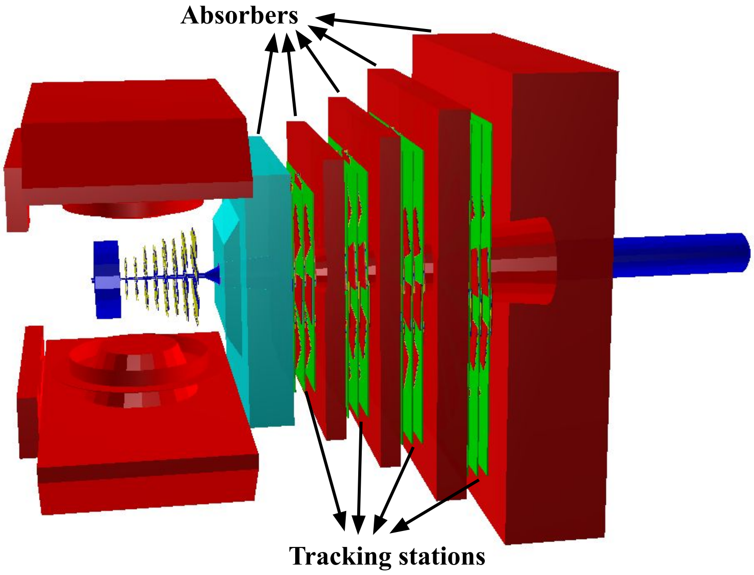

Figure 2.11: Simulated layout of MuCh detector in SIS100 setup.

momentum muons. To study low-mass vector mesons, it is necessary to detect these low-momentum muons with higher efficiency. A lot of simulation study has been done to optimize the size of absorbers, number of absorbers, number of tracking stations, etc. GEANT3 transport engine is used for these simulation studies. Figure 2.12 shows the effect of the thickness of the iron absorber on different particles when a central Au-Au collision takes place at 25A GeV. The number of particles is normalized for a better comparison. Based on this figure, we could estimate the required thickness of absorbers to detect low-mass vector mesons. Muons coming from the decay of J/ψ mesons are not absorbed even after 250 cm of thickness. After around 250 cm of thickness, muons from ω mesons get absorbed by 10 factors more compared to the muons coming from J/ψ mesons. If we compare muons from ω mesons with pions and protons, the signal-to-background ratio (S/B) will not increase after 150 cm of absorber thickness. So to detect low-mass vector mesons, up to 150 cm of the thickness of the absorber is quite favorable. To detect muons from charmonia, an additional absorber of thickness 100 cm is required to be added with additional detector layers. The thickness and material of individual absorber layers have been optimized as well based on their ability of hadron absorption and multiple scattering, which are explained in more detail in [3].

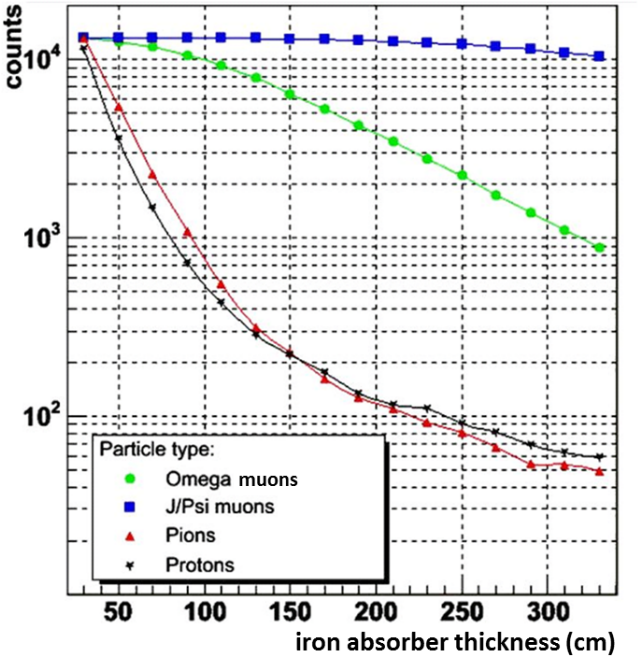

Figure 2.12: Number of different particles as a function of distance traveled in the iron absorber in case of central Au-Au collision at 25A GeV beam energy. Number of different particles has been normalized. Ref. [3]

CBM experiment will cover a wide range of beam energy provided by the accelerators SIS100 and SIS300. The FAIR facility is decided to build in different phases. In the first phase, only SIS100 will be able to accelerate the particles. SIS100 could provide beam energy for Au ions up to 11A GeV. In the second phase, SIS300 will be functional and could provide a beam of up to 45A GeV. The MuCh detector is planned to be built in such a way that it can be easily upgraded depending on the incoming beam energy. Different designs are planned for the MuCh detector depending on the following requirements: a) The thickness of absorbers will be fixed after their construction, and their position will also be fixed. The first absorber will always be 60 cm carbon slice, b) tracking stations will have three layers each, and the number of tracking stations will depend on the physics requirement strictly; for example, for charmonium detection, an additional 1 m of the absorber and one tracking station will be added to increase the number of tracking points, c) different detector layers will be constructed based on their required rate handling capability, size, and cost. Table 2.1 shows the evolution of MuCh detector configurations. The first absorber layer will be the same for all configurations. In addition, a few layers of iron absorbers will be added depending on the beam energy and particle study. Different technology could be used according to the requirement at different stations of the MuCh detector. The initial few stations will face heavy radiation and interaction rate, so special technology is required to build initial stations. After that, later stations could use the conventional detector technology that could be useful to create large-area detectors. Different technologies could be used at different radial distances for the same station. Still, due to the complexity in it, it is decided to use the same technology to create three layers of a single detector station. The track-detecting layers in the first two tracking stations will be made up of Gas Electron Multiplier (GEM) detectors. Further next two tracking stations are decided to be made of Resistive Plate Chambers (RPC).

MuCh Configurations	**Number of iron absorbers**	**Total thickness of iron absorbers**	**Number of Tracking Stations**	**Physics Case**
SIS100-A	2	40 cm	3	LMVM A + A 4-6A GeV
SIS100-B	3	70 cm	4	LMVM A + A 8-10A GeV
SIS100-C	4	170 cm	5	p + A (J/ψ) 29A GeV
SIS300-A	5	105 cm	5	LMVM A + A 15-25A GeV
SIS300-B	6	205 cm	6	(J/ψ) A + A 10-35A GeV

Table 2.1: Different setups of MuCh detector for SIS100 and SIS300.

Gas Electron Multiplier (GEM) Detector

Gas Electron Multiplier, as the name suggests, is a gaseous detector that has a unique structure of GEM foil as an advantage compared to other gaseous detectors. It is first developed at CERN [76, 77]. Each GEM foil consists of a 50 μm thick polyimide foil which is metalized on both sides by 5 μm thick copper layers. This GEM foil has a large density of holes ($\sim\ 50/m^2$), each hole of diameter 70 μm at 140 μm distance from each other. These GEM foils act as an amplifier of electrons which produce a very high electric field (100 kV/cm) inside the holes even when relatively low voltage

($\sim 400V$) is applied across the foil, placed inside a suitable gas volume. There is a remarkable growth in the technology for producing GEM foil. Initially, these foils were developed by using double mask technology in which two masks are used at the top and bottom layers of the foil before etching. This technology is nice to produce foils of sizes (10 x 10) cm to (30 x 30) cm of good quality. But the production cost was very high, and this technology could not be used to develop large-size foils which are required in the MuCh detector. As technology improves, RD51 collaboration at CERN produces foils using single-mask (SM) [78] technology where only one mask is used at the top of the foil for etching holes. The yield of the large-size foil increases the use of single mask technology, and it reduces the production cost. The copper-clad polyimide sheets, which are the raw materials for GEM production, are available as sheets of 50 μm thickness and of width 0.5 m. So by using single mask technology, GEM foils of width 0.5 m could be produced with lengths of 1m and more.

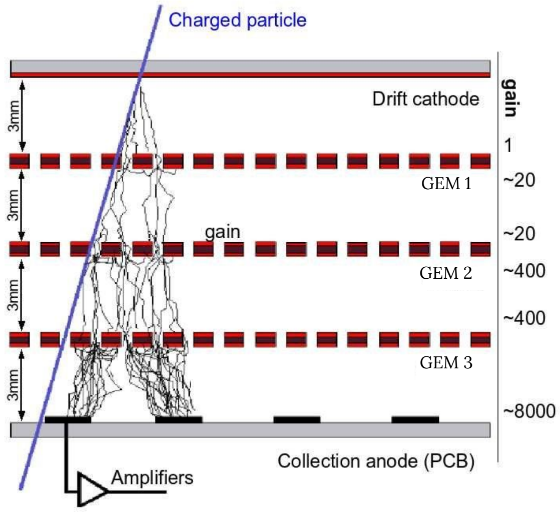

Figure 2.13: The layout of triple layer GEM detector.

In most of the practical applications, a sequence of GEM foils is used due to low gain and electron multiplication from a single GEM foil. To build a detector, these GEM foils are placed at a fixed distance from each other by using spacers. These are placed in a gas-tight chamber that is filled with a suitable gas mixture. These chambers consist of two Printed Circuit Boards (PCBs) at the top and bottom. The space between the top PCB layer and the first GEM foil acts as a drift gap. Primary ionization due to incoming radiation takes place in this drift gap region. Further GEM foils will amplify the signal by the drifting of electrons through the GEM holes. The gap between the

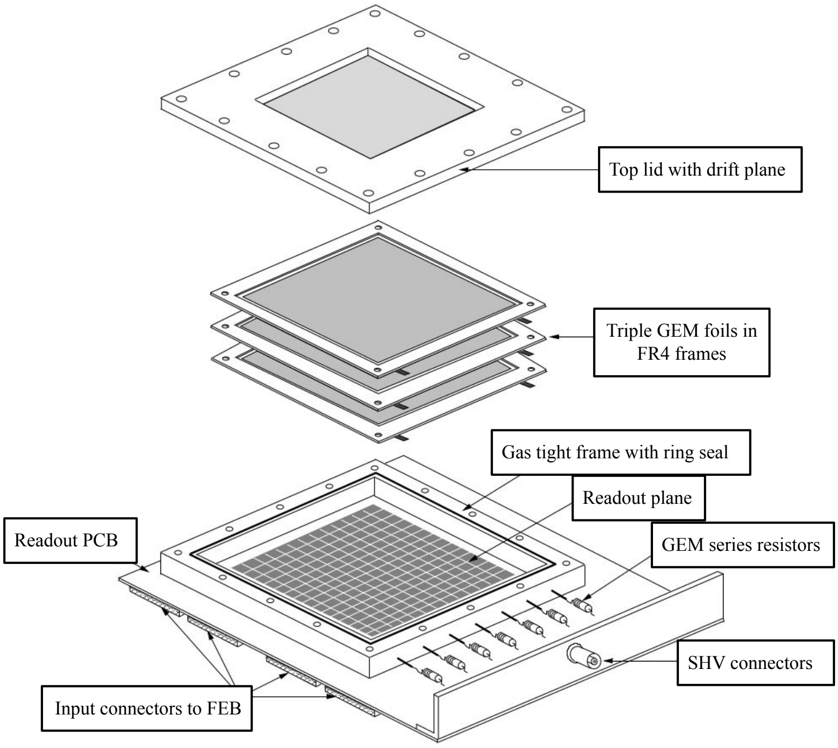

Figure 2.14: The assembling parts of triple GEM detector. Ref. [3]

last GEM foil and the bottom PCB layer act as an induction or collection gap. Suitable voltages are provided for all the gaps. These provided voltages could be the same for all the gaps or could be different, depending on the requirement of the application. These voltages lie in the range of 300-400 V. The gas mixture used in the detector chamber is mainly a mixture of Ar and CO_2 in the ratio of 70/30. This gas mixture makes the detector inactive for neutrons. In CBM MuCh detector, triple-layer GEM detectors are used. Using a triple GEM setup with an applied voltage of 400 V across all gaps and gas mixture of Ar/CO_2 of ratio 70/30, a gain of $> 10^4$ is attained with very low discharge probability of 10^{-11}. To prepare a triple GEM detector for any experiment, the components shown in figure 2.14 need to be assembled in the same order. The setup will be placed in an air-tight closed chamber where the top lid consists of a PCB for the drift plane. A gas-tight enclosure with a groove for O-ring seals is located on the bottom portion. On the sides, connectors are used to provide voltage to all segments from HV resistors. A set of multipin connectors at the bottom connect the Front-End electronic Boards (FEBs) and SHV connectors for HV input on the side. The three GEM foils of size 10 x 10 cm made by using single mask technology are placed in a gas-tight housing separated by suitable spacers for required gaps between foils. GEM detector technology has improved a lot in past years, and a number of high-energy experiments are using GEM detectors as tracking and readout devices. A few examples of experiments which are using GEM detector are TOTEM (TOTal cross section, Elastic scattering and diffraction dissociation Measurement) at the LHC [79], STAR (for Solenoidal Tracker at RHIC) experiment, PHENIX (for Pioneering High Energy Nuclear Interaction eXperiment) at RHIC [80], COMPASS (Common Muon and Proton Apparatus for Structure and Spectroscopy) at CERN, LHCb (Large Hadron Collider beauty) at CERN, LEGS (Laser Electron Gamma-ray Source) at BNL, and BONuS (Barely Offshell Nucleon Structure) at JLAB.

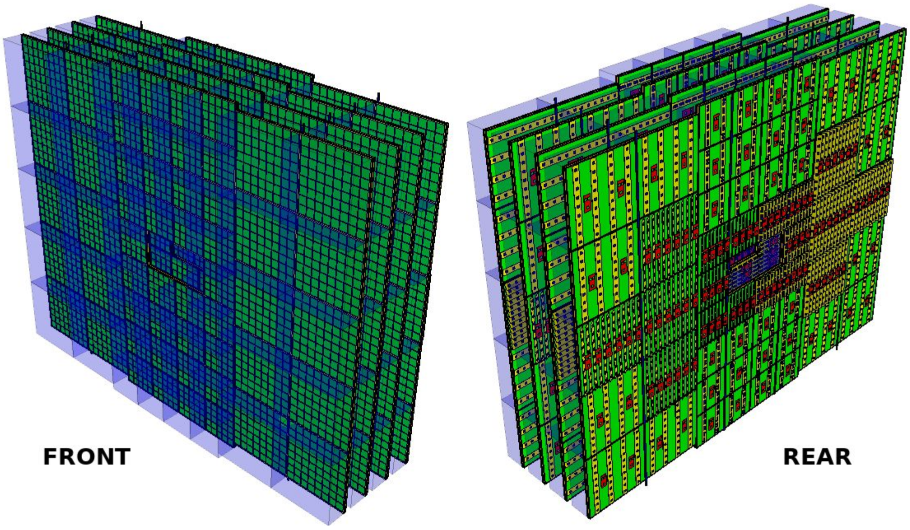

Figure 2.15: Front and rear view one TRD station consisting of four layers showing readout panels.

2.2.6 Transition Radiation Detector (TRD)

To monitor particles and identify electrons with momentum > 1 GeV/c ($\gamma \geq 1000$), Transition Radiation Detector will be used which will be placed in between the RICH and TOF detectors. The basic design of TRD consists of one station containing four detector layers for the SIS100 setup as shown in Figure 2.15 and ten layers in three stations for the SIS300 setup. These detectors will be placed at approximately 4.1 m to 5.9 m along the beam axis from the target. The TRD detector readout will be implemented as rectangular pads with 90-degree rotation at every second TR layer.

These readouts will provide a resolution of 300-500 μm across and 3-30 mm along the pad. The performance of prototype gas detectors based on MWPC and GEM technology has been evaluated at particle rates as high as 400 kHz/cm^2 without any loss. More details about these studies are explained in the technical design report of TRD [81].

2.2.7 Time-of-Flight Detector (TOF)

A series of resistive plate chambers will be employed for hadron identification using TOF measurements. The TOF wall covers a total of 120 m^2 active area for particle detection and is placed at a 6 m of distance from the target in the SIS100 setup and at a 10 m distance from the target in the case of the SIS300 setup. 80 ps of time resolution will be required to use it in CBM experimental setup. Prototype Multi-gap Resistive Plate Chambers (MRPCs) are manufactured with low-resistivity glass and have been successfully tested with a time resolution of 40 ps at 20 kHz/cm^2. Figure 2.16 shows the different types of detectors used in the production of the TOF wall. These detectors are explained in detail in the technical design report of TOF [82].

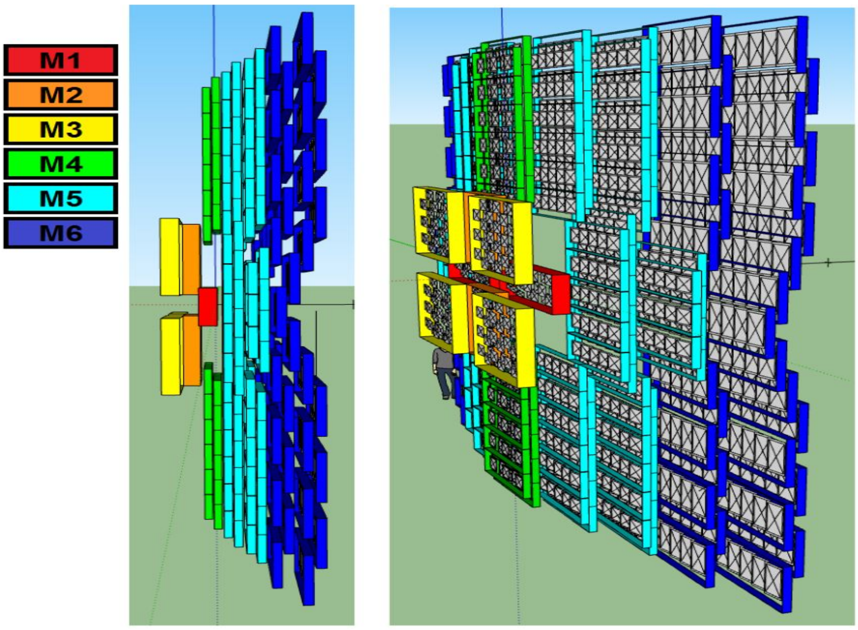

Figure 2.16: Side view and stretched view of TOF detector.

2.2.8 Electromagnetic Calorimeter (ECAL)

The ECAL will be used in the CBM experimental setup [83] to detect direct photons as well as decay photons coming from the decay of π° and η. A systematic layout of ECAL used in the CBM experiment is shown in Figure 2.17. This ECAL will be made up of modules that include 140 layers of 1 mm lead and 1 mm scintillator, having cells of sizes (3 x 3) cm^2, (6 x 6) cm^2, and (12 x 12) cm^2.

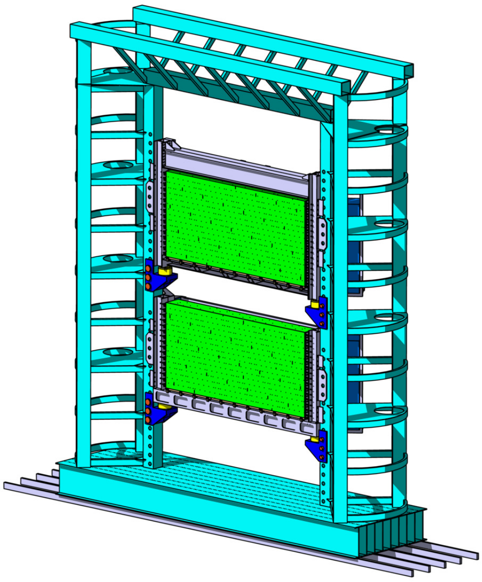

Figure 2.17: Simulated layout of Electromagnetic Calorimeter used in CBM experiment.

2.2.9 Projectile Spectator Detector (PSD)

The collision centrality and the reaction plane's orientation will be evaluated using the Projectile Spectator Detector (PSD). A clear description of the event is required to study event-by-event data sets. An accurate reaction plane must be determined to study collective flow using a method that does not include any of the collision's constituent particles. The detector's purpose is to count the non-interacting nucleons that are launched from a projectile nucleus during collisions between nuclei. This modular lead-scintillator hadron calorimeter will measure the energy of the projectile spectators and will also determine the transverse spectator coordinate for determining the reaction plane in every nucleus-nucleus collision. The PSD contains nine individual modules as shown in figure 2.18 of (20 x 20) cm^2 size in a set of (3 x 3). Each module has 60 layers of lead plates and scintillator tiles of thickness 16 mm and 4 mm, respectively. WLS fibers are placed in grooves of scintillator plates for a light readout setup. Further details are very well explained in the technical design report of PSD [84].

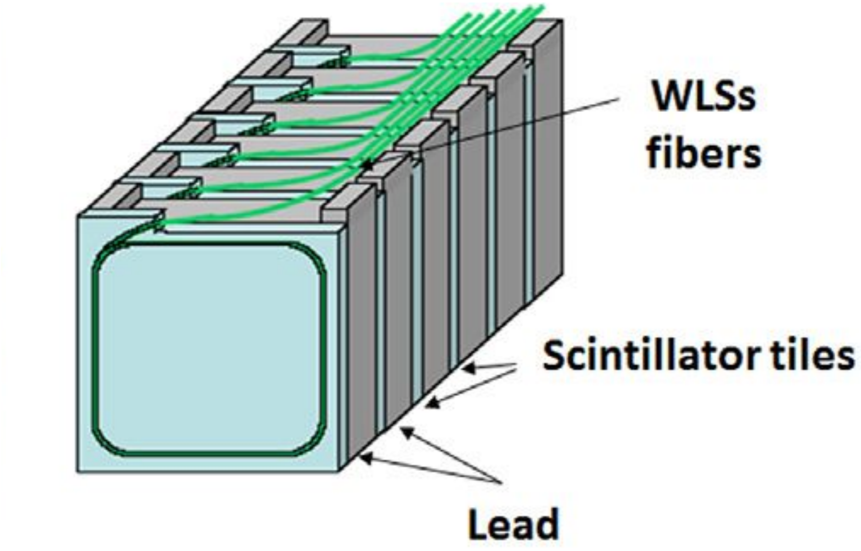

Figure 2.18: Systematic layout of one module of Projectile Spectator Detector.

2.2.10 Online event selection and data acquisition

High reaction rates are required for high statistics of particles which produced through a tiny production cross-section. The highest event rate for the CBM experiment will be 10 MHz which is 1% of the interaction target of beam intensity of 10^9 ions/s. So the CBM detector, data acquisition, and online event selection system should be capable of handling such a high rate. For example, if an archiving rate of 1 GByte/s and event volume is 10 kByte for minimum bias Au-Au collisions; then, the data acquisition could accept up to 100 kHz of event rate. So in case of an event rate of 10 MHz, the online event selection algorithms should be able to reject the background portion by a factor of 100 or more. The online event selection system is a fast online event reconstruction system running on a high-performance computer containing required cores and graphic cards (GSI GreenIT Cube).

Chapter 3

CBM MuCh detector cooling system

In this chapter, we go through our work on the design, construction, and test outcomes of the CBM MuCh detector cooling system as well as the research of its operating principle.

3.1 Requirement of cooling system

As we already know, detecting muons is highly challenging, particularly in low momentum range and in a high particle density environment. CBM overcame this challenge by instrumenting hadron absorbers segmented in several layers and installing a triplet of tracking detector planes in the gaps between each absorber pair so that even low-momentum muons could be detected. Besides the segmented design, the MuCh detector system (absorbers and detector stations) needs to be very compact as well to reduce the background muons from the weak decays of mesons (pions and kaons) which implies a minimum gap for tracking stations between the absorbers [3]. Each tracking station has three layers (triplets) of detector chambers divided into trapezoidal sector-shaped modules. The curvature of a station determines the number of sectors (or modules) per plane, and the particle flux determines the detector technology employed in different stations. The first and second stations of MuCh detector system will house GEM based detector modules.

The Front End electronic Boards (FEB) connected on modules of the MuCh detector system use a custom-built self-triggered Application-Specific Integrated Circuit (ASIC), which provides both timing and ADC information of each incoming signal to its channel. These FEBs dissipate heat while in operation. The FEBs used for the MuCh detector system are sensitive to the surrounding temperature and have a favorable temperature range of 20°C – 25°C for their operation. The detectors for the first two stations of the MuCh detector system are GEM-based, as discussed earlier, and the detector's gain is found to depend on the ambient temperature [85, 86]. Therefore, the stable running of the detector and FEBs requires a steady ambient temperature within the acceptable range, which in turn demands the necessity of continuous draining out of the generated heat. To meet the above requirement, a cooling system using demineralized water as a coolant is under investigation. The use of an air-based cooling system is ruled out because the interconnections of the FEBs are made using the wire bonding technique, which has the disadvantage of connections loosened or broken due to vibrations because of airflow.

In this chapter, we report on the working principle of the cooling system, mechanical design, fabrication, test performances of the prototypes, and the details of the control unit. This particular system is developed keeping the MuCh detector system of the CBM experiment in mind. However, the basic principle and technique studied here can be used elsewhere with proper customization of various parameters such as shape, size, thickness, and material type of the cooling plate. In general, this type of cooling system can be a good solution for places where large heat is generated in a very confined space.

3.2 Working principle and design considerations

As discussed earlier, the MuCh detector system in the CBM experiment consists of a combination of absorbers and detector layers. Due to its compact geometry, the gaps for MuCh tracking stations between the absorbers are kept as small as possible ($\sim$ 10 cm gap is available between two layers of a station). The FEBs of one MuCh module (sector) dissipates $\sim$90 W of heat while in operation, which implies on an average $\sim$4.3 kW and $\sim$5.4 kW of heat generation by the first (consisting of $16 \times 3 = 48$ modules) and the second (composed of $20 \times 3 = 60$ modules) MuCh stations respectively. This large amount of dissipated heat within a confined space results in a rise in temperature at the surface of the FEBs and their vicinity. A compact cooling system is required to meet the constraint. It is accomplished by pursuing a novel concept of using a single metal plate (with water channels grooved within) which can serve both as a mounting structure for the detector as well as a heat sink. The cooling system consists of several components, i.e., a cooling plate, microcontroller board, temperature sensors, water chiller, and suction pump. An aluminum plate with water channels inside serves the purpose of the heat sink. Considering the heat load, availability, and cost-effectiveness, demineralized water is preferred over other coolants such as methane, liquid nitrogen, CO_2, etc.

The FEBs of the detector module with metallic contact on the bottom side of PCB as shown in Figure 3.1 have been installed on one side of the cooling plate just above the water channels, using thermal glue for effective heat transmission. The heat generated from the FEBs is transmitted to the aluminum plate via this metallic contact. A continuous flow of chilled demineralized water is circulated through the water channels within the plate to drain the heat dissipated by the FEBs. Analog LM35 temperature sensors [87] are mounted on the surface of the cooling plate to measure the temperature of the heat sink (cooling plate).

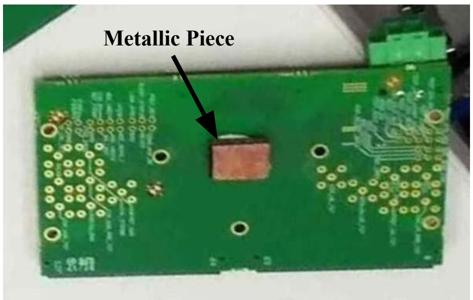

Figure 3.1: Back side of a FEB with metallic contact on it.

It is also essential that the cooling system does not bring down the temperature at the surface of the FEB below the dew point, which might result in the formation of water droplets from the condensation of vapor which is detrimental to the electronics. An automated mechanism is therefore required to control the coolant flow, thereby keeping the temperature around a fixed value. To achieve this, a microcontroller [88] based unit (see section 3.5) is used to keep the temperature of the heat sink at a constant value. By comparing the data from the temperature sensors to a reference temperature value, the microcontroller regulates the pump speed and water flow. A reference temperature is established as an external parameter in the microcontroller using a computer interface. Figure 3.2 shows the flow chart of the working principle.

When the temperature of plate rises above the reference temperature, the micro-

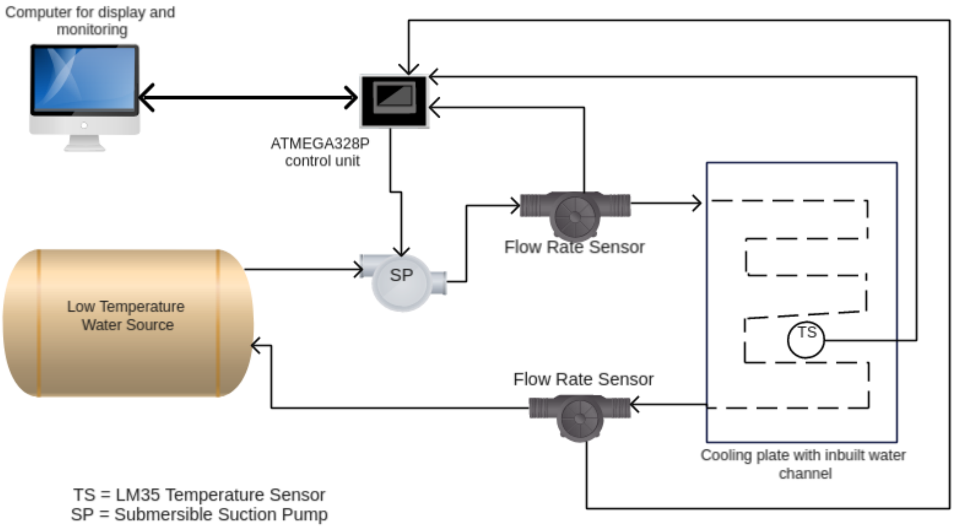

Figure 3.2: Flow Chart: Working principle of the cooling system.

controller turns on the re-circulation of chilled water through the plate and when the temperature of the plate falls below the reference temperature, it turns the flow off. The cycle is automated, and the temperature of the cooling plate is maintained at a predetermined reference point.

As discussed, the use of the cooling plate is twofold: as a supporting structure for mounting the detector modules and FEBs, and as a heat sink for cooling. The dimension, design, and the type of material of the cooling plate are therefore determined considering the factors like mechanical strength, planarity, ease in building water channels inside it, and property of good heat transfer. During the experiment, the system will be operated in a high-radiation zone, hence the material for the plate should have features like low radiation activity.

3.3 Copper-based small size prototype

A small-size prototype test is conducted in the laboratory to validate the proof-of-principle of the conceptual design of the cooling system [89, 90]. As shown in Figure 3.3 (left), a copper plate of thickness 1 mm and size 300 mm × 600 mm with copper tubes (6 mm in diameter) brazed on its top surface is used as heat sink.

Seven heating elements (coil resistors of 4 W dissipative power each) are also

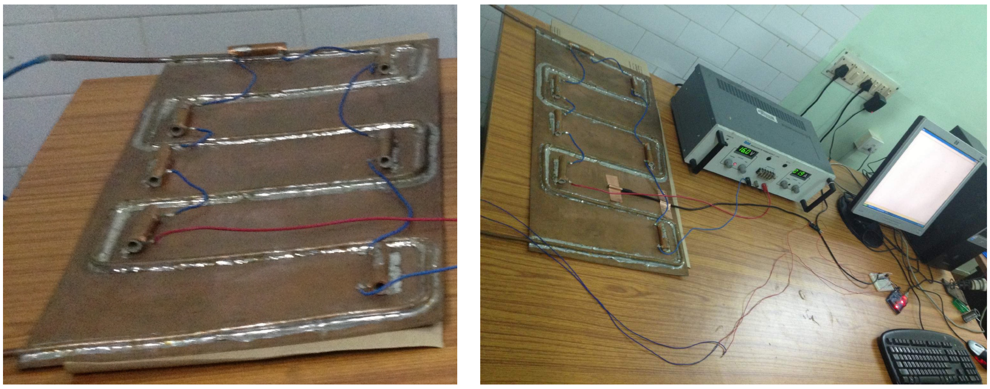

Figure 3.3: Small prototype: 1 mm thick copper cooling plate with copper tubes and heating elements brazed on it (left), the setup of the cooling system (right).

brazed on top surface of the copper plate (Figure 3.3 (left)) to emulate 28 W of heating load and powered by an external regulated power supply. A test setup is prepared as shown in Figure 3.3 (right) by appropriately connecting various components of the cooling system such as water tubes, suction pump, microcontroller, and temperature sensor etc.

The heating elements were turned ON to test the performance of the cooling system. The temperature of the copper plate and the water flow rate are observed for a few hours. The temperature of the copper plate went up in the beginning. As soon as it exceeded the reference temperature, re-circulation of chilled water through the copper tubes began and continued till the temperature dropped down below the reference temperature.

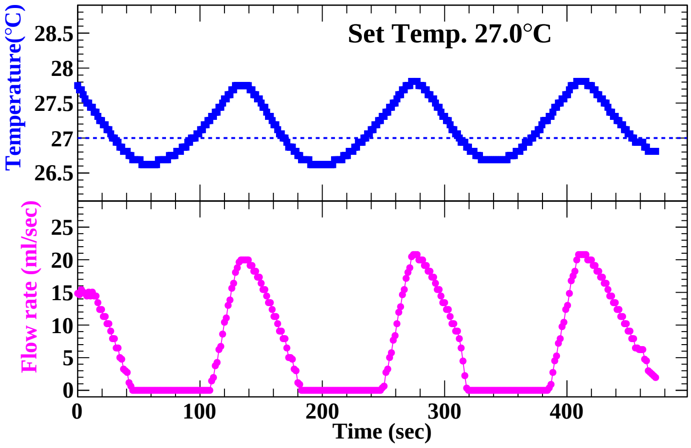

Figure 3.4: Surface temperature of the copper plate and water flow rate as a function of time at a reference temperature of 27°C.

Figure 3.4 shows the variation of temperature and water flow rate as a function of time for a selected period. The reference temperature is set at 27°C for this observation. The system is clearly able to maintain the temperature of the plate at a specified value by draining off the dissipated heat. In the actual experiment, we need the required temperature in the range of 20°–25°C. As the self-triggered electronics are used for the current design, small fluctuations in the biases of the ASIC will lead to huge noise, and more usable bandwidth will be consumed by noise data. It was observed that within 5° of temperature rise, there is a nominal increment in noise data, however with an increase of 10°, there is approximately 20-30% more noise is detected while comparing with 20° temperature. That is why, the range of 20°–25°C is selected. Beyond 35°C temperature, there are other noise effects that affect the working of the ASIC. By keeping 23°C as a reference, ±2°C change will be acceptable. The experiment is performed for various values of the set temperature. A variation of around ±0.7°C in the temperature about the reference value is observed, which is well within the acceptable range of ±2°C.

3.4 Mechanical design of real-size cooling plate

Considering several factors like radiation hardness, availability, and cost-effectiveness, an aluminum plate of thickness 10 – 12 mm (based on the fabrication technique) is suitable for building the cooling plate. The size of the plates of the first station modules is kept as 850 mm × 550 mm which is slightly bigger than the size of a MuCh module in the first station. One of the main challenging tasks in the mechanical design of the cooling plate is the fabrication of the water channels of 5 mm (6 mm) diameter inside a 10 mm (12 mm) thick aluminum plate without compromising the mechanical strength and planarity of the plate. The application of the drilling technique is also ruled out due to the larger size of the plate.

Two different techniques are therefore adopted for making water channels inside the plate as discussed below:

(I) Technique–I: In the first technique, on a 10 mm thick aluminium plate, T-shaped grooves are made from the top side. First, an 11 mm wide and 3 mm thick portion is removed along the length of the plate, then a 5 mm thick and 5 mm wide

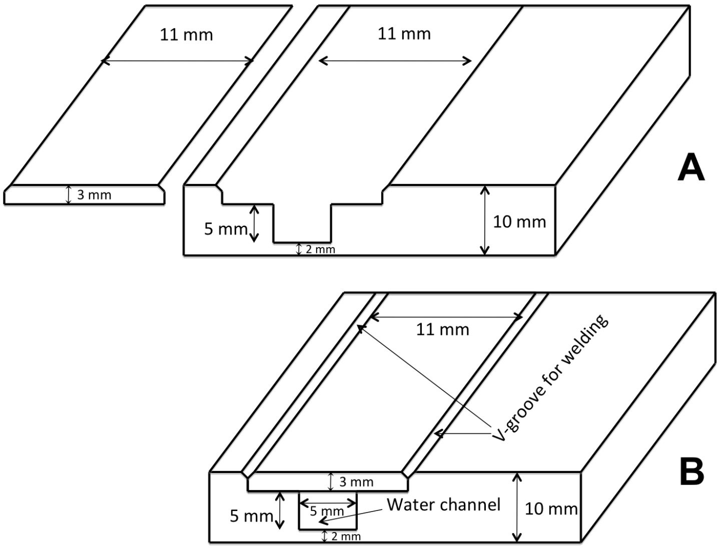

Figure 3.5: Building of 5 mm × 5 mm water channels inside 10 mm thick aluminium plate. Preparation of T-shaped grooves (A), sealed top portion of the T-shaped groove using a 3 mm aluminium sheet (B).

groove is made, realizing a T-shaped groove as shown in Figure 3.5 (A). The top portion (11 mm × 3 mm) of the groove is then sealed by welding a separate aluminium sheet of same dimension using a V-groove junction along the length of the plate as shown in Figure 3.5 (B). This approach generates a 5 mm × 5 mm water channel inside the cooling plate, keeping planarity of the surface of the plate intact.

(II) Technique–II: In the second technique, two identical aluminium plates each of 6 mm thickness are taken, and grooves are made in both in mirror image as shown in Figure 3.6 (A). An aluminium pipe of 6 mm diameter is then press-fitted inside the groove in one of the plates and both plates are then welded together as schematically shown in Figure 3.6 (B) resulting in a 12 mm thick cooling plate with water channels of 6 mm diameter inside.

The inlet and outlet connectors are welded from top side of the plate for connecting water tubes. Water channels are drawn in such a way that they lie precisely below the surface where FEBs are mounted to maximize the heat transfer. Figure 3.7 shows one such cooling plate after the completion of the fabrication.

Cutouts are made on the plate, as shown in Figure 3.7 to allow connection between the detector module and FEBs using flexible cables. Both techniques have their

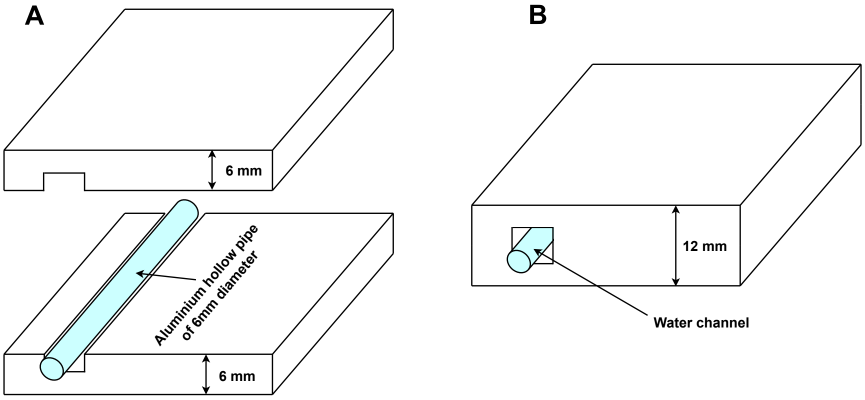

Figure 3.6: Building of water channels of diameter 6 mm inside 12 mm thick aluminium plate. Preparation of grooves on plates in mirror image (A), welding two plates together such that they house water pipes of diameter 6 mm inside (B).

Figure 3.7: Sample cooling plate after fabrication using technique II.

advantages and disadvantages. Technique-I is more efficient in terms of heat transfer as the water channels are in direct contact with the cooling plate, while the Technique-II has the advantage of leak protection as it uses aluminium pipes. Cooling plates are built using both technique-I and technique-II and their performances are studied.

3.5 Control unit

The control unit is one of the essential features of the cooling system because it allows keeping the surface temperature of the plate at a fixed value by regulating the coolant flow rate. The reference temperature is an external parameter and can be set or changed anytime using a computer. It also enables a facility to monitor and record temperature and coolant flow rates.

A microcontroller board ATMEGA328P [88] sits at the heart of the control unit. The board runs at 5 V external power. The controller is interfaced with a computer for monitoring and setting up reference temperature and other parameters. A negative feedback Proportional Integral Derivative (PID) algorithm runs inside the microcontroller. The input to the algorithm is the value of the temperature as measured by the temperature sensor (LM35) mounted on the surface of the cooling plate. The output of the algorithm is an 8-bit Pulse Width Modulation (PWM) signal (ranging from 0 to 255) which is used to regulate the motor speed of the suction pump. The pump is a large load; therefore, the output signal is fed to the base of a power transistor which drives the suction pump. A suitable capacitor and diode in reverse bias are also connected along the terminal of the suction pump to prevent the kickback voltage, which may damage the electronics.

3.6 Test setup and performances for real-size prototypes

To test and validate the concept, design, and integration of the cooling system with the detector modules, studies have been performed on a real-size prototype in the test beam experiment at the CERN SPS beam line facility in November 2016. Two GEM modules of the MuCh detector system were tested at the CERN SPS beamline facility using lead beam on lead target at various beam energies [91–93]. This experiment provided a unique opportunity to test the real size cooling prototype with an actual detector and electronics mounted on it.

Two aluminium cooling plates were built, one following the technique–I while the other using the technique–II as discussed in section 3.4. After preliminary tests for the water leakage, the detector chamber was mounted (see Figure 3.8 (left)) on one side of the cooling plate while FEBs are mounted (see Figure 3.8 (right)) on the other side of the cooling plate using fixing screws.

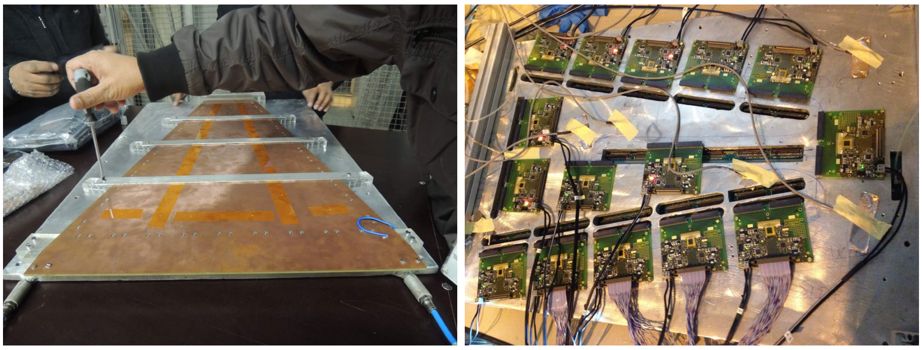

Figure 3.8: The mounting of the detector chamber on one side of the cooling plate (left) and FEBs on the other side of the same cooling plate (right).

A number of LM35 temperature sensors were installed at various locations on the cooling plate toward the FEB side. Figure 3.9 shows the integration of the cooling plate in the test beam experiment from the detector (left) and FEB (right) sides.

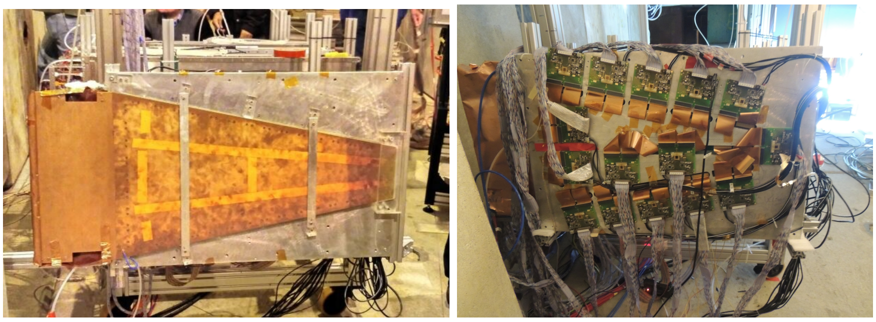

Figure 3.9: Integration of the cooling plate in the test beam experimental setup. Left: Detector side, Right: FEB side.

Two independent water re-circulation systems were made using two submersible suction pumps and water tubes. However, a common chilled water source was used.

Two separate microcontrollers were installed to regulate the speed of two pumps independently interfaced to a shared computer. The microcontrollers were kept outside the radiation zone, as they were not tested for radiation hardness. A reference temperature of 22°C was set for both the systems. The chilled water was kept at a temperature of 12°C.

There was a feedback loop attached in this cooling system where the temperature of the cooling plate was used as an input, and the difference of the cooling temperature from the desired reference temperature was feedback to the motor control unit as shown in figure 3.10. The lower temperature of the chill water help in maintaining the desired temperature even on the lower side of modules for testing purposes. The data-taking continued for more than two weeks during the test beam, and FEBs remained powered-ON during this period. We observed that the cooling system for both modules ran continuously during the entire data-taking period in an automated way without any intervention. The temperatures of the cooling plates were monitored remotely using a monitoring PC, and data points were recorded with a time stamp. The cooling performances for both the modules were quite remarkable, ensuring a stable temperature with ±0.5°C variation on the surface of both plates. Figure 3.10 top panel shows the temperature variation, whereas the bottom panel shows motor speed in PWM units as a function of time for one of the plates with 15 FEBs. It is observed that the temperature remains constant at 22°C (reference temperature) with a variation of ±0.5°C. It is

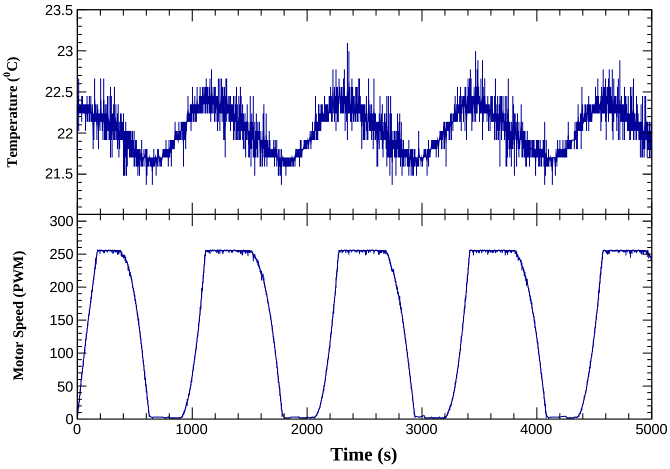

Figure 3.10: Surface temperature of the plate (top) and pump speed (bottom) as a function of time.

also noticed that depending on the temperature of the plate, the pump speed varies with time. The motor speed increases when the plate temperature is higher than the reference temperature, attaining the maximum value. As soon as the plate temperature falls below the reference temperature, the motor speed slowly drops to zero, stopping the coolant flow through the plate. The cycle continues with time, keeping the temperature of the plate constant. The results are shown for a selected period; however the same behavior is obtained for more than two weeks of data taking. Similar performances are also observed for the second plate with 9 FEBs (not shown here).

3.7 Feasibility study of water distribution with multiple prototypes

In the actual experiment, sixteen modules will be connected to each layer of the first tracking station of the MuCh detector system. A test frame made of aluminium extrusion and plywood [94, 95] is developed at Bose Institute, Kolkata, to check how these sixteen modules should be assembled on each layer. Three modules are attached to this frame to test different arrangements or configurations, as shown in Figure 3.12.

In absence of FEBs, the 10 Ω resistors (as shown in figure 3.11a) are used as heating elements to produce uniform heating around 72 W over the whole aluminium module, which is comparable to the actual experimental setup. In each module, eighteen such resistors are embedded. The flat surface of each resistor is attached to the plate using thermal tape to transfer the heat to the modules easily. Heat to be dissipated is generated by passing a current through the resistors, this mechanism is called joule heating. A variable DC power supply of 30 V (Scientific DC power supply PSD3210 3.11b) with a maximum current of 10 A was used to produce the joule heating. Different configurations of resistors are used to select an optimized arrangement that can generate the amount of heat expected to be produced using FEB board in the actual experimental situation. The LM35 temperature sensors 3.11c are used to measure temperature at different positions of the cooling plate. The study was carried out for two different configurations of water distribution which are as follows:

1) ***Flow of water in series through three modules:*** In this configuration, modules

(a) Resistors (b) Voltage Source (c) LM35 temperature sensor

(d) Pneumatic connectors (e) Pneumatic tubes (PPU) (f) Flow Rate Sensor

(g) Water pump

Figure 3.11: Components used in testing process

are connected in series. Water from the source goes to the inlet of the first module, then the outlet of the first module is connected to the inlet of the second module, and so on. Finally, water comes out of the outlet of the third module to the sink. In this case, the water temperature will be different for the inlet of each module due to the absorption of heat in the previous module.

2) ***Flow of water in parallel through three modules:*** In this configuration, water comes directly from the source to the inlet of each module, and it flows back from each outlet to the sink. In this case, the initial temperature of the distilled water will be the same for each module. Push-in pneumatic connectors [96] shown in figure 3.11d and pneumatic polyurethane (PPU) tubes [97] shown in figure 3.11e of 10 mm and 6 mm

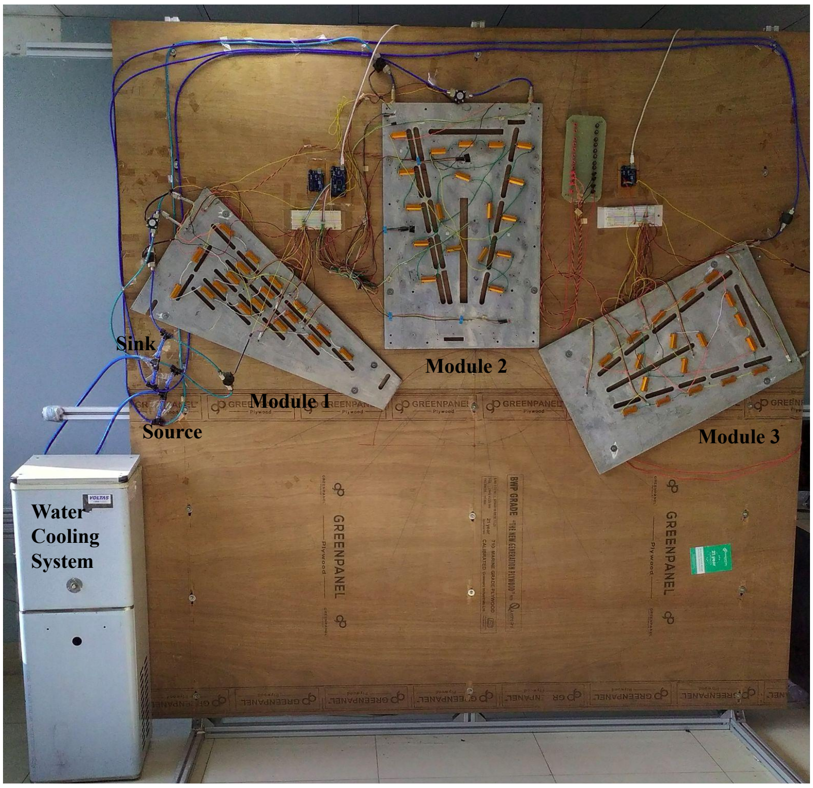

Figure 3.12: Water cooling system and test setup of three modules build at Bose Institute.

.

are used in these configurations.

Six temperature sensors are attached to each module to check the temperature of the module at different points on the surface. Flow rate sensors [98] as shown in figure 3.11f are used at the inlet and outlet of each module. A water cooler 3.12 provides the cool distilled water of temperature between 16°–19°C, a submersible suction pump 3.11g is used to circulate this water through the channels inside the cooling plates. The room temperature was maintained at 25°C. First, the heating starts by input voltage to the heating elements. This is done to check the maximum steady temperature that will be attained by the modules in case of the absence of cooling. The temperature of the modules keeps rising. Within around one hour, modules attain the maximum steady temperature, and that temperature is measured by temperature sensors. Then after some time, the water flow is switched on through the modules, due to which the temperature drops down, and it comes to a stable value. Out of the six temperature sensors, one is selected based on its location near the heating elements on the surface to compare the results. The same procedure is followed for both configurations, and results are shown in Table 3.1 and Table 3.2.

Module	Heat produced(W)	Temp. attained (±1°C) after heating (°C)	after cooling (°C)
1	72.5	30	21
2	78.2	30	24
3	82.2	35	26

Table 3.1: Performance of modules when connected in series.

Module	Heat produced(W)	Temp. attained (±1°C) after heating (°C)	after cooling (°C)
1	72.5	31	21
2	78.2	30	24
3	82.2	35	22

Table 3.2: Performance of modules when connected in parallel.

In both configurations, the minimum temperature attained by the modules shows that the cooling effect was similar for the first two modules, but it is improved for the third module. It is observed that both configurations can keep the temperature of the modules in the required range of 20°–25°C. However, the temperatures of the three modules are more uniform in parallel configurations than in the series configuration. In the actual experiment, the simultaneous start of heating and cooling can avoid an initial rise in temperature.

Chapter 4

Simulation study with CBMROOT

In this chapter, we outline the procedures used during the MuCh detector simulation investigation. In-depth explanations are provided for the MuCh detector's digitization and clustering algorithms. Using a coherent source, primarily from ion-ion collision events, the MuCh detector data rate has been calculated using GEANT3 and GEANT4 transport engines. A Particle Identification Framework (PID) has been utilized to detect hadrons more effectively beyond a specific transverse momentum range.

The simulation study is an essential part of developing an experiment in high-energy physics. For the simulation study of the CBM experiment, CBMROOT [99] framework is specially designed, which relies on the object-oriented C++ ROOT software environment [100]. CBMROOT incorporates a variety of external particle generators and transport systems, like GEANT3 [101], GEANT4 [102], or FLUKA [103] without requiring changes to the user code. It thoroughly explains the geometries and behaviors of the CBM sub-detectors, enabling a realistic analysis of the CBM experiment performance for various physics observables.

To improve the performance and better tune the detectors, we have participated in simulation studies. In one simulation study, we calculate MuCh detector data rate using the coherent source that primarily comes from ion-ion collision events, employing the GEANT3 and GEANT4 transport engines. Estimating the MuCh detector's required minimum data rate handling capacity is helpful for the CBM experimental setup. In another simulation study, we identify the hadrons using a Particle Identification Framework (PID) at a higher transverse momentum range where traditional methods fail. These two studies are discussed in detail in the later part of this chapter. First, we would like to explain the working of the CBMROOT for the MuCh detector.

4.1 CBMROOT simulation chain for MuCh detector

Figure 4.1 shows the block diagram of the steps used in the simulation study of the CBM MuCh detector. The simulation chain is divided into the following parts: (a.) Implementation of geometry and transport, (b.) segmentation of readout pads and digitization, (c.) local hits reconstruction, (d.) track reconstruction and propagation, and (e.) selection of required tracks. Further, each step is discussed in detail.

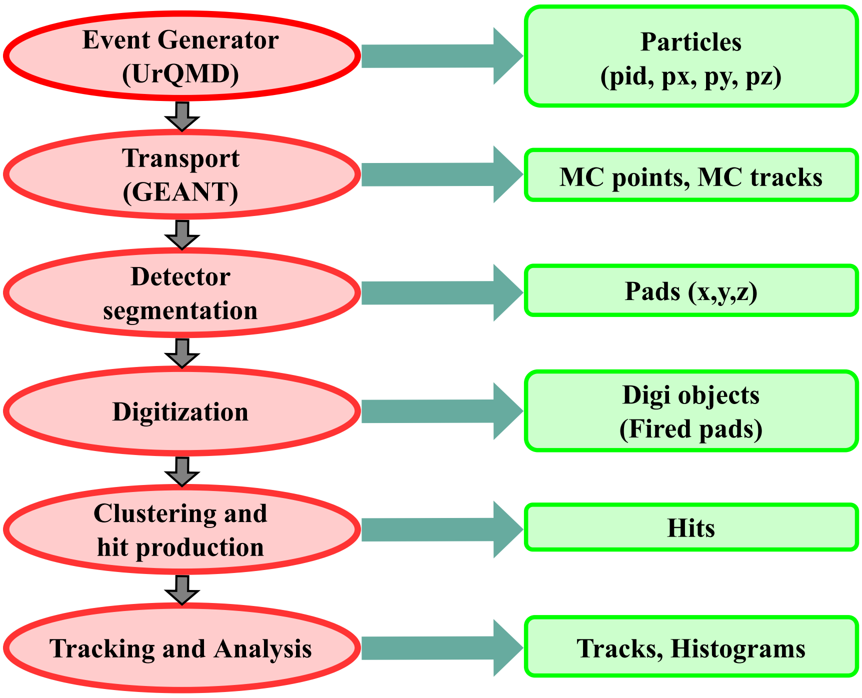

Figure 4.1: Block diagram of the simulation steps used in CBM MuCh detector study.

- **Implementation of geometry and transport:** The CBM MuCh detector identifies the tracks of the particles passing through its detector stations. To do so, first, we need to create the realistic geometry of MuCh detector (for every configuration), which include the absorbers and detector stations, by implementing an actual material budget. It is done by using the GEANT3 transport engine. GEANT3 includes the physics performance of particles as well. Then the particles from the UrQMD event generator are transported through these absorbers and detector layers. The detector contains active and passive volumes. These particles will generate the signals which pass through the active volume. Continuous improvement is made in the geometry part to make it more realistic.

- **Segmentation and digitization:** GEANT3 transport engine provides the position coordinates of the energy deposition by particles in the active volume. The energy deposited and its position coordinates are together called MUCH points. To make the simulated geometry more realistic, the readout plane is segmented into pads for detecting the final detector response. Digitization is the procedure in which MUCH points are distributed into pads depending on the response of the gas detector to the energy deposition inside the chamber. The segmentation of the pads is done by keeping in mind the high hit density and variation of hit density with respect to the radial distance from the beam pipe (density $\propto$ 1/r). In simple digitization, the points falling in a given pad area are combined together to form a digit. In advanced digitization scheme, which is implemented here, MUCH points are treated as primary ionization, multiplication, and signal generation points inside the gas volume.

- **Clustering and local hit finder:** Digits are grouped to make clusters using two different clustering algorithms. One is advanced hit finder algorithm, and another is simple hit finder algorithm. In simple hit finder, one cluster is directly treated as a hit. In advanced hit finder, the clusters are divided into sub-clusters, and each sub-cluster is treated as a hit. The selection of the clustering algorithm depends on particle multiplicity and cluster overlapping. The centroids of multiple sub-clusters or a single main cluster are the assigned location of a MUCH hit for track propagation.

- **Track propagation:** The tracks reconstructed at the STS detector are passed through the MuCh detector propagated using Kalman Filter technique. The MUCH hits found near the propagation points are considered for the propagated tracks. For final consideration, χ^2 of the track fitting, the number of STS and MuCh detector layers connected to the propagated tracks are taken as track validation parameters.

4.2 MuCh detector segmentation, digitization, cluster finding, and hit formation

As we know, MuCh detector is placed just after the dipole magnet, and it will handle a high hit density and large event rates (10 MHz). The segmentation study is necessary for realistic and optimized detector layout production and physics measurements. The muon chamber readout planes are split into several circular sections with pads of the suitable shapes and sizes necessary to obtain the desired pad occupancy to account for the variation of hit density with the distance r from the beam pipe (density declines roughly as 1/r). In addition to the hit occupancy, the maximum pad size is also constrained by spatial resolution. The angular spacing on the transverse plane determines the dimensions of the pads. In the interest of our current system, pads are predicated on a 1° azimuthal angle separation. If necessary, we can divide the pads at greater radii into smaller than 1° intervals as part of future segmentation optimization. The premise that a GEM active gas volume can be divided into the drift and avalanche zones is the basis for the simulation of the GEM detector response (digitization), schematically depicted in Figure 4.2.

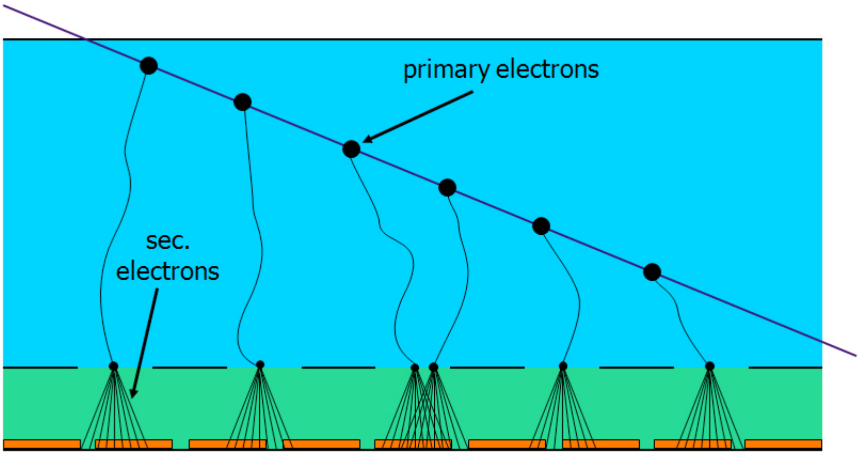

Figure 4.2: Schematic diagram to show signal processing in GEM detector

In reality, triple-layered GEM will be used for MuCh detector. However, the triple-GEM structure is currently not been considered in the simulation. A single GEM layer with a detector gain equal to triple-layered GEM is considered. The following steps are used in digitization:

- The Landau distribution for an argon-based gas mixture, track length in the drift volume, particle type, and energy are used to determine the number of primary electrons generated in the drift volume for each Monte-Carlo point. Throughout the track, primary electrons are produced at random. The HEED [104] package calculates Landau distribution parameter values.

- To estimate the number of secondary electrons that each primary electron contributes to the avalanche zone, exponential gas gain distribution is used with a default mean gas gain of 10^4.

- The spot radius is taken to be 0.6 mm, measured through a beam test, to overlap the secondary electron spots with the pad structure of the module and to determine the charge at every pad. To calculate the arrival time, the Monte-Carlo point time is added to the primary electron drift time.

- To determine the timing responsiveness of the anticipated MUCH readout electronics, a time-dependent sum for charges from all Monte-Carlo points pad-by-pad has been carried out, as well as conversion of the charge-vs-time distribution.

- The following formula converts the signal charge information into Analog-to-Digital Converter (ADC) channels using the threshold charge of the readout:

  $$ADC = \frac{Q_{signal} - Q_{th}}{Q_{max} - Q_{th}} \times nADC \tag{4.1}$$

  where Q_{signal} represents the charge of signal, Q_{max} maximum capacity of a pad to collect charge, Q_{th} is threshold charge, and nADC represents the number of ADC channel (32 channels in this case) for the pads.

- The ADC information and the time stamp of each signal are decoded into 32-bit words and stored in the array of CbmMuchDigi objects along with a 32-bit channel ID for further processing.

Figure 4.3 shows the outcome of such digitization algorithm in terms of reconstructed charge on pads known as digits from the Monte-Carlo track projections. These formed digits are combined together to form clusters, which are further simplified to

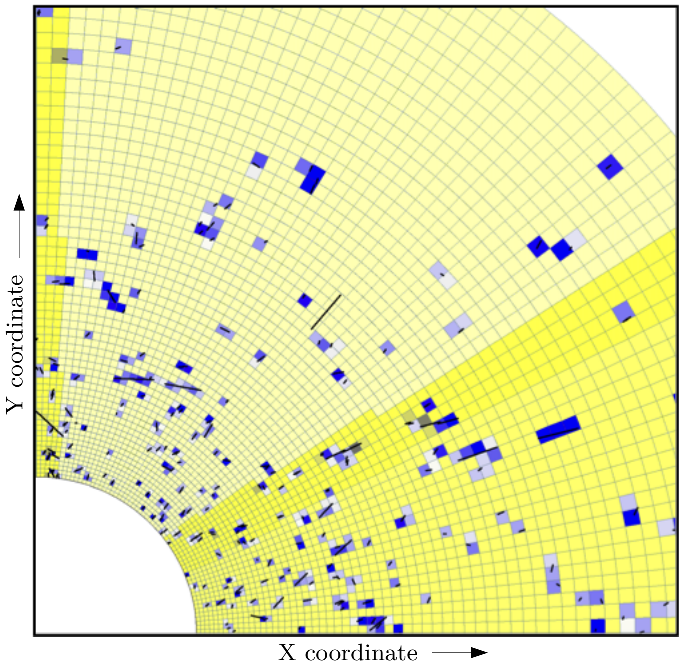

Figure 4.3: Outcome of digitization process for station 1

create hits. For the hit detection and cluster deconvolution, the following approaches have been used:

- **One hit per pad:** The algorithm becomes simple when a hit is generated for each fired pad. The hit positions match the pad centers, and the hit uncertainties are calculated by dividing the pad lengths by $\sqrt{12}$. This algorithm's main benefits are its ease of implementation and minimal CPU usage. The biggest drawback is that there are too many hits produced, and many of them seem to be far from the actual track places. Increased combinatorial backdrop and inefficiency at the track-finding level are also caused by more additional hits.

- **One hit per cluster:** When one hit per cluster is taken, Center-of-gravity averaging using weights corresponding to charges induced on pads yields the hit coordinates. Additionally, this algorithm is quick and easy to use. This approach enables a more exact definition of track location while dealing with small pads than in the prior scenario. The reconstructed hit positions and actual track coordinates may diverge too much in the event of big clusters due to this technique.

- **Search for local maxima:** Local maxima is searched for each cluster. Centers of pads are given hit locations that correlate to local maxima. One hit per cluster approach is used to more accurately calculate the hit coordinates for small clusters when the cluster dimensions are less than (2×2) pads. However, in the event of long clusters (often generated by a single, extremely angled low-energy electron), local maxima may result from unpredictable charge fluctuations on pads. Therefore, looking for local maxima may produce bogus hits that don't match actual tracks. Additionally, one should be aware that this technique might not be able to resolve all tracks.

The MUCH simulations employ the search for local maxima as their default algorithm. The established cluster and hit-finding methods can be applied to the reconstruction of actual data and the simulated one.

Now we come to our contribution to the simulation studies for the CBM experiment. As discussed earlier as well, the CBM detector will have an interaction rate of 10^7 Hz, which is very high to handle by any detector. As the MuCh detector is one of the initial detectors of the CBM experiment, the first few layers of MuCh detector will face a very high data rate. So, it is crucial to study the data rate handling capability of the MuCh detector.

4.3 Data rate estimation for MuCh detector

In CBMROOT framework, particles generated via an event generator like UrQMD are made to pass through the absorbers and detector layers of MuCh detector using GEANT3 transport engine. But GEANT3 underestimates particle rate, particularly those produced due to nuclear interaction. So we use GEANT4 instead of GEANT3 because GEANT4 includes some additional process that represents the interaction more reasonably compared to GEANT3. These phenomena inside the most recent version of GEANT4 provide the good agreement of energy response and resolution of pions and protons.

Two types of sources contribute to the data rate- one is the coherent source, and another is the incoherent source. The coherent source contains mainly the data from ion-ion collision events, named target data rate. We generate coherent sources by using the UrQMD event generator. The incoherent source contains the data from the noise in the electronics, which is called “Thermal Background” and depends on the system’s temperature. Another contributor to the incoherent source is the background data created by the beam passing through the setup. Most of these backgrounds are delta electrons produced in the target, but they can also be produced in, e.g., the beam pipe if it is not well designed. Here we are considering only event-coherent sources. In this study, we estimate the MuCh data rate by using event coherent sources from GEANT3 and GEANT4. First, to see the difference in the effect of GEANT3 and GEANT4 transport models, we analyze 10^5 minimum bias Au-Au events from UrQMD at beam energy 12A GeV. The produced particles are passed through the SIS-100 muon setup, which includes five hadron absorbers and four tracking stations. Each station consists of three GEM layers.

We compare point density per event for each station of MuCh for GEANT3 and GEANT4. It is observed that the contribution of secondary particles has been increased with GEANT4 compared to GEANT3. As is expected, there is hardly any change in the contribution of primary particles. It can be easily seen from Table 4.1. Table 4.1 represents the rough estimation of the average number of particles per event from a single sample of 10^5 events. Standard errors are not mentioned in the table.

	Average number of particles/event		
	All particles	Primary	Secondary
Station 1 (with GEANT3)	225.23	11.19	214.03
Station 1 (with GEANT4)	276.90	10.96	265.94
Station 2 (with GEANT3)	43.62	2.88	40.73
Station 2 (with GEANT4)	77.67	2.70	74.96
Station 3 (with GEANT3)	12.85	0.79	12.06
Station 3 (with GEANT4)	28.45	0.66	27.78
Station 4 (with GEANT3)	3.45	0.13	3.31
Station 4 (with GEANT4)	8.36	0.08	8.27

Table 4.1: Average number of primary and secondary particle production per event for 12A GeV minimum bias Au-Au collisions using GEANT3 and GEANT4 transport models.

Next, we study the occupancy of radial segments of each detector, where occupancy is the fraction of fired pads per event. For this purpose, the detector planes are segmented radially into square pads of 1° azimuthal angle. Radial distribution of occupancy for each station using GEANT3 and GEANT4 are shown in Figure 4.4.

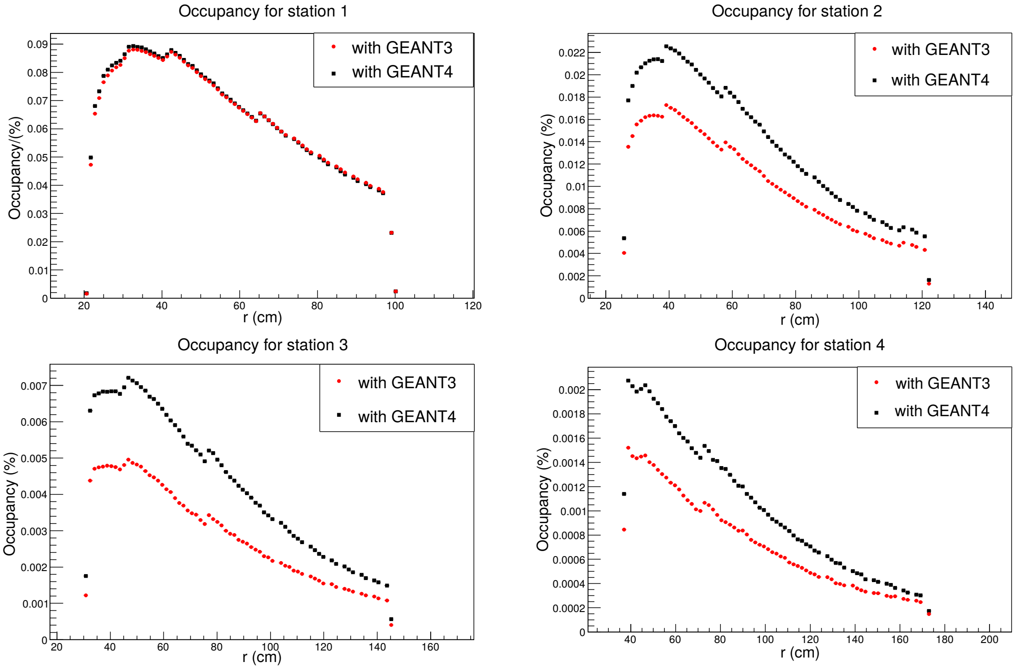

Figure 4.4: Occupancy for different MuCh stations for 12A GeV minimum bias Au-Au collision using GEANT3 and GEANT4 transport models.

For the first station, there is hardly any change in occupancy. But for the second station, due to a quite large increment in secondary particles with GEANT4, a significant increment in occupancy is observed. The maximum pad hit rate is estimated by multiplying the maximum occupancy for each station with peak collision rate (10 MHz). The estimated pad hit rate for each station using GEANT3 and GEANT4 is shown in Table 4.2.

There will be a direct effect of beam energy on the occupancy and the estimated data rate. In Figure 4.5, it is shown that if we take beam energy 35A GeV, the occupancy will reach up to twice as large compared to beam energy 12A GeV. So it is suggested to use detector layers that can handle such a high data rate according to the required beam energy.

	Maximum pad hit rate
Station 1 (with GEANT3)	97 kHz
Station 1 (with GEANT4)	99 kHz
Station 2 (with GEANT3)	19.2 kHz
Station 2 (with GEANT4)	25 kHz
Station 3 (with GEANT3)	5.5 kHz
Station 3 (with GEANT4)	8 kHz
Station 4 (with GEANT3)	1.7 kHz
Station 4 (with GEANT4)	2.3 kHz

Table 4.2: Maximum foreseen pad hit rate at collision rate of 10 MHz due to event coherent background source, for 12A GeV minimum bias Au-Au collision for each station using GEANT3 and GEANT4 transport models.

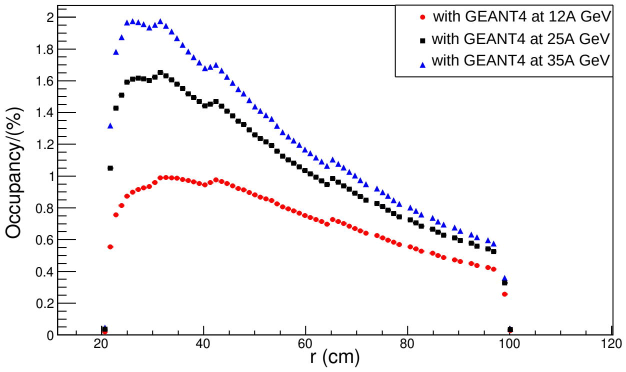

Figure 4.5: Comparison of occupancy for 1st station at different beam energies.

4.4 Identification of Hadrons using PID framework

The MuCh detector in CBM experiment can be replaced with RICH detector for electron identification. It is critical to measure leptons and hadrons simultaneously to obtain a complete picture of the reaction [105]. This could be accomplished with the RICH detector, which has a low material budget and has little influence on hadron trajectories on their way to the Time-of-Flight (TOF) detector. In this part of the study, Particle Identification (PID) Framework [106] is used to identify hadrons. This framework is based on graphical cuts and fitting parameters to predict a particle track of a particular hadron species. In this study, high accuracy is achieved by calibrating the framework.

One million events of 12A GeV Au-Au minimum biased collision are taken, which are generated using Dubna Cascade—Statistical Multifragmentation Model (DCM-SMM) event generator [107] with transport engine GEANT4. The SIS100 electron setup of the CBM experiment is used for this study.

q×p vs. m^2 distributions are plotted for pure samples of protons, kaons, and pions and for all particles. Here q and p represent the charge and momentum of each track, respectively and m represents the mass calculated from the Time of Flight (TOF) detector. Projections of q×p on m^2 are taken into slices and fitted with proper distribution functions (Gaussian for signal, second-order polynomial for background). Stabilized fitting parameters for each particle are used to calculate the Bayesian probability (purity) by using the formula:

$$Purity_i = \frac{P_i}{(\Sigma P_i + P_{bg})} \tag{4.2}$$

P_i and P_{bg} are the probabilities of a track being associated with a hadron species and a background particle, respectively. Here:

$$P_i = A_i e^{-\frac{(\mu_i - m^2)^2}{2\sigma_i^2}} \tag{4.3}$$

and

$$P_{bg} = a(m^2)^2 + bm^2 + c\ ,\ a \neq 0 \tag{4.4}$$

A, μ, σ are the fitting parameters for the signal, and a, b, and c are the fitting parameters for the background. This Bayesian probability or purity is further used to identify hadrons (proton, pion, kaon, etc.).

As we are interested in hadrons produced in the early stages, only primary particles are considered here by using their PDG values. Figure 4.6(a) shows the hadrons based on their PDG values, and Figure 4.6(b) shows the particles detected as hadrons using purity greater than or equal to 90%.

The definition of recall and precision for each hadron species are as follows:

$$Recall = \frac{True\ particles\ using\ PID}{Total\ particles\ using\ PDG}\% \tag{4.5}$$

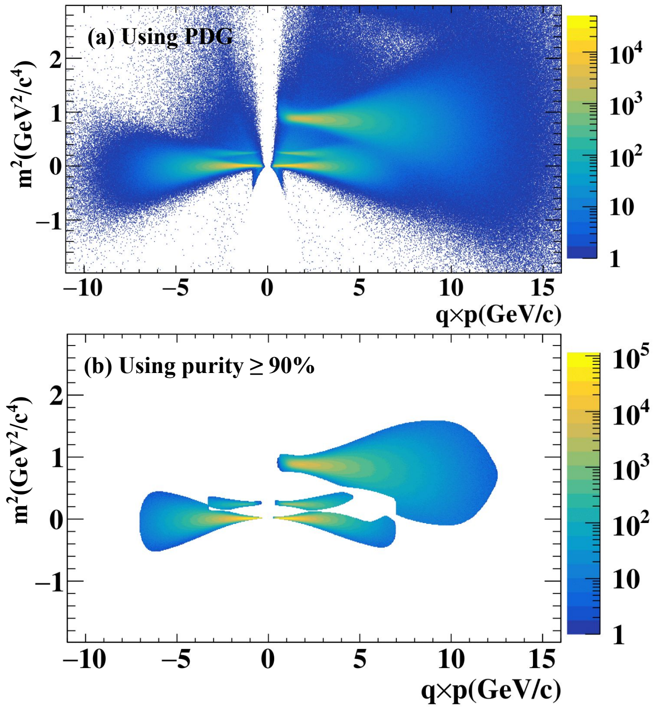

Figure 4.6: m^2 vs. q×p distribution for (a) hadrons detected using PDG, (b) particles detected as hadrons using purity $\geq$ 90%.

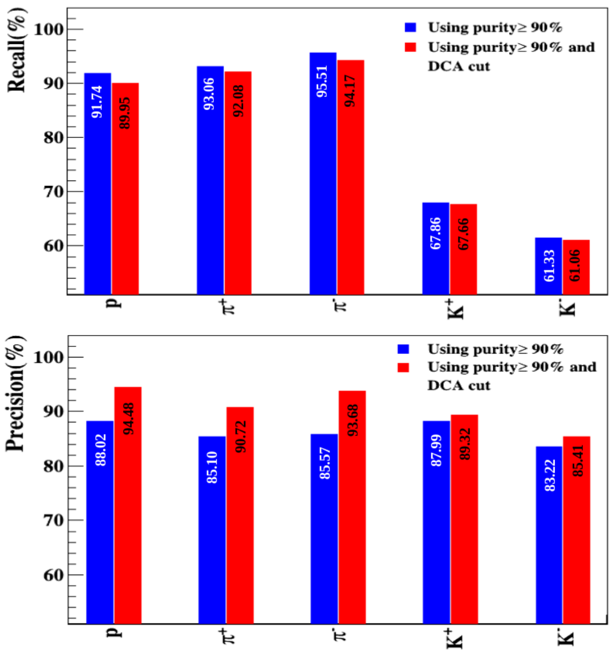

Figure 4.7: Comparison of recall and precision for each hadron species before and after using DCA cut.

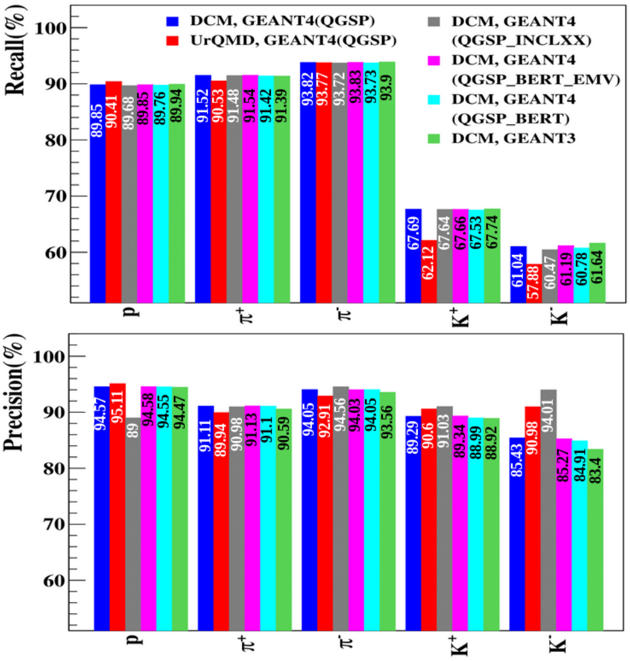

Figure 4.8: Comparison of recall and precision for each hadron species for different event generators and GEANT transport engine setups using purity $\geq 90\%$ and DCA.

$$Precision = \frac{True\ particles\ using\ PID}{Detected\ as\ particle\ using\ PID}\% \tag{4.6}$$

Further, we use the distance of closest approach (DCA) to minimize the false particle detection using cuts $DCA_{proton} \leq$ 0.36, $DCA_{\pi^+} \leq$ 0.58, $DCA_{\pi^-} \leq$ 0.52, $DCA_{K^+} \leq$ 0.84, and $DCA_{K^-} \leq$ 0.75. Figure 4.7 compares recall and precision for each hadron species before and after using DCA cut. In the case of recall, we are compromising some true particles by employing DCA cut. However, there is a large gain in precision for all hadron species.

PID framework can predict protons and pions more accurately compared to kaons. It is because of the low statistics of kaons compared to pions and due to the merging of kaons with pions.

Using the same predicted purity values for the UrQMD event generator and for different GEANT3 and GEANT4 transport engine setups, we are able to detect hadrons to a similar extent with a negligible difference, which are compared in Figure 4.8.

Chapter 5

Model-dependent study of anisotropic flow and particle production in low-energy heavy-ion collisions

In this chapter, we briefly discuss our phenomenological study related to the effect of equations of state, particlization scenarios, and beam energy on anisotropic flow, particle production, and other variables using the UrQMD model.

5.1 Introduction

In recent times, hybrid models have been found beneficial for describing the evolution of strongly interacting matter in heavy-ion collisions. In the hybrid models, the transport approach to explain the non-equilibrium dynamics is connected with a hydrodynamical description to describe the expansion of the locally thermalized fireball. Such a combination of approaches can be advantageous in investigating various observables to extract QCD medium properties. To contribute to this region, we study different variables like various flow coefficients of the anisotropic momentum distribution of final state particles, different features of particle production such as particle ratios and net-proton rapidity distribution in mid-central ($b =$ 5–9 fm) Au + Au collisions in the beam energy range $\mathrm{E_{Lab}} = 1A - 158A$ GeV. For the initial study, different variants of the Ultra-relativistic Quantum Molecular Dynamics (UrQMD) model, namely the pure transport (cascade) mode and the hybrid mode, are employed. In the hybrid UrQMD model, the ideal hydrodynamical evolution is integrated with the pure transport calculation for the description of the evolution of the fireball. We opt for the different available equations of state (EoS) replicating the hadronic as well as partonic degrees of freedom together with possible phase transitions, viz. hadron gas, chiral + deconfinement EoS, and Bag Model EoS, to investigate their effect on the properties of the final state particles. In addition to this, the effect of various particlization models available in the hybrid mode of the UrQMD event generator is also discussed. Particlization models are used to switch fluid dynamic description to the transport description using various hypersurface criteria. We also attempt to gain insights into the dynamics of the medium by studying different features of particle production, such as particle ratios and net-proton rapidity distribution.

5.2 UrQMD Model

The purpose of the UrQMD model [6, 51, 108] is to simulate high-energy nucleus-nucleus collisions. The initialization of the target and projectile nuclei in coordinate and momentum space is done with the help of the Woods-Saxon profile and the Fermi gas model, respectively. Together with the various experimental inputs such as cross-sections, and decay widths, the collisions in the model are narrated in terms of interactions among resonances, hadrons, and their excited states at low energies and in terms of excitation of color strings with their subsequent fragmentation into hadrons at higher energies [51]. The propagation of hadrons occurs on straight-line trajectories amid subsequent collisions.

In the hybrid version of the UrQMD, the ideal (3+1)d relativistic fluid dynamical evolution using SHASTA [109, 110] algorithm is combined with a pure transport approach for better modeling of the intermediate hot and dense stages of the collision. Calculating the initial state of the hydrodynamical evolution is crucial to account for the non-equilibrium nature of the early stage; moreover, this also incorporates event-by-event fluctuations of the initial states. The hydrodynamical evolution commenced upon crossing the two Lorentz-contracted nuclei [108]. As soon as the two Lorentz-contracted nuclei cross each other, which corresponds to the starting time that ensures all baryon scatterings and energy deposition have taken place, the hydrodynamics is switched on. The starting time t_{start} for hydrodynamic evolution is of the order of a few fm/c (see figure 8 of [108]) and is calculated through equation (5.1):

$$t_{start} = \frac{2R}{\gamma\beta} = \frac{2R}{\sqrt{\gamma^2 - 1}} = 2R\sqrt{\frac{2m_N}{E_{lab}}} \tag{5.1}$$

where R represents the radius of nucleus, β represents the velocity of nuclei in center of mass frame, m_N represents the nucleon mass, and E_{lab} corresponds to the kinetic beam energy. This time acts as a lower bound for the thermalization time. Right after this, the spectators are sent into the cascade, and participant particles, which are "point-like" in nature, are mapped onto a hydrodynamical grid.

Next stage is the hydrodynamical evolution, where the equation-of-state (EoS) is an essential input. There are three EoS available in the public version of the UrQMD hybrid model. The first one is the hadron gas (HG) EoS [111] which is non-interacting gas of hadrons expressed by grand canonical ensemble and does not have any phase transition. As the underlying degrees of freedom are the same, the hydrodynamical and pure transport approaches can be compared on equal footing. The next EoS is chiral + deconfinement EoS [112] which incorporates both chiral and deconfinement phase transitions. The latter is of cross-over type in nature for all finite net baryon densities. In addition to this, this EoS has partonic degrees of freedom. Moreover, deconfinement transition occurs through quarks and Polyakov potential, whereas hadronic interaction administers chiral phase transition. Note that the partonic degrees of freedom only show up when the temperature is high enough. It has been seen that this EoS agrees well with the lattice QCD simulations at vanishing baryon chemical potential. The final available EoS is the bag model (BG) [110] which is a combination of the standard MIT bag model and an improved version of the $\sigma - \omega$ model. The former is utilized for the QGP phase, whereas the latter is employed in case of the hadronic phase. This EoS is available with an inbuilt first-order phase transition, during which Gibbs' conditions are used to match both hadronic and partonic phases for equilibrium.

As time evolves, the system starts to become diluted due to expansion, and fluid dynamical description would no longer be applicable. Therefore, the fluid description can be changed to particle description using Cooper-Frye formalism, the procedure is known as "Particlization". One of the crucial steps here is the determination of transition hypersurface. In the hybrid UrQMD model, depending on the type of hypersurface and switching criteria, three different particlization scenarios are available for fluid to particle transition. The default scenario is known as the gradual particlization scenario (GF), in which the fluid slices of thickness 0.2 fm undergo particlization when the energy density in all cells of that slice falls below five times the ground state energy density ϵ_0. So, the particlization is performed slice by slice. The other possible scenario is isochronous particlization (ICF), where the particlization takes place at the same time as soon as the energy density in all cells falls below the critical value ($5\epsilon_0$). In these two cases, the hypersurface is isochronous in nature. In the latter case, it is possible that the parts of the system may have become dilute as the transition can only be done once all cells have energy density below a specific critical value. Therefore, the application of fluid dynamics would be questionable in this case. The last one is the iso-energy density particlization scenario (IEF), where the iso-energy density hypersurface is constructed numerically with the help of Cornelius routine [113]. After that, the hydrodynamical fields are mapped to particles on this hypersurface using Cooper-Frye formalism once the energy density in all cells reaches below the critical value. As discussed in Ref. [113], this scenario is suitable for dealing with event-by-event heavy-ion collisions analysis. The sampling algorithm described there is very flexible in event-by-event calculations where the initial states of hydrodynamics change widely.

5.3 Dependence on beam energy and nuclear equation of state

In an initial study, we make some efforts to address the nuclear equations of state dependence of the anisotropic flow coefficients and particle production in noncentral (b = 5–9 fm) Au–Au collisions in wide ranges of the beam energies, $\mathrm{E}_{\mathrm{Lab}} = 1A - 158A$ GeV which span over existing GSI-SIS energy of HADES experiment up to top SPS energy. It is found that the corresponding $< N_{\mathrm{part}} >$ values in the chosen impact parameter range b = 5–9 fm, covers approximately $10 - 40\%$ centrality class [114]. For our study, we employ the publicly available version 3.4 of the UrQMD model with different configurations of a hybrid model for the intermediate hydrodynamical stage viz., Hadron Gas (HG), Chiral + deconfinement EoS, and Bag Model EoS along with pure transport approach. The last two hybrid versions mimic the partonic degrees of freedom and phase transition in the medium; however, the first one includes hadronic degrees of freedom only. The reaction plane angle (Ψ) is taken to be zero within this model. It is important to note that the present study is not a pioneering attempt to apply hybrid UrQMD model to study collective flow excitation at these beam energies. In [115], the authors have calculated the transverse momentum and rapidity dependence of v_1 and v_2 at 40A and 160A GeV in Pb + Pb collisions using standard UrQMD model at various centralities which showed disagreement with experimental measurements by NA49 collaboration. In addition, v_1 and v_2 were also studied as a function of beam energy in the range of $\mathrm{E_{Lab}} = 90\mathrm{A}$ MeV to $\mathrm{E_{cm}} = 200\mathrm{A}$ GeV and also, showed disagreement with the available data. In Ref [116], the excitation function of v_2 was examined in the range of GSI-SIS to CERN-SPS energies using UrQMD with HG EoS within hybrid approach and other harmonics such as, v_2 and v_3 are studied with Chiral EoS in Au–Au systems between $\sqrt{s_{NN}} =$ 5–200 GeV [50]. The collision energy dependence of v_1 is tested using the hybrid model for nuclear reactions between $\sqrt{s_{NN}} = 3-20$ GeV [117]. In a work [118], study on nuclear equations of state dependence of anisotropic flow was performed using hybrid UrQMD model within 6A–25A GeV with HG and chiral EoS. All these results seem to suggest the quantitative applicability of this model to real scenario has some limitations. However, in this part, we qualitatively aim to understand the effect of various nuclear equations of state and various particlization scenarios using multiple particlization models on the flow harmonics and hence gain some insights about the dynamics leading to their development at various beam energies ranging from 1A–158A GeV.

Besides anisotropic flow, we also attempt to study the EoS dependence of particle production in noncentral collisions. The particle ratios of various species are examined for this purpose. We also look at the net-proton rapidity distributions. The structure of the net-proton rapidity spectra at the mid rapidity is expected to be sensitive to the underlying EoS of the nuclear fireball as well as to the various particlization scenarios. In central collisions, adequate studies have been performed in this direction. In Refs. [141–145], the authors have quantified the structure of net-proton rapidity distribution at mid rapidity in central collisions, in terms of reduced curvature. It was studied as a function of beam energy and compared with predictions incorporating various possible scenarios of fireball expansion. In the present study, we extend these studies to the mid-central collisions.

5.3.1 Results and Discussion

In this section, we present the results of our investigations on various anisotropic flow coefficients at different beam energies for charged and identified hadrons. All three EoS mentioned above are employed for this purpose. Then we move on to investigate the sensitivity of underlying EoS to the different particle production mechanisms such as strange to non-strange ratio, baryon to meson ratio, and so on. Finally, we also look at the net-proton rapidity spectra for different EoS to look for possible insights into the longitudinal dynamics of the medium.

Anisotropic flow coefficients

Among various harmonic coefficients, v_1 is believed to hold sensitivity against the longitudinal dynamics of the QCD medium. Therefore, we start by estimating the v_1 of charged hadrons as a function of rapidity at different beam energies and for pure transport and hybrid versions of the UrQMD model. The results are shown in Figure 5.1. In presence of hydrodynamic expansion, the slope at mid-rapidity remains positive at all investigated energies. For a pure transport approach, the slope initially remains positive and eventually becomes negative.

Directed flow of pions and protons for $p_{\mathrm{T}} < 2$ GeV/c at 40A and 158A GeV are compared with the existing measurement by NA49 experiment [121] at SPS in 10–40$\%$ central Au + Au collisions as shown in Figure 5.2. Hybrid mode fails to explain the v_1 except for pions at 40A GeV. The pure transport approach is seen to do a better job of explaining the proton v_1 reasonably well at both energies at midrapidity, an observation in line with previous studies [115, 147].

Slopes of directed flow of charged hadrons, pions, protons and net-protons as a function of beam energy are quantified in Figure 5.3. The slope is obtained by fitting differential directed flow ($v_1(y)$) using first order polynomial at mid-rapidity. Similar values of slopes are noticed in all three cases of hydro mode up to 10A GeV for all

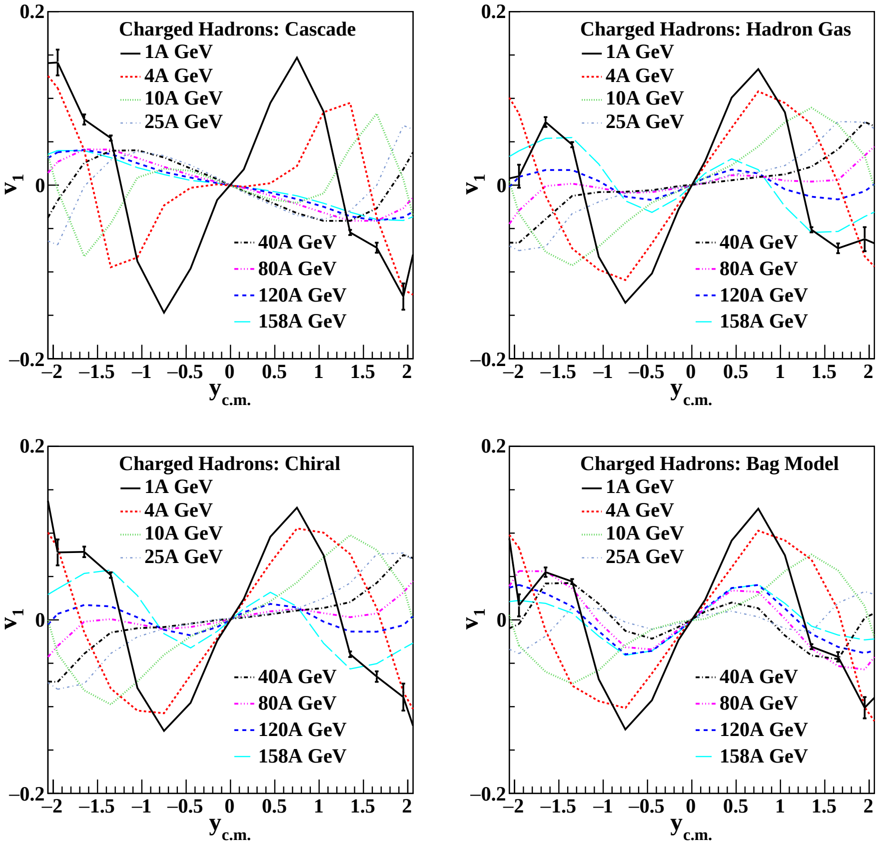

Figure 5.1: Directed flow of charged hadrons as a function of rapidity at different beam energies for different configurations of UrQMD for noncentral (b = 5-9 fm corresponds to approximately 10-40% central) Au-Au collisions.

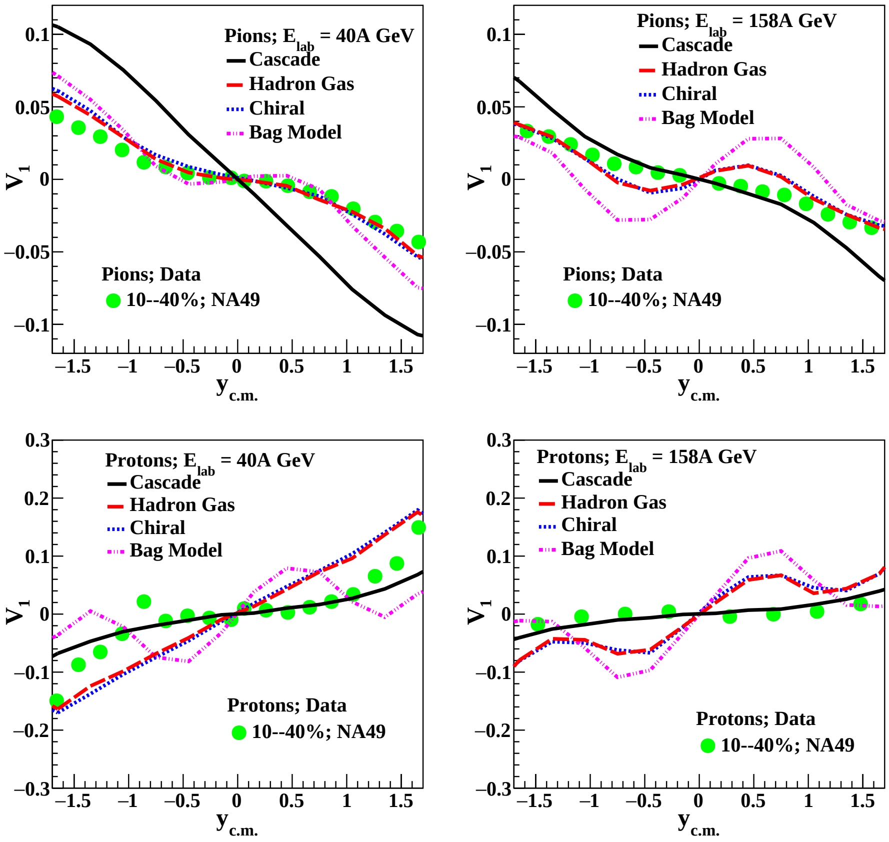

Figure 5.2: Comparison of directed flow of pions and protons as a function of rapidity for different configurations of UrQMD with measured directed flow for $p_{\mathrm{T}} < 2$ GeV/c for noncentral (b = 5-9 fm corresponds to approximately 10-40% central) Au-Au collisions with NA49 experimental measurements [121] at 40A and 158A GeV in Pb-Pb collisions.

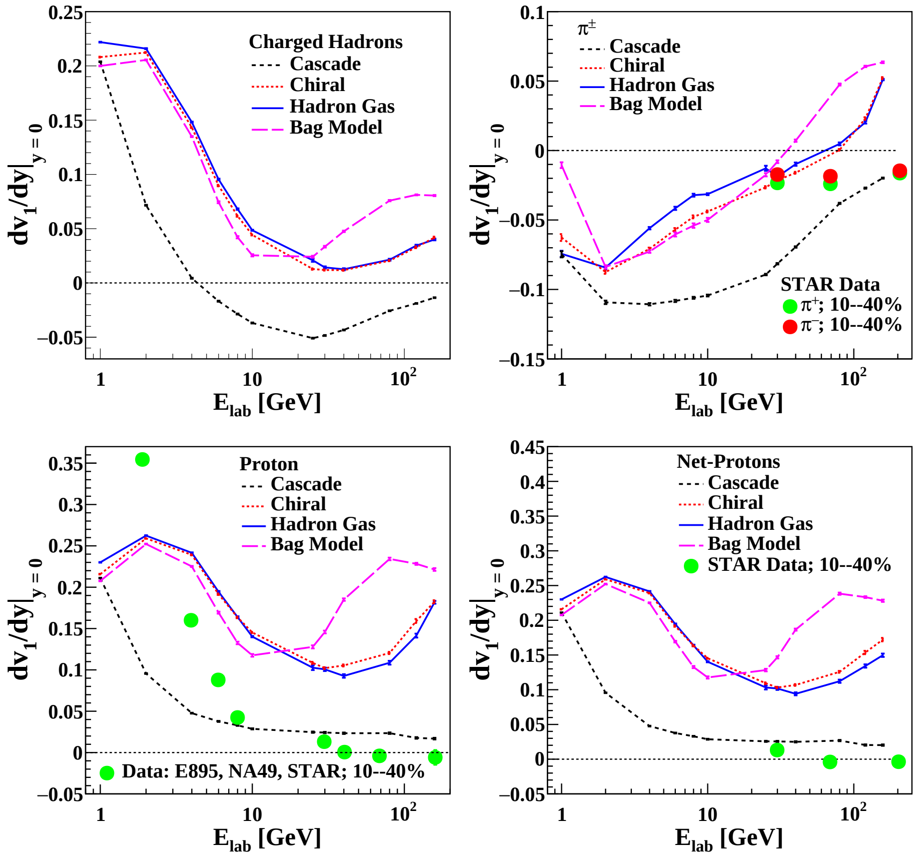

Figure 5.3: Slope of the directed flow of charged hadrons, pions, protons and net-protons as a function of beam energy at midrapidity for different configurations of UrQMD for noncentral (b = 5-9 fm corresponds to approximately 10-40% central) Au-Au collisions with E895 [122] and STAR [123] experimental measurements in Au-Au collisions and with NA49 [121] experimental measurements in Pb-Pb collisions.

species. The slope using cascade mode is smaller compared to hydro mode. For pions, the slope obtained in cascade model always remain negative at all investigated energies and show transition from negative to positive value between 30A to 80A GeV once hydrodynamic expansion is switched on. The slope does not show any sensitivity to underlying dofs brought by HG and chiral EoS in charged hadrons case which was also observed in our previous study between beam energies 6A–25A GeV [118]. Moreover, we tend to see a slight hint of sensitivity in protons and net-protons case beyond 25A GeV, however, we cannot make any strong claim at the moment.

In all three EoS cases of hybrid mode, the minimum in slope is observed between 10A–80A GeV. However, in case of Bag Model EoS, the minimum occurs near 10A–25A GeV while for case of other two EoS, the minimum is slightly shifted to higher energy and lies between 25A–80A GeV. This shift in minimum leads to a splitting of

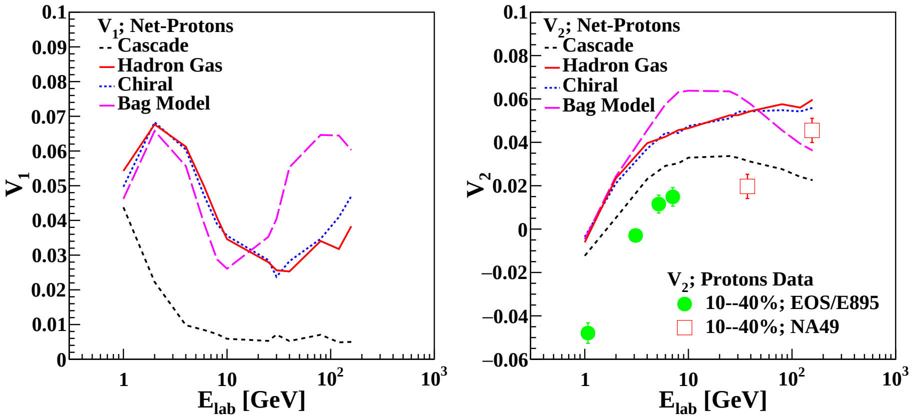

Figure 5.4: p_{T} integrated directed (v_1) (left) and elliptic (v_2) (right) flow of net-protons as a function of beam energy at midrapidity ($0 < y_{c.m.} < 0.5$) for different configurations of UrQMD for noncentral (b = 5-9 fm corresponds to approximately 10-40% central) Au-Au collisions. In the right plot, v_2 of protons for $p_{\mathrm{T}} < 2$ GeV/c is compared with available E895 and NA49 experimental measurements [55, 121] in investigated beam energy range in Au-Au and Pb-Pb collisions, respectively.

slope parameters of $v_1(y)$ between Bag Model and other two EoS which lie around 25–30A GeV. A strong increase of slope in case of Bag Model is observed which could possibly be a result of the in built first order phase transition and perhaps, hint towards the possible onset of deconfinement. In the past, similar interesting feature around similar beam energy has been observed for strange to non-strange ratio [138]. Moreover, the slope of directed flow of protons is compared with the available experimental measurements of E895 [122], NA49 [121] and STAR [123] collaborations as depicted in Figure 5.3. It reveals that the results with hybrid mode overestimate the data beyond 2A GeV. Moreover, the slope of v_1 of pions and net-protons is compared with STAR experiment measurements and it is observed that the inclusion of hydrodynamic expansion overestimates the measurements. According to the fluid dynamical calculations, the slope of v_1 of the baryons is expected to change sign attributed to softening of EoS in the presence of first order phase transition. This was tested with various freeze-out scenarios using hydrodynamical simulations in Ref. [117]. On the other hand, the results with cascade mode underestimate the measurements below 6A GeV and thereafter, show similar trend with slight overestimation above 30A GeV.

Moving forward, we attempt to look at the net-protons for $p_{\mathrm{T}} < 2$ GeV/c in more detail by inspecting their p_{T}-integrated directed and elliptic flow at midrapidity (-0.5 <

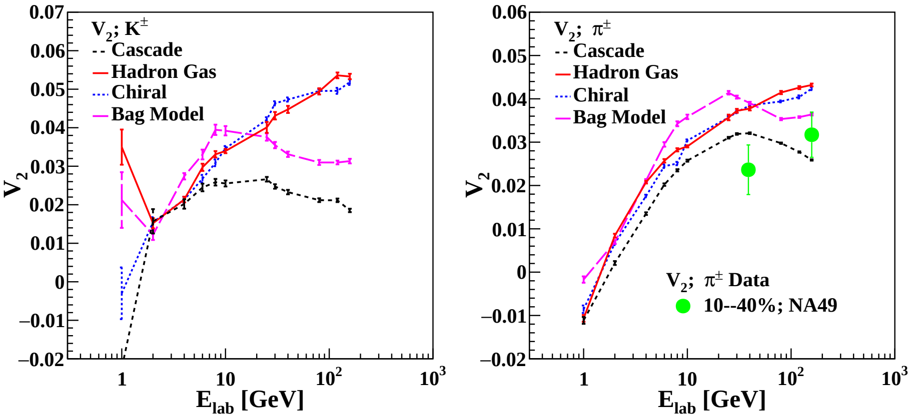

Figure 5.5: p_{T} integrated elliptic flow of kaons and pions as a function of beam energy at midrapidity (-0.5 $< y_{c.m.} <$ 0.5) for different configurations of UrQMD for noncentral (b = 5-9 fm corresponds to approximately 10-40% central) Au-Au collisions. In the right plot, v_2 of pions for $p_{\mathrm{T}} <$ 2 GeV/c is compared with available NA49 experimental measurements [121] in investigated beam energy range in Pb-Pb collisions.

$y_{c.m.} <$ 0.5) as a function of beam energies as shown in Figure 5.4. In the left plot, we observe alike trend for v_1 as its slope in all four cases studied here. Moreover, feature of splitting at 20–30A GeV in presence of hydrodynamical evolution is also observed. While in case of v_2 in the right plot, we witness a similar splitting between Bag Model EoS and other two EoS. Furthermore, at beam energies around 10–25A GeV a broad peak for v_2 in case of Bag Model can be seen and for v_1 as well as its slope, it is appeared as a dip at similar beam energies. We repeat this exercise for v_2 of kaons and pions for $p_{\mathrm{T}} <$ 2 GeV/c as shown in Figure 5.5 and here also, kaons and pions confirm the EoS dependent splitting in hydro case, however, the splitting is not prominent in case of pions. Furthermore, the v_2 of pions and net-protons is also compared with the experimental measurements from E895 and NA49 collaborations [55, 121] and we saw overestimation of the data by hybrid mode here as well.

We now move our focus to look at the higher order flow harmonic coefficient v_4 which has been argued to be generated under the influence of 4^{th} order moment of fluid flow and the intrinsic elliptic flow, v_2 [125–127]. Under the assumption of ideal fluid dynamics and without any fluctuations, v_2 and v_4 are related to each other as, v_4 = 0.5$(v_2)^2$. So one can expect to acquire some information about the transport properties of nuclear fireball by estimating the ratio $v_4/(v_2)^2$. This ratio has been studied in [118] within beam energy range 6A–25A GeV for different equations of state ex-

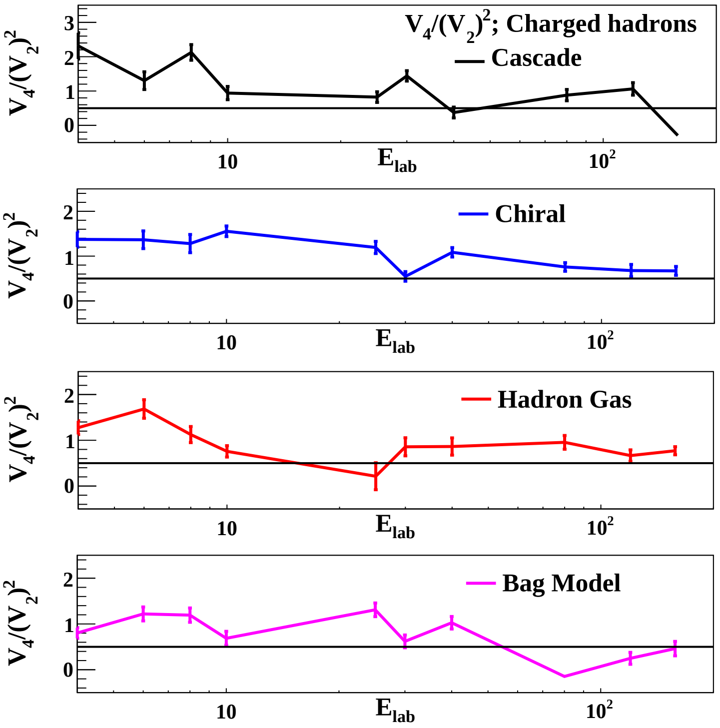

Figure 5.6: $V_4/(V_2)^2$ of charged hadrons as a function of beam energy at midrapidity (-0.5 $< y_{c.m.} <$ 0.5) for different configurations of UrQMD for noncentral (b = 5-9 fm corresponds to approximately 10-40% central) Au-Au collisions. The horizontal line at 0.5 denote the ideal fluid dynamic limit.

cept Bag model. Prior to this, some phenomenological study has been performed for this observable. In particular, the observations using Parton-Hadron-String Dynamics (PHSD) model [128] at different beam energies with Au–Au collisions, have shown the ratio $v_4/(v_2)^2 \approx 2$. Moreover, the authors at Ref. [129] have attempted to investigate the enhancement of v_4 in low energy nuclear collisions using JAM model. Experimentally, the results at RHIC [130–133] indicated the ratio to be unity. Fig 5.6 depicts the ratio as a function of beam energy ($\mathrm{E_{Lab}}$) for different EoS and the values always remain below 2 for all four cases. The ratio $v_4/(v_2)^2$ has been claimed to be in association with the phenomenon of incomplete equilibration in the literature [134]. However, the authors have studied this observable as a function of K^{-1}, number of collisions per particle. With K being the Knudsen number, a dimensionless quantity and a measure of degree of thermalization, it is a function of system size and beam energy. The local equilibration is expected to be reached when $K^{-1} \gg 1$. Moreover, the deviations from ideal hydrodynamics lead to incomplete thermal equilibrium. As the ratio shown in Figure 5.6 deviates from 0.5, giving the impression that the system is not fully equilibrated, thus prevent the use of ideal hydrodynamics in these beam energy regimes. The results here can be used to make some robust claims on the degree of thermalization of the nuclear fireball after comparison with the data available from future experiments at FAIR and NICA.

Last, we attempt to look at the number of constituent quark (NCQ) scaling in the flow coefficients for beam energies examined in this investigation. For this, we especially look at the slope of the directed flow of various species and their combination under the assumption of coalescence sum rule [135, 136] for all four variants of UrQMD and the results are shown in Fig 5.7.

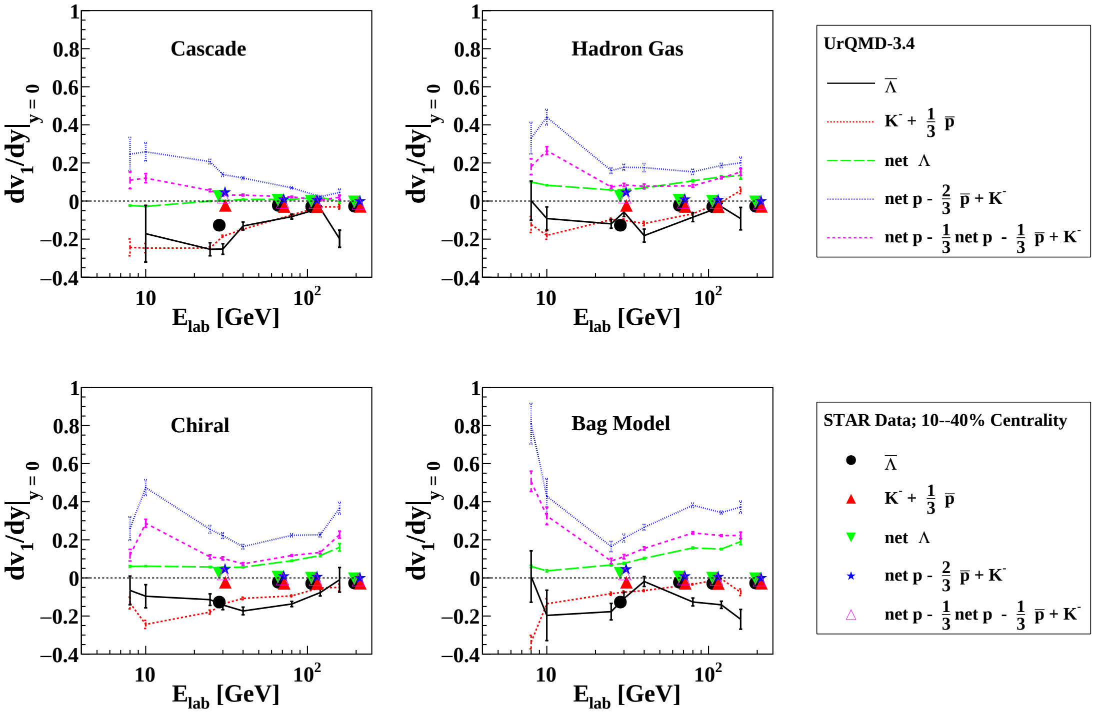

Figure 5.7: Comparison of slope of directed flow of net lambda and anti-lambda with various combinations of hadrons under the assumption of coalescence sum rule as a function of beam energies for different configurations of UrQMD for noncentral (b = 5-9 fm corresponds to approximately 10-40% central) Au-Au collisions. Results from all variants are compared with STAR experimental measurements [135] in 10-40% central Au-Au collisions. Similar kinematic coverage as in data [135] are applied to the simulations.

First, similar to Ref. [135], we compare the dv_1/dy values of $\bar{\Lambda}$ ($\overline{uds}$) (black markers) with (K^- ($\bar{u}s$) + $\frac{1}{3}\bar{p}$ ($\overline{uud}$)) (red markers) where, the same flow for s and $\bar{s}$ and similarly, for $\bar{u}$ and $\bar{d}$ is assumed. The same kinematic coverage as in experimental measurements is applied in our simulations for all species. Though our results are quantitatively higher than the ones presented in Ref. [135], however qualitatively, the sum rule seemed to be followed for these two cases at higher beam energies with a slight hint of violation below 25A GeV which at the moment, can not be strongly claimed due to large uncertainties in all four cases. For the same reason, we plot our results above 8A GeV up to 158A GeV. Moreover, we also look at one more set which is not as simple as the earlier one. As discussed in Ref. [135], different directed flow for transported[1] and produced[2] quarks are expected which are not easy to distinguish in practice. The comparison of dv_1/dy of net Λ (uds) (blue triangular markers) with the calculation comprising different combinations of net p (uud), $\bar{p}$ $(\overline{uud})$ and K^- $(\bar{u}s)$ (pink circle and blue square markers) is shown in Figure 5.7. The combination of K^- and $\frac{1}{3}$ $\bar{p}$ would give s quark which is assumed to replace produced u quark in net p in the first coalescence calculation (pink circle markers). This calculation is expected to hold true at relatively higher energies where most of the quarks are produced and may not be valid at beam energies considered in this investigation, and it seems to be the case from our observations as evident from Figure 5.7 for all four cases of UrQMD. Contrary, in the second calculation where net p is added up with s quark, it is assumed that the transported quarks have a dominant contribution in net p, which is quite suitable in the limit of low beam energies, and one of the quarks is replaced by s quark. This calculation shows a nice agreement with net Λ between 25A–158A GeV which then breaks down below 25A GeV in all four cases. This further may indicate towards possible confinement to deconfinement transition above 25A GeV which has been predicted in prior studies and also in our investigations earlier in this section. The results from our simulations are compared with the available experimental measurements from STAR collaboration [135] and it is noticed that the measurements are overestimated. It is interesting to see the agreement of these sum rule calculations with EoS cases where the underlying degrees of freedom are not partonic and this needs to be understood. However, the scaling behavior using pure transport UrQMD model has also been found earlier [48]. This also brings up the question of whether the underlying assumption of coalescence is indeed the source of this agreement. As mentioned earlier, the particle production in UrQMD at higher energies is performed in terms of string excitation and

---

[1] quarks transported from the initial nuclei

[2] produced in the interactions

subsequent fragmentations as narrated in Refs. [51, 137]. As per the string-excitation scheme, the quark-antiquark or diquark-antidiquark pairs are spontaneously formed in color flux tube between initial quarks and subsequently, mesons and baryons are produced. The produced hadrons undergo multiple scatterings, however, no string will be involved after certain energy limit ($\sqrt{s} < 5$ GeV). This mechanism could give such outcomes shown in Figure 5.7. It is also worth to note that the additive quark model (AQM) is implemented in UrQMD to estimate the unknown hadronic cross-sections [51]. This model assumes the existence of very weakly interacting dressed valance quarks inside the hadrons.

Particle ratios

In this subsection, we investigate and understand the effect of different degrees of freedom and phase transition on the yield of the final state particles. For this, we obtain various particle ratios, namely, strange to non-strange, anti-particle to particle, and compare them with the available data. For central collisions, the K^+/π^+ ratio, has been studied in literature as a unique measure of the onset of deconfinement [138]. It will be interesting to see the behavior of this observable in case of noncentral collisions. We estimate various particle ratios to procure insights about the medium properties by studying the impact of different equations of state. In Figure 5.8, we show ratio of K^-/π^-, K^+/π^+ and $(\mathrm{K}^+ + \mathrm{K}^-)/(\pi^+ + \pi^-)$ as a function of beam energy for different cases of EoS.

In the left plot, K^-/π^- shows a monotonic rise for all beam energies except for Bag Model EoS which saturates after 20A GeV. In the middle plot, K^+/π^+ ratio shows a similar increasing behavior up to 4A GeV and then start to decrease with hint of stronger drop in case of Bag Model EoS between 20A–30A GeV. In the right most plot, $(\mathrm{K}^+ + \mathrm{K}^-)/(\pi^+ + \pi^-)$ is obtained as a function of beam energy and similar splitting seen earlier between 20–30A GeV in presence of first order phase transition is observed. The ratio seems to saturate beyond this range in all other scenarios. Due to the unavailability of the measurements in the desired centrality class, both K^-/π^- and K^+/π^+ ratios are compared with the experimental data from NA49 [139] and STAR experiment [140] at three different centralities as these seem to cover impact parameters considered here. To demonstrate the centrality and beam energy dependence, we also

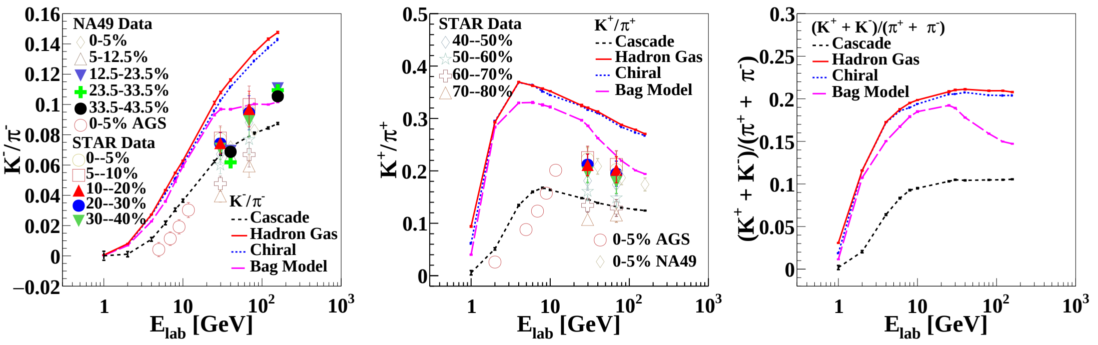

Figure 5.8: K^- to π^-, K^+ to π^+ and $(K^+ + K^-)/(\pi^+ + \pi^-)$ ratio as a function of beam energy for different configurations of UrQMD for noncentral (b = 5-9 fm corresponds to approximately 10-40% central) Au-Au collisions and their comparison with AGS [64], NA49 [139, 148] and STAR experimental measurements [140] in Au-Au, Pb-Pb and Au-Au collisions for all available centralities, respectively. Vertical bars on the data denote statistical uncertainties.

compare our predictions of various particle ratios with measurements at most central as well as peripheral collisions. From Figure 5.8, it can be seen that the chiral and hadron gas EoS are able to reproduce the trend set by data in both these ratios however the magnitude is overestimated. Furthermore, we also look at the antiparticle to particle ratio for different EoS. In Figure 5.9, $\mathrm{K}^+/\mathrm{K}^-$, π^+/π^- and $\bar{\mathrm{p}}/\mathrm{p}$ ratios are depicted for all four cases of fireball evolution. $\mathrm{K}^+/\mathrm{K}^-$ ratio shows an increase for all beam energies and EoS, however, no sensitivity to a specific EoS is detected. In the middle plot of Fig 5.9, we see same magnitude of π^+/π^- ratio for all EoS at all energies beyond 4A GeV with decreasing trend as a function of beam energy. Moreover, data seem to favor hybrid mode for both ratios with slight underestimation by hybrid in the case of $\mathrm{K}^+/\mathrm{K}^-$ ratio. The anti-proton to proton ratio is shown in the right most plot and compared with experimental data. Measurements are relatively underestimated by the model in all cases of EoS.

Finally, we study the p/π^+ and $\bar{\mathrm{p}}/\pi^-$ ratios and compare them with the available data as shown in Figure 5.10. In the former case, the ratio is inversely proportional to beam energy and shows similar magnitude for all hybrid cases with slightly higher magnitude in cascade case at all beam energies. The ratio using hybrid mode shows good agreement with the experimental measurement as depicted in the left plot. In the right plot of Figure 5.10, $\bar{\mathrm{p}}/\pi^-$ ratio shows similar trend as data and sensitivity to first order phase transition. The reader may take note of the fact that for protons the com-

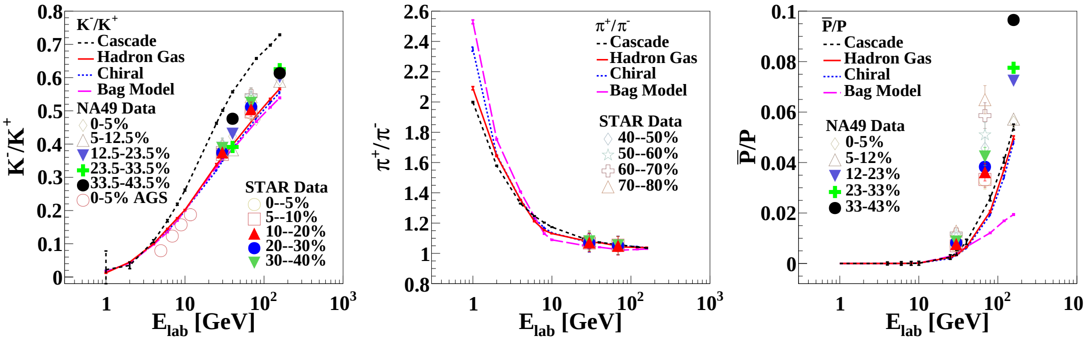

Figure 5.9: K^- to K^+, π^+ to π^- and anti-proton to proton ratio as a function of beam energy for different configurations of UrQMD for noncentral (b = 5-9 fm corresponds to approximately 10-40% central) Au-Au collisions and their comparison with AGS [150], NA49 [139] and STAR experimental measurements [140] in Au-Au, Pb-Pb and Au-Au collisions for all available centralities, respectively. Vertical bars on the data denote statistical uncertainties.

parison of the UrQMD model calculations with the experimentally measured data are to be accepted with a caveat. In low energy collisions ($E_{lab} \lessapprox$ 10A GeV) the production of light nuclei (d,t,He) has a non-negligible contribution. The model calculates the so-called primordial nucleons which still contain the contribution of the nucleons bound in the light nuclei. This concerns all observables involving protons. However for anisotropic flow coefficients the effect of bound proton is considerably reduced because of their independence of proton multiplicity. But it is important for the observables like particle ratios presented in Figure 5.9 and Figure 5.10 involving proton yield, as well net-proton rapidity distribution shown in Figure 5.11 (net subsection). A consistent way to take the light nuclei into account is by coalescing the final state nucleons from UrQMD. The basic philosophy behind coalescence approach is to check for clusters of nucleons at freeze-out with a very small momentum difference that happens to be very close to each other. However, this is beyond the scope of the present work.

Net-proton rapidity spectra

Understanding the in-medium properties of stopped protons by studying their rapidity distributions have been a promising observable. In Refs. [141–145], multiple of studies in this direction has been performed. It has been argued that the irregularities in the distribution of stopped protons may well be the consequence of onset of deconfinement

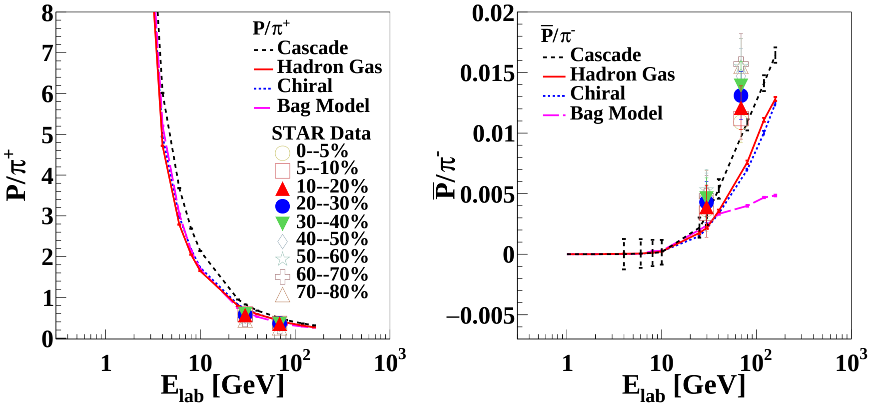

Figure 5.10: Proton to π^+ and anti-proton to π^- ratio as a function of beam energy for different configurations of UrQMD for noncentral (b = 5-9 fm corresponds to approximately 10-40% central) Au-Au collisions and their comparison with STAR experimental measurements [140] in Au-Au collisions for all available centralities. Vertical bars on the data denote statistical uncertainties.

transition. This occurs due to inherited softest point in the nuclear equations-of-state in the vicinity of a phase transition. Such investigations are generally performed in central collisions however, it is also worth to check this in noncentral collisions as well. The shape of rapidity spectra at midrapidity may contain very crucial information about medium and believed to be sensitive to the underlying nuclear equations of state. Therefore, we look at the net-proton rapidity distribution at different beam energies and equations of state. In Figure 5.11, we show rapidity distribution of net-protons at mid rapidity for all energies and EoS considered in this work. Rapidity spectra remain flat at high beam energies in case of cascade mode in contrast to hybrid mode where it shows a very interesting feature. These results are compared with the measured rapidity spectra at available energies from E917 [151] and NA49 [152] experiments in the centrality regions covering investigated range. Our results overestimate the measurements at all available beam energies. As the irregularities in the shape of rapidity spectra at midrapidity can potentially help in explaining the dynamics of the medium, we quantify the nature of simulated as well as the measured spectra at midrapidity by calculating the double derivative of the rapidity spectra at midrapidity i.e. global minima or maxima as shown in Figure 5.12. This quantity is identical to the one obtained in the Refs. [141–145] and is referred as reduced curvature. For this, the rapidity distributions of net-protons are fitted with polynomial at the midrapidity for all beam energies

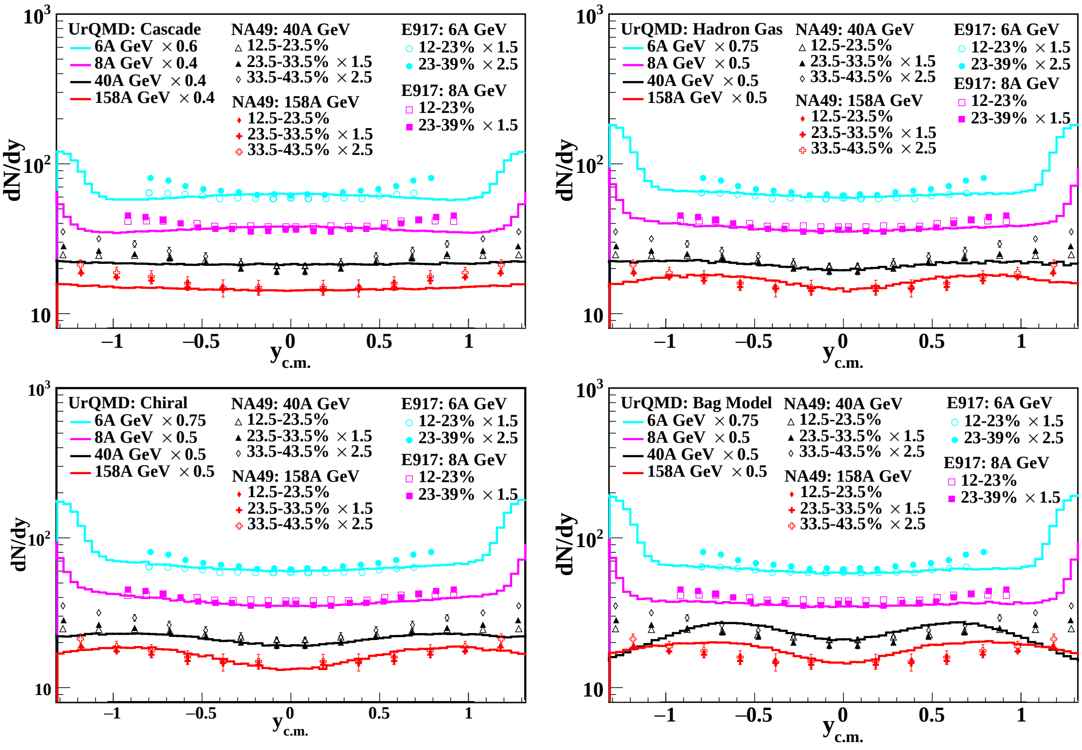

Figure 5.11: Rapidity spectra of net-protons at various beam energies for different equations of state for noncentral (b = 5-9 fm corresponds to approximately 10-40% central) Au-Au collisions and its comparison with the measured rapidity spectra of net-protons in Au-Au and Pb-Pb collisions by E917 [151] and NA49 [152] collaborations, respectively. Both simulation results and measurements are scaled for better visualization. Vertical bars on the data denote statistical uncertainties.

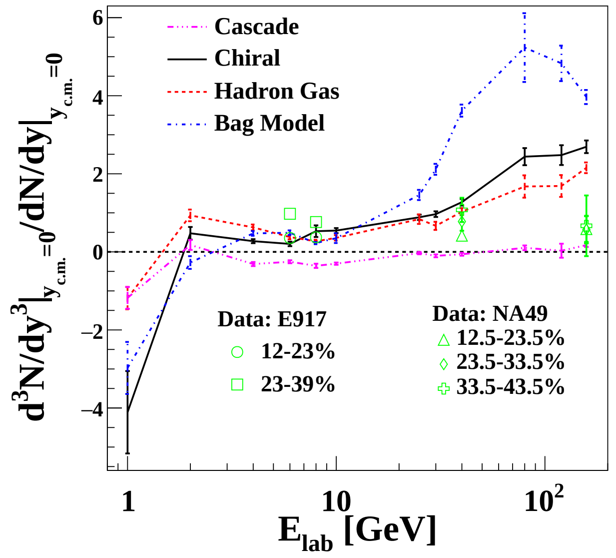

Figure 5.12: Reduced curvature of rapidity spectra of net-protons as a function of beam energy for different configurations of UrQMD for noncentral (b = 5-9 fm corresponds to approximately 10-40% central) Au-Au collisions at midrapidity (-0.5 $< y_{c.m.} <$ 0.5) and its comparison with the calculated reduced curvature of measured rapidity spectra of net-protons in noncentral Au-Au and Pb-Pb collisions by E917 [151] and NA49 [152] collaborations, respectively.

and EoS. As shown in Figure 5.12, the reduced curvature in the case of cascade remains constant and zero for all energies. As soon as the hydrodynamical evolution is introduced, the corresponding observable show some sensitivity as a function of beam energy. Similar to simulations, the reduced curvatures of measured rapidity spectra shown in Figure 5.11 are calculated and it is seen that it remains almost flat, however, slightly higher than cascade case at all beam energies. It almost matches with hybrid scenario at 6A, 8A and 40A GeV and is slightly lower in hybrid mode case at 158A GeV. We do not notice the so-called “peak-dip-peak-dip” irregularity as seen in the experimental observations and in the central collisions [141–145].

It may also be mentioned that in Ref. [141–145], the contribution of nucleons bound in the light nuclei was subtracted from primordial nucleons by means of the coalescence, whereas our results still suffer form the uncertainty due to inclusion of contribution from bound protons, as detailed earlier. Still, it is interesting to note that this observable has led to show the sensitivity between Chiral and Hadron gas EoS beyond 25A GeV which is the same energy at which we have seen some interesting features for other observables investigated in this study. The magnitude and slope of reduced curvature are highest for Bag Model and decreases for Chiral to Hadron gas beyond 25A GeV. In the end, it is worth mentioning that the net-protons are the only species for which any sensitivity to the underlying degrees of freedom has been noticed, especially for the observables related to longitudinal dynamics such as directed flow and rapidity.

5.4 Effect of various particlization scenarios

Back to the hybrid models, after completion of fluid dynamic evolution, the later stage is described using the transport approach as the medium is expected to be away from the equilibrium. The conversion of fluid-based description to the particle-based description is known as particlization, which is a technical terminology. The Cooper-Frye procedure [146] is used to evaluate the particle distributions on the boundary where this conversion is performed. It is essential here to note that this switching of description is not freeze-out, as in principle, after freeze-out, there should not be any rescattering and, therefore, no need to have transport description [113]. Various variants of freeze-out hypersurfaces or particlization models are available in the UrQMD hybrid model. One can aim to extract some insights about the medium by observing the response of different observables to these variants. The choice of particlization model can further affect the evolution of the particles after hadronization as well as freeze-out and hence observables, such as anisotropic flow, particle ratios, rapidity spectra, and so on. Since the corresponding physical stage to particlization is not available in actual evolution of the QCD matter, its optimization is necessary to describe the experimental measurements.

A large amount of investigations have been performed to describe the medium properties using different equations-of-state and freeze-out scenarios. In [119], Hanburt-Brown-Twiss (HBT) radii of pions has been studied for energy range $\mathrm{E_{Lab}} = 20A - 160A$ GeV for different equations-of-state in the UrQMD model. Effect of gradual particlization (GF) and isochronous particlization (ICF) scenarios in combination with hadron gas (HG) EoS are also observed. In [120], multiplicity and mean transverse mass excitation function have been analyzed for available freeze-out (GF and ICF) scenarios and equations-of-state in UrQMD model over energy range $\mathrm{E_{Lab}} =$

$20A - 160A$ GeV for central Au-Au/Pb-Pb collisions. In [117], directed flow has been investigated for identified particles. It is found out that neither combination of EoS and freeze-out scenario is able to predict the experimental measurements.

In the present study, we aim to investigate the effect of various particlization scenarios using multiple particlization modes in the UrQMD model for the available variety of the nuclear equations-of-state. As none of the previous works have examined the effect of all possible combinations of EoS and freeze-out modes available in UrQMD model, it will be useful to systematically investigate all results at a single place[3]. For this, we are using same simulated mid-central ($5 < b < 9$ fm) Au–Au collision events which we use in our previous study, using the UrQMD model for beam energies ranging from 1A–158A GeV for different particlization models and EoS. Our objective is to find the best possible combination among the various permutations of UrQMD variants which describe the data best.

5.4.1 Results and Discussion

In this section, we present the outcomes of our investigation of the dependence of various experimental observables on the available particlization modes available in the UrQMD hybrid model. To begin, we investigate various flow coefficients for a range of beam energies using different particlization scenarios. Then we see the effect of particlization prescriptions on particle production by looking at strange to non-strange ratio, baryon to mason ratio, etc. Then we look at the net-proton rapidity spectra for different particlization modes in combination with different EoS.

Anisotropic flow coefficients

In regards to our present investigations, the study of anisotropic flow coefficients for different particlization models is essential. The reason being the choice of hypersurface and switching criteria allows the fluid dynamic evolution to cease at different times. Particlization may affect the flow of the species as it will spend more or less

---

[3] There are some studies for EoS and freeze-out dependence available in the literature [113, 117]. But these studies do not cover all possible nine combinations and it will be nice to show all possible combinations in the same place.

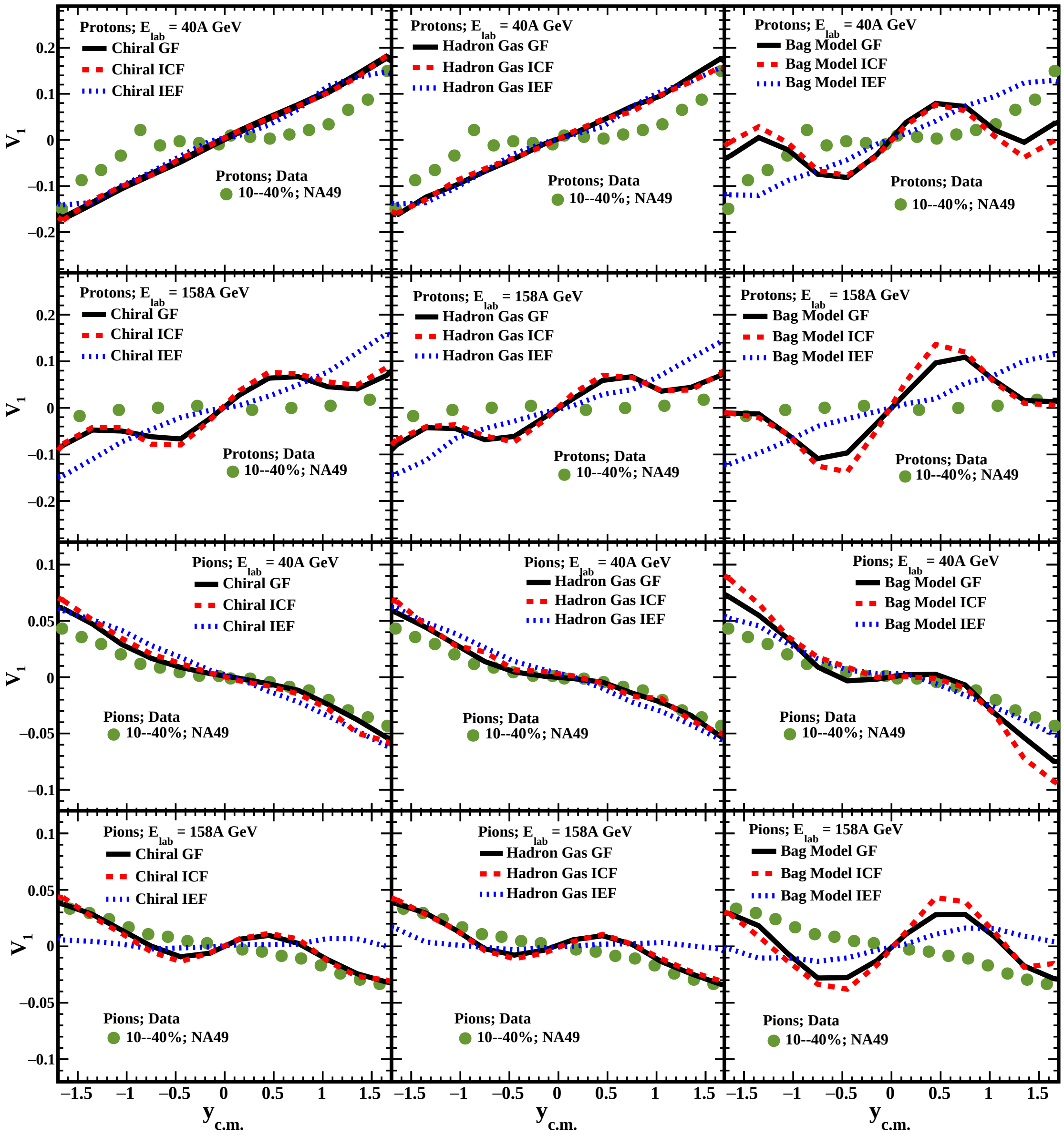

Figure 5.13: Comparison of directed flow of protons (upper two panels) and pions (bottom two panels) as a function of rapidity with experimental measurements at 40A and 158A GeV [121] at SPS for different EoS and particlization modes of UrQMD with measured directed flow for noncentral (b = 5-9 fm) Au-Au collisions.

time in evolution. Directed flow is sensitive to longitudinal dynamics among various anisotropic flow coefficients. So we estimate the directed flow of pions and protons as a function of rapidity for various particlization scenarios and equations of state as shown in Figure 5.13. The results are compared with the experimental data from NA49 experiment [121] at SPS for similar centrality regions (10–40%) at 40 and 158A GeV. In the case of pions for 40A GeV, the results shown are closer to experimental data compared to other studies. If we look at pions and protons for higher beam energy at 158A GeV, the iso-energy particlization shows more favorable results than the other two particlization modes. One interesting point to note here is that the so-called "wiggle" structure is less pronounced in the cases where IEF is employed compared to the other two scenarios. As discussed in Ref. [124], there may be some factors on which the shape of the wiggle, i.e., magnitude of v_1 and rapidity range, depends and these are space-momentum correlation, amount of stopping and initial beam-target rapidity. Contributions of these factors may be different for different EoS and particlization scenarios, resulting in different shapes of the wiggle. However, more study is needed in this direction to make any strong claims.

We choose the slope of the directed flow of protons as our next observable for investigation. The slope of directed flow at mid-rapidity is an interesting observable and contains insights into the medium properties. In Figure 5.14, the results for proton with $p_{\mathrm{T}} < 2$ GeV/c are compared with the measurements of E895 [122], NA49 [121], and STAR [123] experiments.

It can be seen that the slope of the directed flow of protons does not show any sensitivity to the underlying degrees of freedom below 20A-30A GeV for all particlization scenarios. This observation agrees with the claims made in previous study in this chapter [5] and is attributed to the short lifetime of hydrodynamical phase. In our previous study, we observed a splitting among the comparison of various EoS [5]; here, similar splitting is exhibited around 20–30A GeV. This suggests that various particlization models and EoS behave differently above this energy range, perhaps indicating the threshold for the possible onset of deconfinement. However, a detailed study in this direction is needed to make any firm statement on this.

Moving on to elliptic flow (v_2), which was estimated for protons and pions

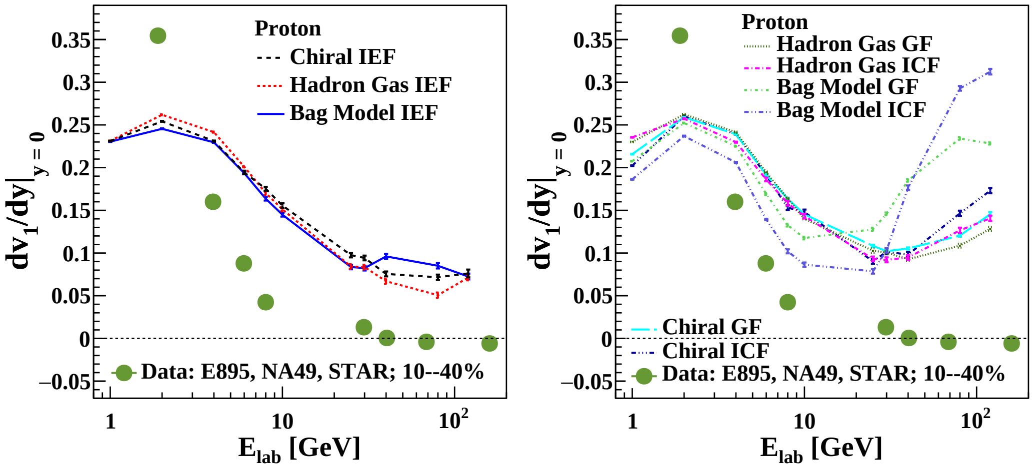

Figure 5.14: Comparison of slope of the directed flow of protons as a function of beam energy at midrapidity for different EoS and particlization modes of UrQMD for non-central (b = 5-9 fm corresponds to approximately 10-40% central) Au-Au collisions with E895 [122] and STAR [123] experimental measurements in Au-Au collisions and with NA49 [121] experimental measurements in Pb-Pb collisions.

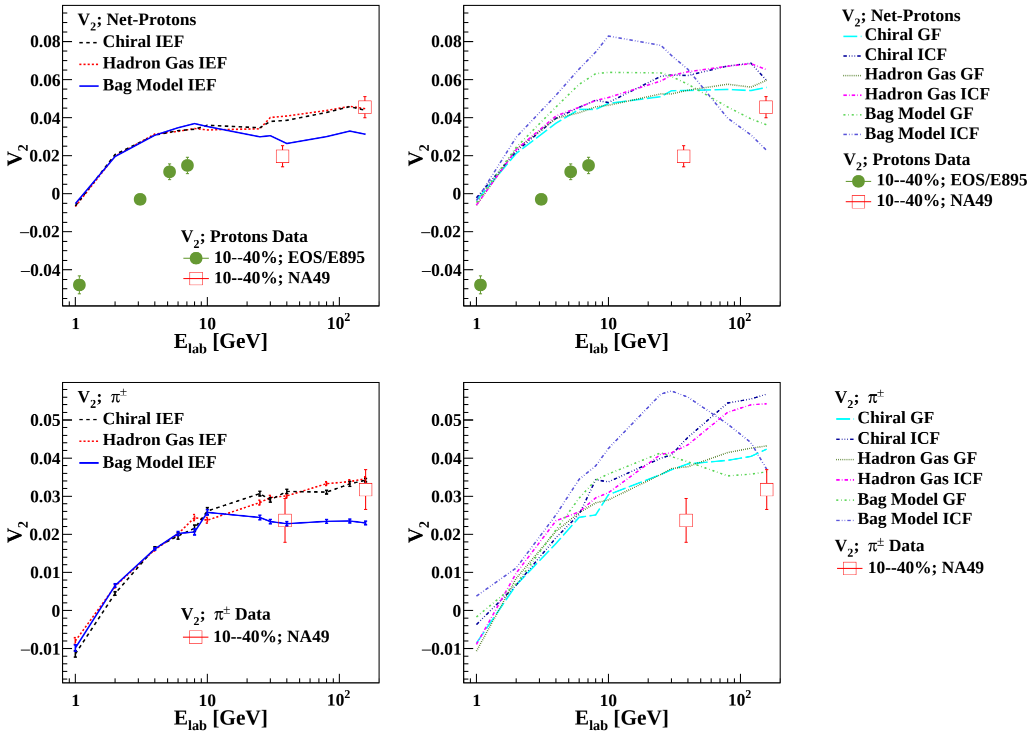

Figure 5.15: p_{T} integrated elliptic flow v_2 of net-protons, and pions as a function of beam energy at midrapidity (-0.5 $< y_{c.m.} <$ 0.5) for different EoS and particlization modes of UrQMD for noncentral (b = 5-9 fm corresponds to approximately 10-40% central) Au-Au collisions. v_2 of net-protons and pions for $p_{\mathrm{T}} <$ 2 GeV/c are compared with available E895 and NA49 experimental measurements [55, 121] respectively in the investigated beam energy range in Au-Au and Pb-Pb collisions.

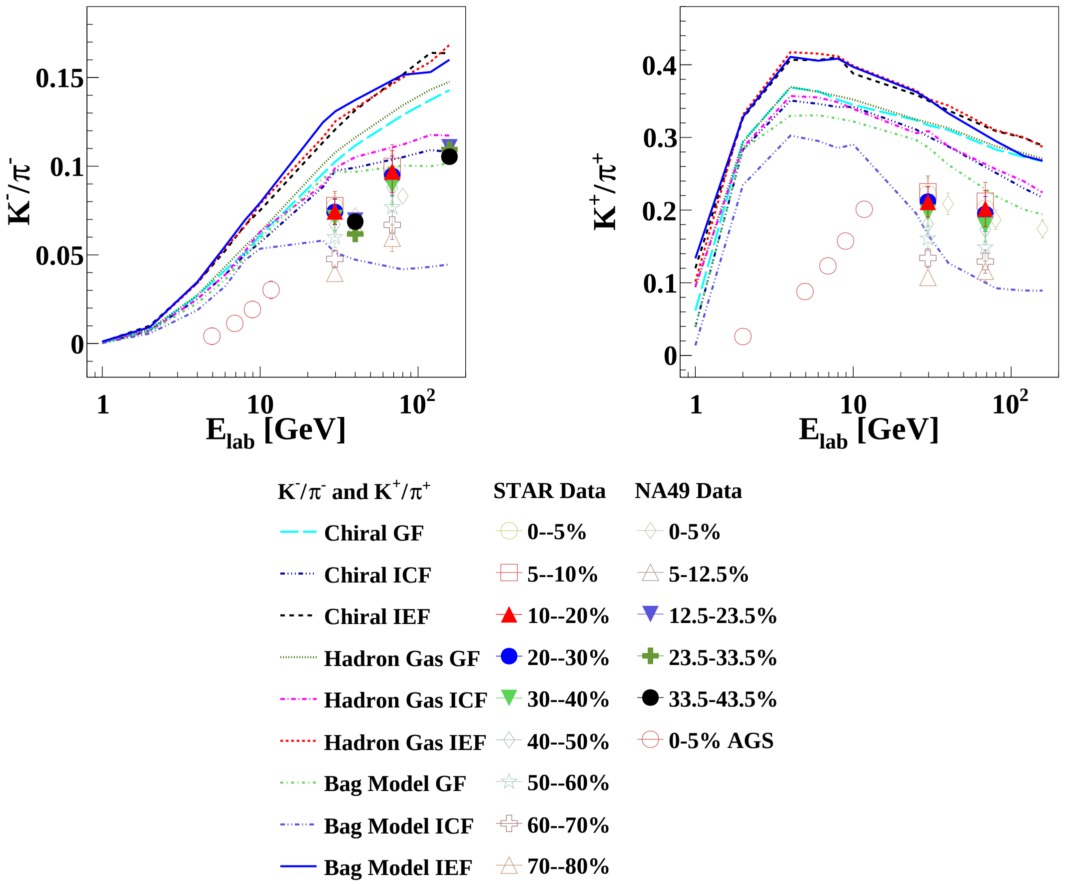

Figure 5.16: K$^-$ to π^-, and K$^+$ to π^+ ratio as a function of beam energy for different EoS and particlization modes of UrQMD for noncentral (b = 5-9 fm corresponds to approximately 10-40% central) Au-Au collisions and their comparison with AGS [64], NA49 [139, 148], and STAR experimental measurements [140] in Au-Au, Pb-Pb, and Au-Au collisions respectively for all available centralities. Vertical bars on the data denote statistical uncertainties.

and studied as a function of beam energies for different EoS and particlization models as shown in Figure 5.15. The observable is compared with measurements from EOS/E895 [55] and NA49 [121] experiments. Similar to the previous two observables, v_2 in the case of IEF scenario shows better agreement with experimental measurements at high beam energies, whereas v_2 for ICF case diverges from the data even more than default GF scenario. Neither particlization model agrees with measured v_2 at low beam energies. One of the observations is that v_2 using the bag model shows non-monotonous behavior irrespective of the particlization modes for both species. It seems that because of the more realistic iso-energy density hypersurface in the IEF scenario, the results are in agreement with the experimental data.

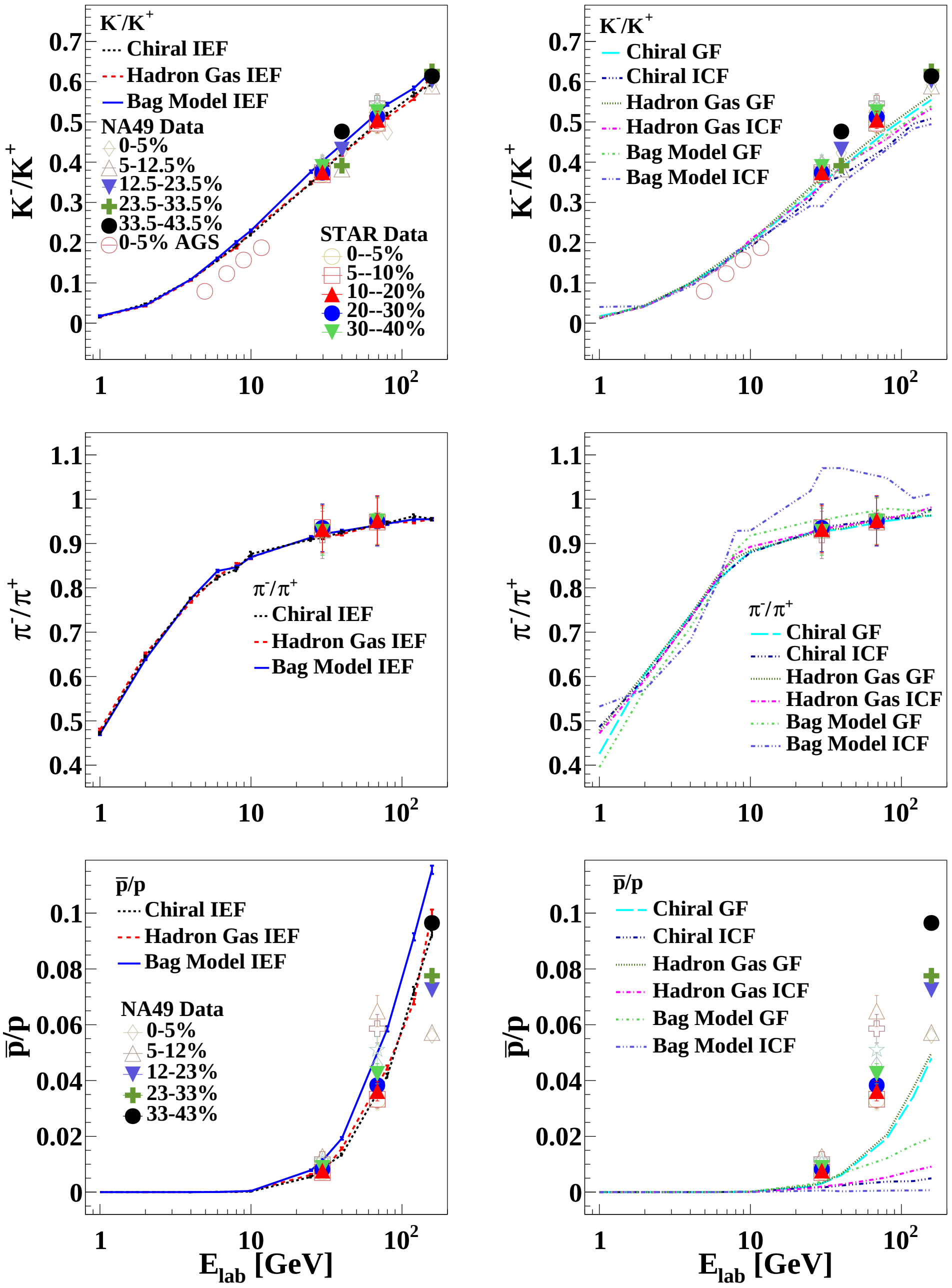

Figure 5.17: K^{-} to K^{+}, π^{-} to π^{+} and anti-proton to proton ratio as a function of beam energy for different EoS and particlization modes of UrQMD for noncentral (b = 5-9 fm corresponds to approximately 10-40% central) Au-Au collisions and their comparison with AGS [150], NA49 [139] and STAR experimental measurements [140] in Au-Au, Pb-Pb and Au-Au collisions respectively for all available centralities. Vertical bars on the data denote statistical uncertainties.

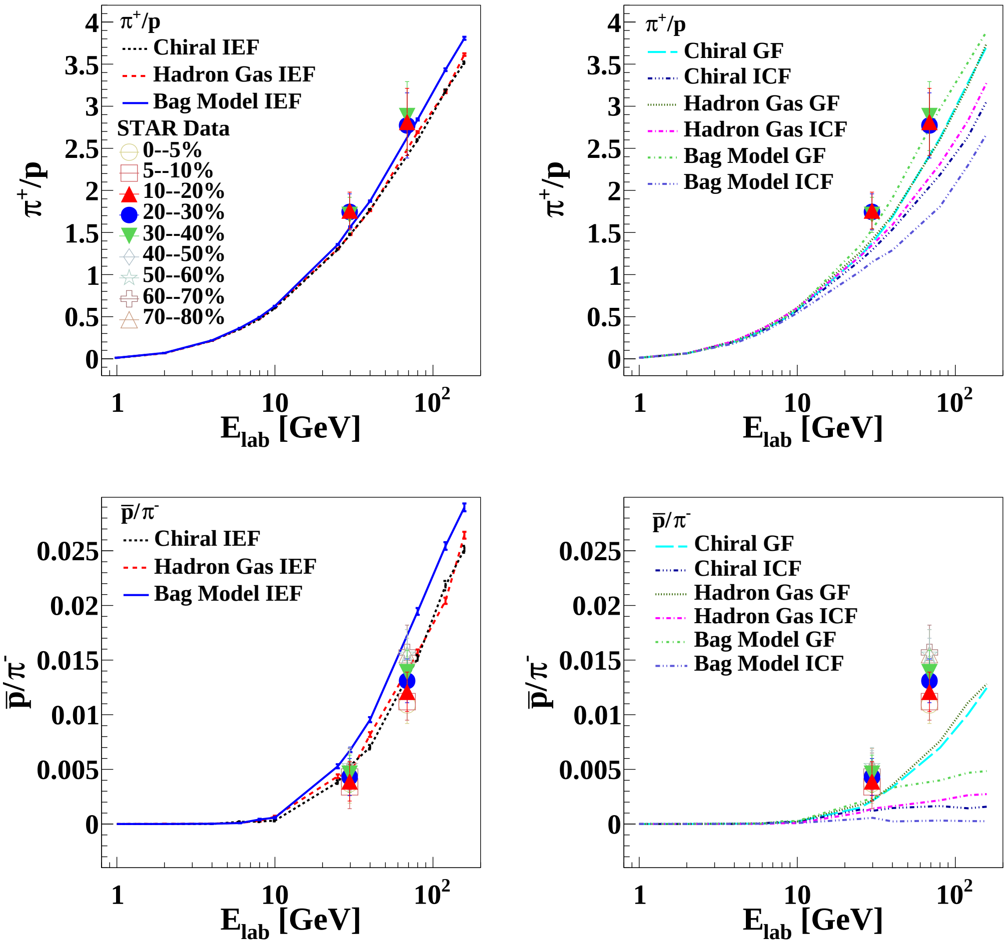

Figure 5.18: π^+ to proton and anti-proton to π^- ratio as a function of beam energy for different EoS and particlization modes of UrQMD for noncentral (b = 5-9 fm corresponds to approximately 10-40% central) Au-Au collisions and their comparison with STAR experimental measurements [140] in Au-Au collisions for all available centralities. Vertical bars on the data denote statistical uncertainties.

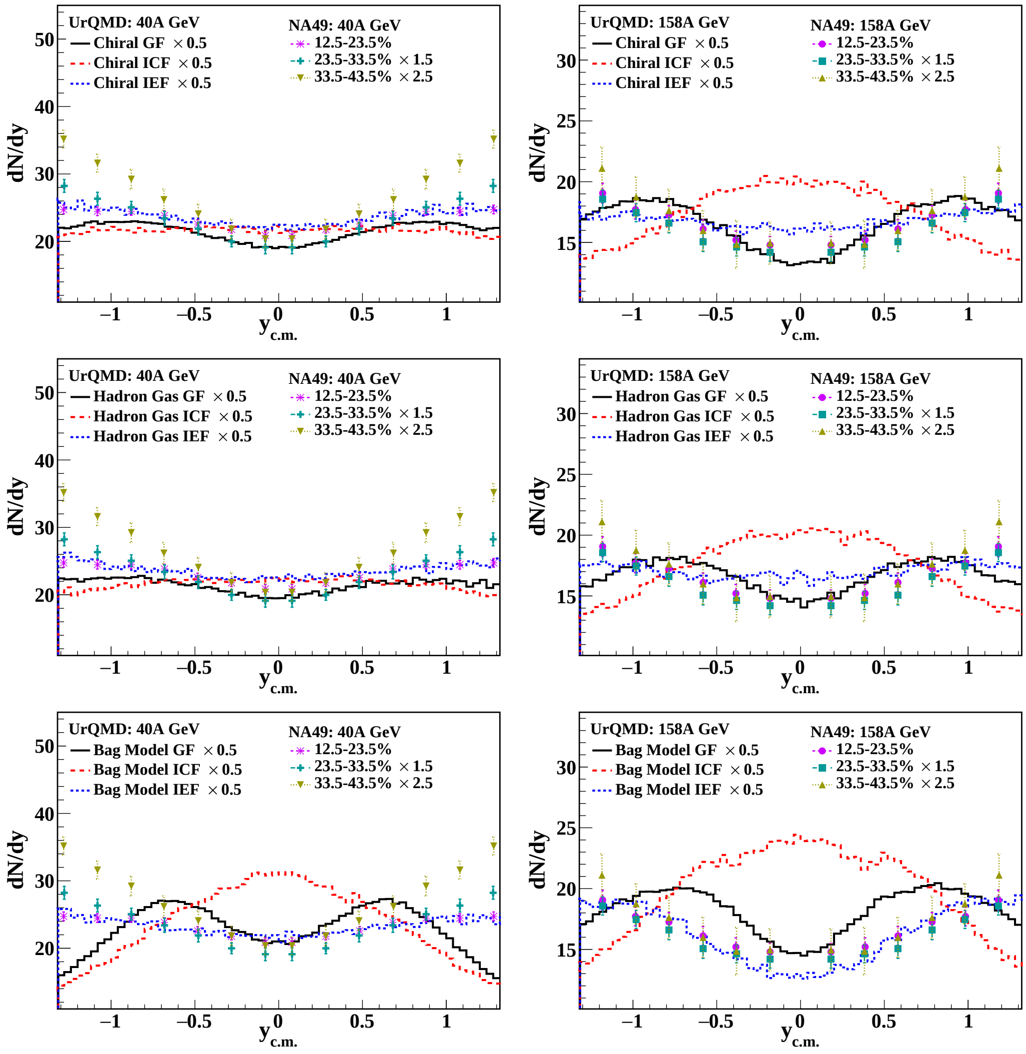

Figure 5.19: Rapidity spectra of net-protons at 40 and 158A GeV beam energies for different EoS and particlization modes of UrQMD for noncentral (b = 5-9 fm corresponds to approximately 10-40% central) Au-Au collisions and their comparison with the measured rapidity spectra of net-protons in Au-Au and Pb-Pb collisions by E917 [151] and NA49 [152] Collaborations, respectively. Both simulation results and measurements are scaled for better visualization. Vertical bars on the data denote statistical uncertainties.

Particle ratios

In this subsection, we study the effect of different particlization modes under different EoS on particle production in the final state. Particle ratios might show sensitivity to the underlying particlization mode as various criteria for switching from fluid-based to particle-based description can alter the chemical composition of the system. Particle ratios such as K^+/π^+ have been studied in the literature, especially in central heavy-ion collisions, and are believed to be crucial to providing critical information about the medium, such as the onset of deconfinement [138]. Investigation of such ratios in noncentral collisions can be exciting and might infer the medium properties.

We start with the strange-to-non-strange particle ratios, such as K^-/π^- and K^+/π^+ which is shown in Figure 5.16 as a function of beam energies. The ratios are obtained for various particlization scenarios as well as EoS and compared with experimental data. As expected, the ratios are sensitive to the underlying particlization scenario. The unavailability of the data in the desired centrality classes mandates us to compare in three different classes in NA49 [139, 148] and STAR experiments [140] which covers the impact parameter region under study. Moreover, the ratio was also compared with measurements in various centrality classes to understand the centrality and beam energy dependence. When ICF scenario is used, there is a non-monotonous trend in the ratio K^-/π^-. Here, as our main focus is to see the difference between available freeze-out scenarios, point to be noted is that the fireball region is considered to be in equilibrium in this study. To make it more reasonable, core-corona separation method [149] which is not implemented here, could be used to distinguish hot equilibrated core from the outer dilute corona region. It will improve the description of strange particle ratio. Although it will not affect the non-strange particle production and hence particle to anti-particle ratio and baryon to meson ratio [149].

The particle to anti-particle ratios such as $\mathrm{K}^-/\mathrm{K}^+$, π^-/π^+ and $\overline{\mathrm{p}}/\mathrm{p}$ are estimated as a function of beam energy and shown in Figure 5.17. A monotonous trend is observed in all three ratios for all variants of EoS and particlization modes. The ratios have shown excellent agreement with experimental measurements in the IEF scenario for all three cases of EoS. Moreover, both in GF as well as ICF modes, the ratios $\mathrm{K}^-/\mathrm{K}^+$, π^-/π^+ have shown agreement with data, but the same cannot be said in the case of $\overline{\mathrm{p}}/\mathrm{p}$. The ratios seem more sensitive to the particlization scenarios because of the possible change in the particle chemistry.

We also estimate the baryon to meson ratio, namely, p/π^+ (shown as the inverse for better visualization) and $\overline{\mathrm{p}}/\pi^-$ which is shown in Figure 5.18. Agreement with the data is also seen in the case of IEF scenario for all EoS as depicted in Figure 5.18. In the case of π^+/p, the GF scenario is also able to reproduce the data compared to ICF mode. From both Figs. 5.17 and 5.18, it is worth noting that there is negligible anti-proton production in the ICF scenario, even at higher beam energies. From this investigation, it seems evident that the IEF scenario brings more clarity to understanding and interpreting the results.

We want to bring to the reader's attention that the comparison of protons from the UrQMD model with the experimental data should be accepted with caution. In the region of low beam energy, $E_{lab} \lessapprox 10$A GeV, there is a non-negligible contribution of light nuclei production. Primordial nucleons calculated by the model still have a contribution from bound nucleons. This involved all the proton observables in this article. The way out in such a case is to coalesce final state nucleons in UrQMD into light nuclei. The basic principle for coalescence is to find the nucleon clusters with small momentum and position differences. Such study has its own importance; however, it is beyond the reach of this present investigation. This may not be as significant for anisotropic flow as for particle ratios since the flow coefficients are independent of proton multiplicity. As for particle ratios, this contribution is important as well as for net-rapidity distributions (see next subsection).

Net-proton rapidity spectra

From the rapidity distributions of the net-protons, the in-medium properties of stopped protons can be understood. It has been argued that irregularities at the mid-rapidity of the longitudinal spectra of net-protons can be the consequence of the possible onset of the deconfinement. A possible reason behind this may well be the inherited softest point in the nuclear equation-of-state near the phase transition. In the context of this study, the particlization scenario also can play a crucial role since the production of particles can be sensitive to the conversion from fluid to the particle-based description.

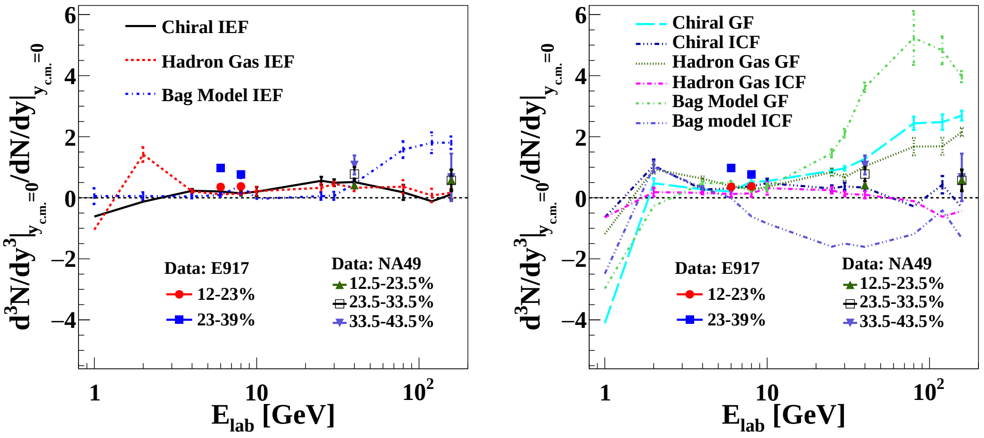

Figure 5.20: Reduced curvature of rapidity spectra of net-protons as a function of beam energy for different EoS and particlization modes of UrQMD for noncentral (b = 5-9 fm corresponds to approximately 10-40% central) Au-Au collisions at midrapidity ($-0.5 < y_{c.m.} < 0.5$) and its comparison with the calculated reduced curvature of measured rapidity spectra of net-protons in noncentral Au-Au and Pb-Pb collisions by E917 [151] and NA49 [152] Collaborations, respectively.

Since such investigations are primarily performed in the central collision, it is also equally important to study in noncentral collisions. In this investigation, the rapidity distribution of net-proton is estimated for beam energies 1A-158A GeV for various EoS and particlization scenarios. However, the rapidity spectra of net-protons in selected beam energies are shown in Figure 5.19. The simulated results are compared to the experimental measurements from E917 [151] and NA49 [152] in centralities covering the impact parameter region under investigation. Even at first glance, one can see that rapidity spectra using ICF and GF scenarios are not seem to be in agreement with the measurements. However, the IEF scenario seems to be performing exceptionally well.

The shape of the rapidity spectra is quantified as a reduced curvature, and its excitation function is studied to gain more insights and have more differential comparisons. In this analysis, the reduced curvature is estimated by fitting the rapidity spectra of net-protons at mid-rapidity using sixth order polynomial, which is shown in Figure 5.20. The reduced curvature of net-proton rapidity distributions for different particlization models and EoS compared with experimental measurements [151, 152]. The reduced curvature for measurements is also estimated in a similar way as for simulations. The results with the IEF scenario for all three cases of EoS show nice agreement with the data. In the ICF scenario, the reduced curvature underestimates the experimental measurements for hadron gas and bag model EoS. One interesting observation from the above figure is that there is very high sensitivity to the particlization scenario in the case of bag model EoS at high beam energies, so much so that we see large negative values of reduced curvature in the case of ICF scenario and large positive values in case GF scenario. We want to mention that the authors of Refs [141–145] have subtracted the contribution of nucleons bound in nuclei from primordial nucleons, which we have not done in our analysis. Therefore, our results suffer from uncertainties due to the contribution of bound protons.

Chapter 6

Summary and Outlook

The CBM experiment is one of the upcoming experiments which will explore the QCD phase diagram in high net baryon density and moderate temperature regions. India is participating in the CBM experiment by taking responsibility for developing the MuCh detector system. We have contributed to the development of the CBM experiment by investigating a cooling system for the first two stations of the MuCh detector. To summarize, we presented details of the concept, design, fabrication, and test performances of a water-based cooling prototype under investigation for the MuCh detector system in the CBM experiment. One small-size and two real-size prototypes of the cooling system were developed, and their performances were studied in detail. A setup of the three prototype modules was developed at Bose Institute, Kolkata, where two different configurations were studied.

Tests for the small-size prototype were conducted using a copper plate and an emulated heat load in the laboratory while the real-size prototypes were tested during the test beam experiment at the CERN SPS H4 beamline facility with the actual heat load and under realistic experimental conditions.

The results obtained from the study of copper plate-based small-size prototype validated the proof-of-principle of the concept and design of the cooling system. The real-size prototypes were built with aluminum plates using two different mechanical techniques. A novel concept of control mechanism is realized and tested by integrating the ATMEGA328P microcontroller with the cooling system to monitor and control the temperature of the cooling plate.

The experiences of operating the real-size prototypes during the test beam experiment at CERN SPS and the test results confirmed that the system under investigation is feasible in all aspects and efficient enough to meet the cooling requirement of the

MuCh detector system in the CBM experiment. Three modules are also tested in both series and parallel configurations to select the suitable configuration for each layer of the tracking station. It was found that parallel configuration would be a better option for the water distribution of modules in the final experiment.

Several other challenges are, however, to be further investigated and addressed before realizing the full cooling setup for the integration in the experiment. The two most important issues under consideration are the scalability of the system to meet the experimental requirement and the development and integration of a leak detection and protection unit or a leakless coolant flow mechanism to the existing system.

In the simulation, we have contributed to simulation studies as well to increase the performance and for better tuning of the detectors. We have studied the data rate handling capability of the MuCh detector through simulation. Using the GEANT3 and GEANT4 transport engines, the MuCh detector data rate has been calculated using a coherent source primarily from ion-ion collision events. It has been observed that the contribution of secondary particles is more using the GEANT4 transport engine compared to GEANT3. The maximum pad hit rate for each station of the MuCh detector has been estimated after studying the occupancy for each detector station. This study is essential to see the minimum data rate handling capacity for the detectors that are used for different stations of the MuCh detector.

Further, we investigate a PID framework working on the principle of Bayesian probability to detect hadrons with more accuracy, mainly at a higher p_T range which is not possible by the traditional cut-based methods. The PID framework has been tuned to detect hadrons more efficiently at a higher p_T range. DCA value is used to reduce the contribution of the false signal. The same predicted purity values are checked on combinations of different event generators and transport engine setups to assure the ability of the used PID framework, and we get suitable outcomes for all configurations. It is to be noted that by utilizing this framework, we can significantly improve efficiency and reduce false particle detection for hadrons.

As a part of the phenomenological study, first, we have made dedicated efforts to understand the impact of various nuclear equations of state on the several observables to understand the nuclear matter produced in the low energy collisions of heavy ions in a wide range of beam energies, 1A–158A GeV. The UrQMD model with intermediate hydrodynamical evolution was employed with different nuclear equations-of-state such as Hadron gas, Chiral + deconfinement, and Bag model. We started by examining the anisotropic flow coefficients of charged and identified hadrons in the above-mentioned beam energy range. A unique feature at 25–30A GeV in the energy dependence of the slope of the directed flow of charged hadrons, protons, and net-protons at mid-rapidity was observed. The slope using Bag Model EoS, showed a splitting, leading to a sharp rise compared to the other two equations of state. This may be attributed to the incorporated first-order phase transition in the former case. A similar feature was observed for directed flow as well. Apart from the splitting, the dip within a certain energy range for these equations-of-state hints towards the possible onset of deconfinement. Moreover, we noticed that study of net-proton rapidity distribution certainly brings out the sensitivity to underlying degrees of freedom in chiral and hadron gas EoS beyond 20–30A GeV beam energy; however, more evidence in this direction is required to make any robust claim. Along with this, efforts have been made to study the effect of different EoS on elliptic flow (v_2) of identified hadrons as a function of the beam energy ($\mathrm{E_{Lab}}$). As a quadrangular flow, v_4 is believed to be originated from v_2 and 4^{th} order moment of the fluid flow, the ratio $v_4/(v_2)^2$ was examined for a wide range of beam energies and different EoS. The ratio is consistently below 2 for all four cases of EoS and can be tested against the data from the future experiments at NICA [28] and FAIR [29, 30].

In addition, we have studied NCQ scaling in terms of the coalescence sum rule for the slope of the directed flow of $\bar{\Lambda}$ and net Λ. For this purpose, we used different calculations used in Ref. [135] and compared them with dv_1/dy of $\bar{\Lambda}$ and net Λ. Results qualitatively match the expectations for all four variants of UrQMD. This study may also hint towards the possible onset of deconfinement at certain beam energy above 25A GeV. Furthermore, it was interesting to notice similar results, even for pure transport and hadrons gas EoS cases where quarks and gluons are not underlying degrees of freedom.

At this point, it appears from the results of collective flow excitation functions that neither of the EoS is suitable enough to reproduce the experimental measurements quantitatively. Moreover, the nature of the matter might be partonic; however, it does not evolve as a non-viscous ideal fluid as implemented in the present version of the model. Furthermore, higher values of calculated flow coefficients corresponding to data suggest a larger pressure gradient in an ideal hydrodynamic scenario. Therefore, one possibility would be to use viscous hydrodynamics instead of the ideal one to account for dissipative effects. Other reasons for the disagreement might be the inapplicability of hydrodynamics at low beam energies where the transport approach seems to give the better agreement and the fact that reaction plane angle, which leads to event-by-event fluctuations, is not taken into account in UrQMD.

Various particle ratios are calculated for all EoS and studied as a function of beam energy. The ratios were sensitive to first-order phase transition and exhibited different behavior than other cases. UrQMD, including fluid dynamic simulations with Hadron Gas and Chiral EoS, can qualitatively explain the strange to non-strange ratio and overestimate the measurements. However, the calculated strange to non-strange ratio showed some interesting features in response to various EoS beyond 25A GeV. Similarly, particle to anti-particle ratios is qualitatively described by hybrid mode with underestimation to the data except for π^+ to π^- ratio, which is nicely explained. Moreover, the measured ratio of proton to π^+ is also well described by the predictions. However, the calculated $\bar{p}$ to π^- ratio underestimates the data.

Then we study the rapidity spectra of net-protons for different EoS at various beam energies. The shape of these spectra at mid-rapidity, quantified as a reduced curvature, is seen to be sensitive to underlying EoS and shows a larger value in the case of Bag Model EoS beyond 25A GeV. It also revealed the sensitivity to the underlying degrees of freedom beyond 25A GeV.

Continuing the previous study, we have investigated different observables in non-central Au + Au collisions in beam energy range 1A-158A GeV for various particlization modes in combination with different EoS. We have employed above mentioned three EoS, with particlization models such as gradual (GF), isochronous (ICF), and iso-energy density (IEF) particlization scenarios. We started with an anisotropic flow coefficient study for various particlization models coupled to various EoS. We observed that irrespective of any EoS, IEF particlization scenario provides a compelling and qualitative description of the experimental measurements in contrast with the other two scenarios. In particular, experimental measurements of the elliptic flow of protons and pions were explained well using the IEF scenario at beam energies above around 20A

GeV. We also observed that directed flow using the IEF scenario has no "wiggle" structure compared to the other two cases. The slope of the directed flow was examined as a function of beam energies for various particlization modes and EoS, and it was seen that the IEF scenario is useful in reproducing the trend of the experimental data qualitatively. Moreover, while investigating the elliptic flow (v_2), we found that similar to v_1 analysis, the IEF scenario suits the data better at higher beam energies. We also note that excitation of v_2 obtained using the bag model shows non-monotonous behavior irrespective of the opted particlization scenario.

Then, we investigated the effect of particlization models on particle production by estimating the particle ratios as the choice of particlization mode can alter the particle chemistry of the system. We have observed that IEF and ICF scenarios for all EoS cases qualitatively describe the strange to non-strange ratio. Moreover, in the case of the particle to anti-particle and baryon-to-meson ratios, the IEF scenario describes the data reasonably well compared to the other two scenarios. Surprisingly, we observed negligible anti-proton production at high beam energies for the ICF scenario. Although, more studies in this direction could be helpful.

We investigated the reduced curvature of net-protons, which quantifies the shape of rapidity at mid-rapidity as a function of beam energy. The reduced curvature obtained for the IEF scenario gives consistent results with experimental measurement, even at high beam energies. The results here are essential and would be helpful once more precise data become available in the near future from the upcoming accelerator facilities.

From this investigation, the particlization model-dependent study has clarified the suitability of the EoS in the UrQMD model to examine various experimental observables. We have seen that the choice IEF particlization scenario should be more useful as it provides compelling agreement with experimental results without being too sensitive to the underlying EoS. However, if one were to choose among the EoS, then both hadron gas and chiral EoS with the IEF scenario would make a good choice for a more realistic combination. Examining other various observables using these combinations would be helpful to make any further distinctions.

Finally, we would like to draw the conclusion that these investigations are essential for the better development of the CBM experiment. However, there is still more to be done before the CBM experiment can deliver. This thesis represents the contributions we made from our end, and more will be investigated in the future. The phenomenological research conducted for this thesis is essential in selecting the appropriate set of variables to employ with the UrQMD event generator for any future research, and it will be even more helpful once the CBM experimental results are available.

Bibliography

[1] Aoki Y., Endrodi G., Fodor Z., Katz S. D., Szabo K. K. (2006), The Order of the quantum chromodynamics transition predicted by the standard model of particle physics, Nature, 443, 675-678 (DOI: 10.1038/nature05120) iii, 5

[2] Friman B., Höhne C., Knoll J., Leupold S., Randrup J., Rapp R., Senger P. (2011) The CBM Physics Book, Springer Berlin, Heidelberg, Lect. Notes Phys., 814, 1-980 (DOI: 10.1007/978-3-642-13293-3) iv

[3] Chattopadhyay S. *et al* (2015) (Eds.), Technical Design Report for the CBM : Muon Chambers (MuCh), GSI-2015-02580, https://repository.gsi.de/record/161297. iv, xviii, 27, 28, 29, 32, 37

[4] Kundu S. K., Roy A. *et al* (2023), Development of a water-based cooling system for the Muon Chamber detector system of the CBM experiment, Nuclear Inst. and Methods in Physics Research, A 1050, 168143 (DOI: 10.1016/j.nima.2023.168143) v

[5] Kundu S. K., Bailung Y., Rode S. P., Bhaduri P. P., Roy A. (2021), Dependence on beam energy and nuclear equation of state of anisotropic flow and particle production in low-energy heavy-ion collisions, Phys. Rev. C, 104, 024907 (DOI:10.1103/PhysRevC.104.024907) vii, 90

[6] Bass S. A. *et al* (1998), Microscopic models for ultrarelativistic heavy ion collisions, Prog. Part. Nucl. Phys., 41, 255-369 (DOI:10.1016/S0146-6410(98)00058-1) vii, 11, 68

[7] Kundu S. K., Bailung Y., Rode S. P., Bhaduri P. P., Roy A. (2023), Effect of various particlization scenarios on anisotropic flow and parti-

cle production using UrQMD hybrid model, Nucl. Phys. A, 1030, 122574 (DOI:10.1016/j.nuclphysa.2022.122574) viii

[8] http://www.signaltonoisemag.com/allarticles/2017/5/3/the-standard-model-high-school xvii, 2

[9] Chatrchyan S. *et al* (CMS Collaboration) (2012), Observation of a New Boson at a Mass of 125 GeV with the CMS Experiment at the LHC, Phys. Lett. B, 716, 30-61 (DOI:10.1016/j.physletb.2012.08.021) 2

[10] Aad G. *et al* (ATLAS Collaboration) (2012), Observation of a new particle in the search for the Standard Model Higgs boson with the ATLAS detector at the LHC, Phys. Lett. B, 716 1-29 (DOI:10.1016/j.physletb.2012.08.020) 2

[11] Fritzsch H., Gell-Mann M.,Leutwyler H. (1973), Advantages of the Color Octet Gluon Picture, Phys. Lett. B, 47, 365-368 (DOI: 10.1016/0370-2693(73)90625-4) 2

[12] Nambu Y. (1960), Axial vector current conservation in weak interactions, Phys. Rev. Lett., 4, 380-382 (DOI: 10.1103/PhysRevLett.4.380) 2

[13] Greenberg O. W. (1964), Spin and Unitary Spin Independence in a Paraquark Model of Baryons and Mesons, Phys. Rev. Lett., 13, 598-602 (DOI: 10.1103/PhysRevLett.13.598) 2

[14] Workman R. L. *et al* (Particle Data Group) (2022), Review of Particle Physics, Prog. Theor. Exp. Phys., 2022, 083C01 (DOI: 10.1093/ptep/ptac097) xvii, 3

[15] Sahu P. K., Phatak S. C., Viyogi Y. P. (2009), Quark gluon plasma and Hadron physics, Narosa Pub. House, New Delhi, 316836387 4

[16] Gross D. J., Wilczek F. (1973), Ultraviolet Behavior of Non-Abelian Gauge Theories, Phys. Rev. Lett., 30, 1343 (10.1103/PhysRevLett.30.1343) 4

[17] Politzer H. D. (1973), Reliable Perturbative Results for Strong Interactions?, Phys. Rev. Lett., 30, 1346 (DOI: 10.1103/PhysRevLett.30.1346) 4

[18] Aarts G., Attanasio F., Jager B., Seiler E., Sexty D., Stamatescu I. O. (2016), QCD at nonzero chemical potential: recent progress on the lattice, AIP Conference Proceedings, 1701, 020001 (DOI: 10.1063/1.4938590) xvii, 4

[19] Borsanyi S. *et al* [Wuppertal-Budapest] (2010), Is there still any T_c mystery in lattice QCD? Results with physical masses in the continuum limit III, JHEP 09, 073 (DOI: 10.1007/JHEP09(2010)073) 5

[20] Bazavov A. *et al* (2012), The chiral and deconfinement aspects of the QCD transition, Phys. Rev. D, 85, 054503 (DOI: 10.1103/PhysRevD.85.054503) 5

[21] Fodor Z., Katz S. D. (2004), Critical point of QCD at finite T and μ, lattice results for physical quark masses, JHEP, 04, 050 (DOI: 10.1088/1126-6708/2004/04/050) 5

[22] Letessier J., Rafelski J. (2023), A new phase of matter? In Hadrons and Quark–Gluon Plasma (Cambridge Monographs on Particle Physics, Nuclear Physics and Cosmology, p. 1), Cambridge: Cambridge University Press. (DOI: 10.1017/9781009290753.002) 6

[23] Bjorken J. D. (1983), Highly relativistic nucleus-nucleus collisions: The central rapidity region, Phys. Rev. D, 27, 140 (DOI: 10.1103/PhysRevD.27.140) 6

[24] Shuryak E. V. (1978), Quark-Gluon Plasma and Hadronic Production of Leptons, Photons and Psions, Phys. Lett. B, 78, 150 (DOI: 10.1016/0370-2693(78)90370-2) 6

[25] Braun-Munzinger P., Dönigus B. (2019), Loosely-bound objects produced in nuclear collisions at the LHC, Nucl. Phys. A, 987, 144-201 (DOI: 10.1016/j.nuclphysa.2019.02.006) xvii, 7

[26] Adams J. *et al* (STAR Collaboration) (2005), Event by event $< p_t >$ fluctuations in Au - Au collisions at $\sqrt{s_{NN}}$ = 130 GeV, Phys. Rev. C, 71, 064906 (DOI: 10.1103/PhysRevC.71.064906) 7, 10

[27] Appelshäuser H. *et al* (NA49 Collaboration) (1999), Event-by-event fluctuations of average transverse momentum in central Pb + Pb collisions at 158 GeV per nucleon, Phys. Lett. B, 459, 679-686 (DOI: 10.1016/S0370-2693(99)00673-5) 7

[28] Kekelidze V., Kovalenko A., Lednicky R., Matveev V., Meshkov I., Sorin A., Trubnikov G. (2016), Prospects for the dense baryonic matter research at NICA, Nucl. Phys. A, 956, 846-849 (DOI: 10.1016/j.nuclphysa.2016.03.019) 8, 103

[29] Ablyazimov T. *et al* (CBM Collaboration) (2017), Challenges in QCD matter physics –The scientific programme of the Compressed Baryonic Matter experiment at FAIR, Eur. Phys. J. A, 53, 60 (DOI: 10.1140/epja/i2017-12248-y) 8, 103

[30] Sturm C., Sharkov B., Stöcker H. (2010), 1, 2, 3 . . . FAIR !, Nucl. Phys. A, 834, 682c-687c (DOI: 10.1016/j.nuclphysa.2010.01.124) 8, 103

[31] Schmah A. (STAR Collaboration) (2012), Highlights of the Beam Energy Scan from STAR, Central Eur. J. Phys., 10, 1238-1241 (DOI: 10.2478/s11534-012-0149-1) 8

[32] Chatterjee R., Srivastava D. K. (2009), Elliptic flow of thermal photons and formation time of quark gluon plasma at energies available at the BNL Relativistic Heavy Ion Collider (RHIC), Phys. Rev. C, 79, 021901 (DOI: 10.1103/PhysRevC.79.021901) 9

[33] Bass S. A., Muller B., Srivastava D. K. (2004), Photon Interferometry of Au+Au Collisions at the BNL Relativistic Heavy-Ion Collider, Phys. Rev. Lett. 93, 162301 (DOI: 10.1103/PhysRevLett.93.162301) 9

[34] Bass S. A., Muller B., Srivastava D. K. (2003), Light from Cascading Partons in Relativistic Heavy-Ion Collisions, Phys. Rev. Lett., 90, 082301 (DOI: 10.1103/PhysRevLett.90.082301) 9

[35] Renk T., Bass S. A., Srivastava D. K. (2006), Dynamics of the Landau–Pomeranchuk–Migdal effect in Au + Au collisions at $\sqrt{s} = 200A$ GeV, Phys. Lett. B, 632, 632 (DOI: 10.1016/j.physletb.2005.11.026) 9

[36] Chatterjee R., Frodermann E. S., Heinz U. W., Srivastava D. K. (2006), Elliptic Flow of Thermal Photons in Relativistic Nuclear Collisions, Phys. Rev. Lett., 96, 202302 (DOI: 10.1103/PhysRevLett.96.202302) 9

[37] Heinz U. W., Chatterjee R., Frodermann E. S., Gale C., Srivastava D. K. (2007), Elliptic Flow of Thermal Photons/Dileptons, Nucl. Phys. A, 783, 379 (DOI: 10.1016/j.nuclphysa.2006.11.090) 9

[38] Mohanty P., Alam J. e., B. Mohanty (2011), Evolution of collectivity as a signal of quark gluon plasma formation in heavy ion collisions, Phys. Rev. C, 84, 024903 (DOI: 10.1103/PhysRevC.84.024903) 9

[39] Matsui T., Satz H. (1986), J/ψ Suppression by Quark-Gluon Plasma Formation, Phys. Lett. B, 178, 416 (DOI: 10.1016/0370-2693(86)91404-8) 10

[40] Jeon S., Koch V. (1999), Fluctuations of Particle Ratios and the Abundance of Hadronic Resonances, Phys. Rev. Lett., 83, 5435 (DOI: 10.1103/PhysRevLett.83.5435) 10

[41] Jeon S., Koch V. (2000), Charged Particle Ratio Fluctuation as a Signal for Quark-Gluon Plasma, Phys. Rev. Lett., 85, 2076 (DOI: 10.1103/PhysRevLett.85.2076) 10

[42] Gavin S., Pruneau C. (2000), Covariance of antiproton yield and source size in nuclear collisions, Phys. Rev. C, 61, 044901 (DOI: 10.1103/PhysRevC.61.044901) 10

[43] Adams J. *et al* (STAR Collaboration) (2003), Net charge fluctuations in Au+Au collisions at $\sqrt{s}$ = 130 GeV, Phys. Rev. C, 68, 044905 (DOI: 10.1103/PhysRevC.68.044905) 10

[44] Nouicer R. (2016), New State of Nuclear Matter: Nearly Perfect Fluid of Quarks and Gluons in Heavy Ion Collisions at RHIC Energies, Eur. Phys. J. Plus, 131, 70 (DOI: 10.1140/epjp/i2016-16070-20) xvii, 10

[45] Poskanzer A. M., Voloshin S. A. (1998), Methods for analyzing anisotropic flow in relativistic nuclear collisions, Phys. Rev. C, 58, 1671-1678 (DOI: 10.1103/PhysRevC.58.1671) 10

[46] Alver B. *et al* (PHOBOS Collaboration) (2007), System size, energy, pseudorapidity, and centrality dependence of elliptic flow, Phys. Rev. Lett., 98, 242302 (DOI: 10.1103/PhysRevLett.98.242302) 11

[47] Aamodt K. *et al* (ALICE Collaboration) (2010), Elliptic flow of charged particles in Pb-Pb collisions at 2.76 TeV, Phys. Rev. Lett., 105, 252302 (DOI: 10.1103/PhysRevLett.105.252302) 11

[48] Bhaduri P. P., Chattopadhyay S. (2010), Differential elliptic flow of identified hadrons and constituent quark number scaling at FAIR, Phys. Rev. C, 81, 034906 (DOI: 10.1103/PhysRevC.81.034906) 11, 80

[49] Sarkar S., Mali P., Mukhopadhyay A. (2017), Simulation study of elliptic flow of charged hadrons produced in Au + Au collisions at energies available at the Facility for Antiproton and Ion Research, Phys. Rev. C, 95, 014908 (DOI: 10.1103/PhysRevC.95.014908) 11

[50] Auvinen J., Petersen H. (2013), Evolution of elliptic and triangular flow as a function of $\sqrt{s_{NN}}$ in a hybrid model, Phys. Rev. C, 88, 064908 (DOI: 10.1103/PhysRevC.88.064908) 11, 71

[51] Bleicher M. *et al* (1999), Relativistic hadron hadron collisions in the ultrarelativistic quantum molecular dynamics model, J. Phys. G, 25, 1859-1896 (DOI: 10.1088/0954-3899/25/9/308) 11, 68, 81

[52] Lin Z. W., Ko C. M., Li B. A., Zhang B., Pal S. (2005), A Multi-phase transport model for relativistic heavy ion collisions, Phys. Rev. C, 72, 064901 (DOI: 10.1103/PhysRevC.72.064901) 11

[53] Chen L. W., Greco V., Ko C. M., Kolb P. F. (2005), Pseudorapidity dependence of anisotropic flows in relativistic heavy-ion collisions, Phys. Lett. B, 605, 95-100 (DOI: 10.1016/j.physletb.2004.11.017) 11

[54] Le Fèvre A., Leifels Y., Hartnack C., Aichelin J. (2018), Origin of elliptic flow and its dependence on the equation of state in heavy ion reactions at intermediate energies, Phys. Rev. C, 98, 034901 (DOI: 10.1103/PhysRevC.98.034901) 12

[55] Pinkenburg C. *et al* [E895] (1999), Elliptic flow: Transition from out-of-plane to in-plane emission in Au + Au collisions, Phys. Rev. Lett., 83, 1295-1298 (DOI: 10.1103/PhysRevLett.83.1295) xx, xxiii, 12, 76, 77, 91, 92

[56] Aamodt K. *et al* (ALICE Collaboration) (2011), Higher Harmonic Anisotropic Flow Measurements of Charged Particles in Pb-Pb Collisions at $\sqrt{s_{NN}}$ = 2.76 TeV, Phys. Rev. Lett., 107, 032301 (DOI: 10.1103/PhysRevLett.107.032301) 13

[57] Aad G. *et al* (ATLAS Collaboration) (2012), Measurement of the azimuthal anisotropy for charged particle production in $\sqrt{s_{NN}} = 2.76$ TeV lead-lead collisions with the ATLAS detector, Phys. Rev. C, 86, 014907 (DOI: 10.1103/PhysRevC.86.014907) 13

[58] Chatrchyan S. *et al* (CMS Collaboration) (2014), Measurement of higher-order harmonic azimuthal anisotropy in PbPb collisions at $\sqrt{s_{NN}} = 2.76$ TeV, Phys. Rev. C, 89, 044906 (DOI: 10.1103/PhysRevC.89.044906) 13

[59] Adams J. *et al* (STAR Collaboration) (2005), Experimental and theoretical challenges in the search for the quark–gluon plasma: The STAR Collaboration's critical assessment of the evidence from RHIC collisions, Nucl. Phys. A, 757, 102 (DOI: 10.1016/j.nuclphysa.2005.03.085) 13

[60] Adcox K. *et al* (PHENIX Collaboration) (2005), Formation of dense partonic matter in relativistic nucleus–nucleus collisions at RHIC: Experimental evaluation by the PHENIX Collaboration, Nucl. Phys. A, 757, 184 (DOI: 10.1016/j.nuclphysa.2005.03.086) 13

[61] Agakishiev G. *et al* [HADES] (2009), The High-Acceptance Dielectron Spectrometer HADES, Eur. Phys. J. A, 41, 243-277 (DOI: 10.1140/epja/i2009-10807-5) 13

[62] Sturm C. T. *et al* [KAOS] (2001), Evidence for a soft nuclear equation of state from kaon production in heavy ion collisions, Phys. Rev. Lett., 86, 39-42, (DOI: 10.1103/PhysRevLett.86.39) 13

[63] Rai G. *et al* [E895] (1999), Results from the experiment E895 at the BNL AGS, Nucl. Phys. A, 661, 162-169 (DOI: 10.1016/S0375-9474(99)85018-0) 13

[64] Ahle L. *et al* [E866 and E917] (2000), Excitation function of K+ and pi+ production in Au + Au reactions at 2A GeV to 10A GeV, Phys. Lett. B, 476, 1-8 (DOI: 10.1016/S0370-2693(00)00037-X) xxi, xxiii, 13, 82, 92

[65] Afanasiev S. *et al* [NA49] (1999), The NA49 large acceptance hadron detector, Nucl. Instrum. Meth. A, 430, 210-244 (DOI: 10.1016/S0168-9002(99)00239-9) 14

[66] The FAIR experiment, https://fair-center.eu/ . xvii, 18

[67] UNILAC acceleartor, https://www.gsi.de/en/work /beschleunigerbetrieb/beschleuniger/unilac/unilac . xvii, 19

[68] p-LINAC, https://www.gsi.de/en/work/beschleunigerbetrieb/beschleuniger/ionenquellen/projects/p_linac . xvii, 19

[69] Heavy-ion synchrotron SIS18 with sections, https://www.gsi.de/en/work/accelerator_operations/accelerators/heavy_ion_synchrotron_sis18/sis18_sections. xvii, 21

[70] Malakhov A., Shabunov A (Eds) (2013), Technical Design Report for the CBM Superconducting Dipole Magnet, GSI-2015-02000, https://repository.gsi.de/record/109025 24

[71] Kurilkin P., *et al* (2017), Superconducting dipole magnet for the CBM experiment at FAIR, EPJ Web Conf., 138, 12001 (DOI: 10.1051/epj-conf/201713812001) xvii, 24

[72] Klaus P., *et al* (Eds) (2022), Technical Design Report for the CBM: Micro Vertex Detector (MVD), GSI-2022-00549, https://repository.gsi.de/record/246516 25

[73] Heuser J., *et al* (Eds) (2013), Technical Design Report for the CBM Silicon Tracking System (STS), GSI-2013-05499, https://repository.gsi.de/record/54798 26

[74] Montgomery R. A. *et al* (2015), Investigation of Hamamatsu H8500 phototubes as single photon detectors, Nucl. Instrum. Meth. A, 790, 28-41 (DOI: 10.1016/j.nima.2015.03.068) 26

[75] Höhne C. (Ed) (2013), Technical Design Report for the CBM Ring Imaging Cherenkov Detector, GSI-2014-00528, https://repository.gsi.de/record/65526 26

[76] Sauli F. *et al* (1997), GEM: A new concept for electron amplification in gas detectors, Nucl. Inst. and Meth. A, 386, 531 (DOI: 10.1016/S0168-9002(96)01172-2) 30

[77] Alfonsi M. *et al* (2007), Status of triple GEM muon chambers for the LHCb experiment, Nucl. Inst. and Meth. A, 581, 283 (DOI: 10.1016/j.nima.2007.07.123) 30

[78] Villa M. *et al* (2011), Progress on large area GEMs, Nucl. Inst. and Meth. A, 628, 182-186 (DOI: 10.1016/j.nima.2010.06.312) 31

[79] Altunbas C. *et al* (2002), Construction, test and commissioning of the triple-GEM tracking detector for COMPASS, Nucl. Inst. and Meth. A, 490, 117-203 (DOI: 10.1016/S0168-9002(02)00910-5) 33

[80] Kozlov A. *et al* (2004), Development of a triple GEM UV photon detector operated in pure CF(4) for the PHENIX experiment, Nucl. Inst. and Meth. A, 523, 345-354 (DOI: 10.1016/j.nima.2003.12.018) 33

[81] CBM Collaboration (2018), Technical Design Report for the CBM Transition Radiation Detector (TRD), GSI-2018-01091, https://repository.gsi.de/record/217478 34

[82] Herrmann N. (Ed) (2014), Technical Design Report for the CBM Time-of-Flight System (TOF), GSI-2015-01999, https://repository.gsi.de/record/109024 34

[83] Korolko I. E., Prokudin M. S., Zaitsev Y. M. (2017), The CBM ECAL, J. Phys. Conf. Ser., 798, 012164 (DOI: 10.1088/1742-6596/798/1/012164) 35

[84] Guber F., Selyuzhenkov I. (Eds) (2015), Technical Design Report for the CBM Projectile Spectator Detector (PSD), GSI-2015-02020, https://repository.gsi.de/record/109059 36

[85] Patra R. N. *et al* (2017), Measurement of basic characteristics and gain uniformity of a triple GEM detector, Nucl. Instrum. Meth. A, 862, 25 (DOI: 10.1016/j.nima.2017.05.011) 38

[86] Roy S. *et al* (2019), Stability study of gain and energy resolution for GEM detector, Nucl. Instrum. Meth. A, 936, 485 (DOI: 10.1016/j.nima.2018.10.060) 38

[87] Texas Instruments, LM35 Precision Centigrade Temperature Sensors datasheet, *http://www.ti.com/lit/ds/symlink/lm35.pdf*. 39

[88] Atmel, ATmega328/P Micro-controller datasheet, *https://cdn.sparkfun.com/assets/c/a/8/e/4/Atmel-42735-8-bit-AVR-Microcontroller-ATmega328-328P_Datasheet.pdf*. 39, 45

[89] Jain V. *et al* (2015), Design of a water based cooling system to take out electronics heat load of MUCH detector in CBM experiment, Proceeding of DAE-BRNS Symp. Nucl. Phys., 60, 1022-1023 40

[90] Nag D. *et al* (2016), Design and fabrication of a water based cooling system for the CBM Muon Chamber, Proceeding of DAE-BRNS Symp. Nucl. Phys., 61, 1096-1097 40

[91] Ghosh C. *et al* (2017), Development of a controlled and monitored water cooling system for CBM-MUCH Detector, Proceeding of DAE-BRNS Symp. Nucl. Phys., 62, 1062-1063 46

[92] Nag D. *et al* (2018), Design and Fabrication of a Controlled Water Based Cooling System for CBM Muon Chamber, Proceeding of Springer Proc. Phys., 203, 893-895 46

[93] Kumar A. *et al* (2021), Testing Real-Size Triple GEM Chambers with Pb+Pb Collision at CERN SPS, Proceedings in Physics, Springer, Singapore, 261, 711-718 (DOI: 10.1007/978-981-33-4408-2_98) 46

[94] Kundu S. K. *et al* (2020), Performance study of the first two stations of CBM MuCh cooling system, CBM Progress Report 2019, 102-103 (DOI: 10.15120/GSI-2020-00904) 48

[95] Kundu S. K. *et al* (2021), Feasibility study of water distribution for the CBM MuCh cooling system, Proceeding of DAE-BRNS Symp. Nucl. Phys., 323, 790-791 48

[96] FESTO, Push-in fittings QS, standard, *https://www.festo.com/media/pim/987/D15000100122987.PDF*. 49

[97] FESTO, Plastic tubing, standard O.D., *https://www.festo.com/cat/en-gb_gb/data/doc_ENGB/PDF/EN/OD-TUBING_EN.PDF*. 49

[98] YF-S201 Water Flow Sensor, *http://www.mantech.co.za/datasheets/products/yf-s201_sea.pdf*. 50

[99] https://git.cbm.gsi.de/computing/cbmroot 53

[100] Brun R., Rademakers F. (1997), ROOT: An object oriented data analysis framework, Nucl. Instrum. Meth. A, 389, 81–86 (DOI: 10.1016/S0168-9002(97)00048-X) 53

[101] Brun R. *et al* (1987), GEANT3, CERN-DD-EE-84-1 53

[102] Agostinelli S. *et al* (GEANT4 Collaboration) (2003), GEANT4: A simulation toolkit, Nucl. Instrum. Meth. A, 506, 250–303 (DOI: 10.1016/S0168-9002(03)01368-8) 53

[103] Battistoni G. *et al* (2007), The FLUKA code: description and benchmarking, AIP Conf. Proc., 896, 31–49 (DOI: 10.1063/1.2720455) 53

[104] Smirnov I. B. (1996), HEED version 1.01, Detailed Simulation of the Initial Ionization in Gases, CERN Computer Newsletter No. 226, p.13 57

[105] Senger A. (2020), Simultaneous muon and reference hadron measurements in the Compressed Baryonic Matter experiment at FAIR, Int. J. Mod. Phys. E, 29, 2030003 (DOI: 10.1142/S0218301320300039) 62

[106] https://git.cbm.gsi.de/pwg-c2f/analysis/pid/ 62

[107] Baznat M., Botvina A., Musulmanbekov G. *et al* (2020), Monte-Carlo Generator of Heavy Ion Collisions DCM-SMM, Phys. Part. Nuclei Lett., 17, 303–324 (DOI: 10.1134/S1547477120030024) 63

[108] Petersen H., Steinheimer J., Burau G., Bleicher M., Stöcker H. (2008), A Fully Integrated Transport Approach to Heavy Ion Reactions with an Intermediate Hydrodynamic Stage, Phys. Rev. C, 78, 044901 (DOI: 10.1103/PhysRevC.78.044901) 68, 69

[109] Rischke D. H., Bernard S., Maruhn J. A. (1995), Relativistic hydrodynamics for heavy ion collisions. 1. General aspects and expansion into vacuum, Nucl. Phys. A, 595, 346-382 (DOI: 10.1016/0375-9474(95)00355-1) 68

[110] Rischke D. H., Pursun Y., Maruhn J. A. (1996), Relativistic hydrodynamics for heavy ion collisions. 2. Compression of nuclear matter and the phase transition to the quark - gluon plasma, Nucl. Phys. A, 595, 383-408 (DOI: 10.1016/0375-9474(95)00356-3) [erratum: Nucl. Phys. A, 596, 717-717 (1996)]. 68, 69

[111] Zschiesche D., Schramm S., Schaffner-Bielich J., Stoecker H., Greiner W. (2002), Particle ratios at RHIC: Effective hadron masses and chemical freeze-out, Phys. Lett. B, 547, 7-14 (DOI: 10.1016/S0370-2693(02)02736-3) 69

[112] Steinheimer J., Schramm S., Stöcker H. (2011), The hadronic SU(3) Parity Doublet Model for Dense Matter, its extension to quarks and the strange equation of state, Phys. Rev. C, 84, 045208 (DOI: 10.1103/PhysRevC.84.045208) 69

[113] Huovinen P., Petersen H. (2012), Particlization in hybrid models, Eur. Phys. J. A, 48, 171 (DOI: 10.1140/epja/i2012-12171-9) 70, 87, 88

[114] Adare A. *et al* [PHENIX] (2016), Transverse energy production and charged-particle multiplicity at midrapidity in various systems from $\sqrt{s_{NN}} = 7.7$ to 200 GeV, Phys. Rev. C, 93, 024901 (DOI: 10.1103/PhysRevC.93.024901) 70

[115] Petersen H., Li Q., Zhu X., Bleicher M. (2006), Directed and elliptic flow in heavy ion collisions at GSI-FAIR and CERN-SPS, Phys. Rev. C, 74, 064908 (DOI: 10.1103/PhysRevC.74.064908) 71, 72

[116] Petersen H., Bleicher M. (2009), Ideal hydrodynamics and elliptic flow at SPS energies: Importance of the initial conditions, Phys. Rev. C., 79, 054904 (DOI: 10.1103/PhysRevC.79.054904) 71

[117] Steinheimer J., Auvinen J., Petersen H., Bleicher M., Stöcker H. (2014), Examination of directed flow as a signal for a phase transition in relativistic nuclear collisions, Phys. Rev. C, 89, 054913 (DOI: 10.1103/PhysRevC.89.054913) 71, 76, 88

[118] Rode S. P., Bhaduri P. P., Roy A. (2019), Anisotropic flow of charged and identified hadrons at FAIR energies and its dependence on the nuclear equation of state, Eur. Phys. J. A, 55, 216 (DOI: 10.1140/epja/i2019-12921-1) 71, 75, 77

[119] Li Q. f., Steinheimer J., Petersen H., Bleicher M., Stöcker H. (2009), Effects of a phase transition on HBT correlations in an integrated Boltzmann+Hydrodynamics approach, Phys. Lett. B, 674, 111-116 (DOI: 10.1016/j.physletb.2009.03.012) 87

[120] Petersen H., Steinheimer J., Bleicher M., Stöcker H. (2009), $< m_T >$ excitation function: Freeze-out and equation of state dependence, J. Phys. G, 36, 055104 (DOI: 10.1088/0954-3899/36/5/055104) 87

[121] Alt C. *et al* (NA49 Collaboration) (2003), Directed and elliptic flow of charged pions and protons in Pb + Pb collisions at 40-A-GeV and 158-A-GeV, Phys. Rev. C, 68, 034903 (DOI: 10.1103/PhysRevC.68.034903) xx, xxii, xxiii, 72, 74, 75, 76, 77, 89, 90, 91, 92

[122] Liu H. *et al* [E895] (2000), Sideward flow in Au + Au collisions between 2A GeV and 8A GeV, Phys. Rev. Lett., 84, 5488-5492 (DOI: 10.1103/PhysRevLett.84.5488) xx, xxii, 75, 76, 90, 91

[123] Adamczyk L. *et al* (STAR Collaboration) (2014), Beam-Energy Dependence of the Directed Flow of Protons, Antiprotons, and Pions in Au+Au Collisions, Phys. Rev. Lett., 112, 162301 (DOI: 10.1103/PhysRevLett.112.162301) xx, xxii, 75, 76, 90, 91

[124] Snellings R. J. M., Sorge H., Voloshin S. A., Wang F. Q., Xu N. (2000), Novel rapidity dependence of directed flow in high-energy heavy ion collisions, Phys. Rev. Lett., 84, 2803-2805 (DOI: 10.1103/PhysRevLett.84.2803) 90

[125] Borghini N., Ollitrault J. Y. (2021), Momentum spectra, anisotropic flow, and ideal fluids, Phys. Lett. B, 642, 227-231 (DOI: 10.1016/j.physletb.2006.09.062) 77

[126] Gombeaud C., Ollitrault J. Y. (2010), Effects of flow fluctuations and partial thermalization on v_4, Phys. Rev. C, 81, 014901 (DOI: 10.1103/PhysRevC.81.014901) 77

[127] Luzum M., Gombeaud C., Ollitrault J. Y. (2010), v_4 in ideal and viscous hydrodynamics simulations of nuclear collisions at the BNL Relativistic Heavy Ion Collider (RHIC) and the CERN Large Hadron Collider (LHC), Phys. Rev. C, 81, 054910 (DOI: 10.1103/PhysRevC.81.054910) 77

[128] Konchakovski V. P., Bratkovskaya E. L., Cassing W., Toneev V. D., Voloshin S. A., Voronyuk V. (2012), Azimuthal anisotropies for Au+Au collisions in the parton-hadron transient energy range, Phys. Rev. C, 85, 044922 (DOI: 10.1103/PhysRevC.85.044922) 78

[129] Nara Y., Steinheimer J., Stoecker H. (2018), The enhancement of v_4 in nuclear collisions at the highest densities signals a first-order phase transition, Eur. Phys. J. A, 54, 188 (DOI: 10.1140/epja/i2018-12626-y) 78

[130] Adams J. *et al* (STAR Collaboration) (2004), Azimuthal anisotropy at RHIC: The First and fourth harmonics, Phys. Rev. Lett., 92, 062301 (DOI: 10.1103/PhysRevLett.92.062301) 78

[131] Masui H. [PHENIX] (2006), Anisotropic flow in $\sqrt{s_{NN}}$ = 200 GeV Cu+Cu and Au+Au collisions at PHENIX, Nucl. Phys. A, 774, 511-514 (DOI: 10.1016/j.nuclphysa.2006.06.077) 78

[132] Abelev B. I. *et al* (STAR Collaboration) (2007), Mass, quark-number, and $\sqrt{s_{NN}}$ dependence of the second and fourth flow harmonics in ultra-relativistic nucleus-nucleus collisions, Phys. Rev. C, 75, 054906 (DOI: 10.1103/PhysRevC.75.054906) 78

[133] Huang S. [PHENIX] (2008), Measurements of high p_T identified particles v_2 and v_4 in $\sqrt{s_{NN}}$ = 200 GeV Au+Au collisions by PHENIX, J. Phys. G, 35, 104105 (DOI: 10.1088/0954-3899/35/10/104105) 78

[134] Bhalerao R. S., Blaizot J. P., Borghini N., Ollitrault J. Y. (2005), Elliptic flow and incomplete equilibration at RHIC, Phys. Lett. B, 627, 49-54 (DOI: 10.1016/j.physletb.2005.08.131) 78

[135] Adamczyk L. *et al* (STAR Collaboration) (2018), Beam-Energy Dependence of Directed Flow of Λ, $\bar{\Lambda}$, $K^{\pm}$, K_s^0 and ϕ in Au+Au Collisions, Phys. Rev. Lett., 120, 062301 (DOI: 10.1103/PhysRevLett.120.062301) xxi, 79, 80, 103

[136] Dunlop J. C., Lisa M. A., Sorensen P. (2011), Constituent quark scaling violation due to baryon number transport, Phys. Rev. C, 84, 044914 (DOI: 10.1103/PhysRevC.84.044914) 79

[137] Guo Y., Liu F., Tang A. (2012), Directed flow of transported and non-transported protons in Au+Au collisions from UrQMD model, Phys. Rev. C, 86, 044901 (DOI: 10.1103/PhysRevC.86.044901) 81

[138] Alt C. *et al* (NA49 Collaboration) (2008), Pion and kaon production in central Pb + Pb collisions at 20A and 30A GeV: Evidence for the onset of deconfinement, Phys. Rev. C, 77, 024903 (DOI: 10.1103/PhysRevC.77.024903) 76, 81, 96

[139] Alt C. *et al* (NA49 Collaboration) (2006), Energy and centrality dependence of anti-p and p production and the anti-Lambda/anti-p ratio in Pb+Pb collisions between 20A GeV and 158A GeV, Phys. Rev. C, 73, 044910 (DOI: 10.1103/PhysRevC.73.044910) xxi, xxiii, 81, 82, 83, 92, 93, 96

[140] Adamczyk L. *et al* (STAR Collaboration) (2017), Bulk Properties of the Medium Produced in Relativistic Heavy-Ion Collisions from the Beam Energy Scan Program, Phys. Rev. C, 96, 044904 (DOI: 10.1103/PhysRevC.96.044904) xxi, xxii, xxiii, 81, 82, 83, 84, 92, 93, 94, 96

[141] Ivanov Y. B. (2010), Baryon Stopping in Heavy-Ion Collisions at E_{lab} = 2-160 GeV/nucleon, Phys. Lett. B, 690, 358-362 (DOI: 10.1016/j.physletb.2010.05.051) 71, 83, 84, 86, 99

[142] Ivanov Y. B. (2013), Baryon Stopping as a Probe of Deconfinement Onset in Relativistic Heavy-Ion Collisions, Phys. Lett. B, 721, 123-130 (DOI: 10.1016/j.physletb.2013.02.038) 71, 83, 84, 86, 99

[143] Ivanov Y. B. (2013), Elliptic Flow of Protons and Antiprotons in Au+Au Collisions at $\sqrt{s_{NN}}$ = 7.7–62.4 GeV within Alternative Scenarios of Three-Fluid Dynamics, Phys. Lett. B, 723, 475-480 (DOI: 10.1016/j.physletb.2013.05.053) 71, 83, 84, 86, 99

[144] Ivanov Y. B., Blaschke D. (2015), Robustness of the Baryon-Stopping Signal for the Onset of Deconfinement in Relativistic Heavy-Ion Collisions, Phys. Rev. C, 92, 024916 (DOI: 10.1103/PhysRevC.92.024916) 71, 83, 84, 86, 99

[145] Ivanov Y. B., Blaschke D. (2016), Baryon stopping in heavy-ion collisions at E_{lab} = 2A-200A GeV, Eur. Phys. J. A, 52, 237 (DOI: 10.1140/epja/i2016-16237-4) 71, 83, 84, 86, 99

[146] Cooper F., Frye G. (1974), Comment on the Single Particle Distribution in the Hydrodynamic and Statistical Thermodynamic Models of Multiparticle Production, Phys. Rev. D, 10, 186 (DOI: 10.1103/PhysRevD.10.186) 87

[147] Stöcker H. (2007), Collapse of flow: Probing the order of the phase transition, PoS CPOD07, 025 (DOI: 10.22323/1.047.0025) 72

[148] Afanasiev S. V. *et al* (NA49 Collaboration) (2002), Energy dependence of pion and kaon production in central Pb + Pb collisions, Phys. Rev. C, 66, 054902 (DOI: 10.1103/PhysRevC.66.054902) xxi, xxiii, 82, 92, 96

[149] Steinheimer J., Bleicher M. (2011), Core-corona separation in the UrQMD hybrid model, Phys. Rev. C, 84, 024905 (DOI: 10.1103/PhysRevC.84.024905) 96

[150] Ahle L. *et al* [E866 and E917] (2000), An Excitation function of K- and K+ production in Au + Au reactions at the AGS, Phys. Lett. B, 490, 53-60 (DOI: 10.1016/S0370-2693(00)00916-3) xxi, xxiii, 83, 93

[151] Back B. B. *et al* [E917] (2001), Baryon rapidity loss in relativistic Au+Au collisions, Phys. Rev. Lett., 86, 1970-1973 (DOI: 10.1103/PhysRevLett.86.1970) xxii, xxiv, 84, 85, 86, 95, 98

[152] Anticic T. *et al* (NA49 Collaboration) (2011), Centrality dependence of proton and antiproton spectra in Pb+Pb collisions at 40A GeV and 158A GeV measured at the CERN SPS, Phys. Rev. C, 83, 014901 (DOI: 10.1103/PhysRevC.83.014901) xxii, xxiv, 84, 85, 86, 95, 98